

https://dspace.org/

The influence of shielded metal arc welding (SMAW) inter-pass temperature on the ferrite number of weld joints made on AISI 304H stainless steel

Ngonyoza, Ntsikelelo

2015-05-08
http://hdl.handle.net/10539/17702

Downloaded from a DSpace repository. https://dspace.org/



The Influence of Shielded Metal Arc Welding (SMAW) Inter-pass Temperature on the Ferrite Number of Weld Joints made on AISI 304H Stainless Steel

MSc(50/50) Research Project

Prepared by

Ntsikelelo Ngonyoza (552436)

Submitted to

School of Chemical and Metallurgical Engineering, Faculty of Engineering and the Built Environment, University of the Witwatersrand, Johannesburg, South Africa

Supervisor(s): Dr. Josias van der Merwe

October 2014

DEDICATION

I would like to thank my Lord and Saviour Jesus Christ for his guidance and providence. Thank you to my lovely wife, Maxine, for her support and love. To my mom for her sacrifices and nagging me about when I’m graduating, thank you.

ACKKOWLEDGEMENTS

The author would like to acknowledge:

- Ms Marion van den Hoogen, Materials and Corrosion Engineering Lead at SAPREF Refinery, for her patience.
- Dr. Josias van der Merwe, the author's supervisor, for his guidance and patience.
- Dr. Nicolas Dowling for his contribution towards my professional and career development.
- Mr Jay Padayachee and the SAPREF Refinery Inspection Department for financial support to conduct this investigation.
- Mr Mohamed Cader from Avenger-LTA for providing the welding resources needed to conduct the research.
- Ms Leanne Matyhyssen from MegChem (Pty) Ltd for chemical etching the specimens with Villela's reagent and Oxalic acid.

ABSTRACT

The research focused on the influence of welding inter-pass temperature in 304H type austenitic stainless steel weld joints in the as-welded condition. The shielded metal arc welding process was used to weld the joints. The following was evaluated: the theoretical and measured ferrite numbers, solidification mode and delta ferrite morphology, as well as the evolution and precipitation of secondary phases i.e. sigma phase in the weld, chromium carbides in the heat affected zone. After the evaluation, it was clear that the inter-pass temperature had an effect on solute distribution during cooling and subsequent calculated ferrite numbers of the welds. The calculated ferrite numbers, that were determined using the weld metal chemistry of each joint and the WRC-1992 constitution diagram, increased from FN of 1 to FN of 3 with the increase in welding inter-pass temperature from 105°C-100°C and to 195°C-200°C respectively. The measured ferrite number showed no correlation with the increases in interpass temperature. The highest measured ferrite number of 3.8 was obtained when welding at an inter-pass temperature of 135°C – 140°C which was closest to the FN of 5 required minimum, as specified by the SAPREF Refinery, to prevent solidification cracking. No solidification cracking was observed in any of the specimens evaluated in this study even though all the specimens had ferrite contents well below FN 5. This observation supports research that indicates that controlling of the primary solidification mode as delta ferrite is more important a factor in preventing solidification cracking than trying to control the actual ferrite content of the weld metal. The primary solidification mode of the weld was a combination of the austenite-ferrite (AF) to predominantly ferrite-austenite (FA) with the FA solidification mode dominating with the increase in inter-pass temperature. The nature of the carbides formed due to low temperature sensitization in the heat affected zone of the base metal changed with the increase in inter-pass temperature. The precipitated chromium carbides only formed discontinuous carbide networks at the interpass temperature of 195°C-200°C. The transformation of sigma from delta ferrite was not observed in the columnar dendritic and mushy zones of the weld metal. This research revealed the optimum welding inter-pass temperature for welding 304H austenitic stainless steel with 308H electrode to be 135-140°C.

TABLE OF CONTENTS

CONTENT	PAGE
I. CHAPTER ONE - INTRODUCTION	**17**
1.1 Background	**17**
1.2 Research objectives	**18**
II. CHAPTER TWO - LITERATURE REVIEW	**19**
2.1 Metallurgy of stainless steels	**19**
2.1.1 Solidification of stainless steel	21
2.2 Austenitic stainless steel microstructure	**24**
2.3 hot and cold working of austenitic stainless steels	**27**
2.3.1 Hot working of austenitic stainless steels	27
2.3.2 Cold working of austenitic stainless steels	29
2.4 Delta ferrite	**30**
2.4.1 Importance of delta ferrite in austenitic stainless steels	30
2.4.2 Influence of delta ferrite on performance of austenitic stainless steels in high temperature service	31
2.4.3 Effect of alloying elements on delta ferrite formation	34
2.5 Difference between 304, 304L and 304H austenitic stainless	**35**

2.5.1 Type 304, 304L and 304H chemical compositions and the significance of alloying elements 35

2.5.2 Differences in mechanical properties 38

2.6 Shielded metal arc welding (SMAW) process 41

2.7 Importance of inter-pass temperature 43

2.8 Post solidification phase transformation – The effect of solidification mode on the delta ferrite microstructure in austenitic stainless steel 43

2.9 Effect of constitutional supercooling on the weld metal austenitic matrix microstructure 47

2.10 Sigma phase transformations 51

2.10.1 Factors that influence the delta ferrite-sigma phase transformation in weld metals 51

2.10.1.1 Compositional conditions 52

2.10.1.2 Structural conditions 52

2.11 Methods and difficulties in the measurement of delta ferrite 53

2.11.1 Metallographic evaluation 54

2.11.2 X-ray diffraction 54

2.11.3 Magnetic permeability measurements 54

2.11.4 Magnetic determination 55

2.11.5 Calculation of ferrite from chemistry **60**

2.12 Control of ferrite content/ferrite number **60**

2.12.1 Heat input 60

2.12.2 Cooling rate 61

2.12.3 Welding process 62

2.12.4 Welding consumable considerations 63

2.13 Sensitization of austenitic stainless steels **63**

2.13.1 Sensitization theory 63

2.13.2 Low temperature HAZ sensitization (LTS) behavior 66

2.14 Etching of austenitic stainless steels **67**

2.14.1 Electrolytic etching 67

2.14.2 Chemical etching 70

III. CHAPTER THREE - EXPERIMENTAL PROCEDURE **72**

3.1 Materials used **72**

3.2 Equipment used **74**

3.3 Procedure **75**

3.3.1 Joint preparation and welding 75

3.3.2 Ferrite measurement 76

3.3.3 Specimen extraction and sectioning 78

3.3.4 Specimen mounting 79

3.3.5 Specimen grinding and polishing 79

3.3.6 Specimen etching 81

3.3.7 Microscopy 81

IV. CHAPTER FOUR - RESULTS 82

4.1 Ferrite numbers 82

4.2 Metallurgical feature evaluation 87

4.2.1 Solidification phases 87

4.2.2 Presence of carbides in the heat affected zone 89

4.2.3 Evaluation for sigma phase transformation in the weld metal 93

4.2.4 Evaluation for sigma phase transformation in the weld metal 95

V. CHAPTER FIVE - DISCUSSION 99

5.1 Ferrite numbers 99

5.2 Metallurgical feature evaluation 100

5.2.1 Solidification phases 100

5.2.2 Delta ferrite morphology 101

5.2.3 Sigma phase transformation in the weld metal 102

5.2.4 Low temperature sensitization of the heat affected zone (HAZ) 103

VI. CHAPTER SIX – CONLCUSION 104

VII. CHAPTER SEVEN – FUTURE WORK OPPORTUNITIES 105

VIII. REFERENCES **106**

LIST OF TABLES

Table	Page
Table 1: Chemical compositions in wt% of some typical austenitic stainless steels	23
Table 2: Crystal structures and compositions of phases that may occur in stainless steels	24
Table 3: Solubility of sulphur and phosphorus in ferrite and austenite in wt %	31
Table 4: Creep-Rupture Properties of CF8 Castings	32
Table 5: Chemistry of 304, 304L and 304H austenitic stainless steel	38
Table 6: Mechanical properties of types 304, 304L and 304H austenitic stainless steel at 20 or 21°C	39
Table 7: : Maximum allowable stress values for types 304, 304L and 304H austenitic stainless steel for temperature range 65-825°C	39
Table 8: Effect of interpass temperature on the mechanical properties	43
Table 9 Electrolytic etchants for etching sigma phase, carbides and delta ferrite	70
Table 10: Chemical etchants for etching sigma phase, carbides and delta ferrite	71

Table 11: Chemical composition of the 304H austenitic stainless steel samples 72

Table 12: Chemical composition of the 308H welding electrode 73

Table 13: Welding variables used for welding the pipe samples 76

Table 14: Specimen preparation grinding and polishing steps and times 80

Table 15: Ferritescope ferrite content measurement readings for sample A to D welded at various inter-pass temperatures 83

Table 16: Chemical compositions of the weld metals of specimens A to D 85

Table 17: The calculated chromium-nickel-equivalents and WRC-1992 ferrite numbers of the weld metals of specimens A to D 85

Table 18: Weight % of different elements for EDS spectrum 1. 91

Table 19: Weight % of different elements for EDS spectrum 1 on the matrix of specimen C 92

Table 20: Comparison between ferritescope measured and the WRC-1992 predicted ferrite numbers 99

LIST OF FIGURES

Figure	Page
Figure 1: The influence of chromium on the atmospheric corrosion of low-carbon steel	19
Figure 2: Fe-Cr binary phase diagram	20
Figure 3: A section of the -Fe-Cr-Ni ternary equilibrium diagram at 650°	20
Figure 4: Vertical section of Fe-Cr-Ni phase diagram showing the variation of solidification mode with composition for a constant Fe content of 70%	21
Figure 5: Compositional and property linkages in the stainless steel family of alloys	23
Figure 6: Main transformations that occur in austenitic stainless steel between room temperature and the liquid state	25
Figure 7: Type 304 base metal and heat affected zone taken at X250 Magnification	26
Figure 8: The heat affected zone, fusion line and 308 filler weld metal of the fabrication taken at X250 Magnification	26
Figure 9: Effect of alloying elements on hot ductility of AISI 304L austenitic stainless steel	28
Figure 10: Stress rupture curves for E308 weld metal and CF8 castings	

at 593° C with different ferrite levels 33
Figure 11: Influence of the chemical composition, especially the
Cr content, on the oxidation resistance of steels 36

Figure 12: Stress rupture curves for ASTM 312 Type 304 and 304H 40

Figure 13: Shielded Metal Arc Welding Process 42

Figure 14: Solidification and post solidification transformation in
Fe-Cr-Ni welds (a) interdendritic ferrite, (b) vermicular ferrite and
(c) lathy ferrite (d) a schematic vertical or isoplethal section of
the Fe-Cr-Ni ternary phase diagram at 70 wt% Fe and above 1200°C 44

Figure 15: Solidification and transformation modes and resultant
ferrite morphologies 47

Figure 16: The effect of constitutional super-cooling on solidification
mode on the (a) planar, (b) cellular, (c) columnar dendritic and
(d) equiaxed dendritic grains 0f the weld metal 48

Figure 17: The effect of constitutional supercooling on solidification
mode during welding resulting in (a) planar, (b) cellular, (c) columnar
dendriticand (d) equiaxed dendritic grains 50

Figure 18: Microstructures depicting the effect of constitutional supercooling
on solidification mode during welding planar resulting in (a) planar,
(b) cellular, (c) columnar dendritic and (d) equiaxed dendritic grains 50

Figure 19: The variations in solidification mode in a single weld across
the fusion zone 50

Figure 20: Microstructure showing the variations in solidification mode in a single weld across the fusion zone 50

Figure 21: Sigma phase precipitation in an austenitic stainless steel containing delta ferrite 53

Figure 22: Schaeffler constitution diagram for stainless steel weld metal 56

Figure 23: DeLong constitution diagram for stainless steel weld metal, the Schaeffler austenite-martensite boundary is included for reference 57

Figure 24: WRC-1992 constitution diagram 60

Figure 25: Grain boundary structure of sensitized steel 64

Figure 26: Time-temperature-precipitation (TTP) for 304 type stainless steel 65

Figure 27: Time-temperature-sensitization (TTS) carbide precipitation curves for type 304 stainless steel 65

Figure 28: Basic laboratory setup for electrolytic etching and polishing 68

Figure 29: Idealized current density versus applied voltage for many common electrolytes with regions for electrolytic etching and polishing as indicated 69

Figure 30: Carbon compositional limits of ASTM A240/240M Type 304, 304L and 304H austenitic stainless steel 73

Figure 31: Welded pipe samples after sections were cut out 76

Figure 32: Top view of the weld bead on the welded samples with the centre line of weld bead marked as location A 77

Figure 33: Welded pipe samples with sections that were cut out for mounting and sample preparation 78

Figure 34: Graphical representation of ferrite content measurement readings from table 10. 84

Figure 35: Graphical comparison of the average ferrite content measurement readings from table 14. 84

Figure 36: Graphical comparison of the Cr_{eq}/Ni_{eq} ratio from table 16 85

Figure 37: Graphical comparison of the WRC-1992 ferrite numbers (FN) from table 16 86

Figure 38: Ferrite numbers plotted on WRC-1992 calculated using the weld metal chemistry of specimens A, B, C and D 86

Figure 39: Weld metal microstructure of specimens A to D at X200 magnification after chemical etching with Villela's reagent 88

Figure 40: Schematic of weld joint showing (1) base metal, (2), heat affected zone-HAZ, (3) fusion line, (4) columnar dendritic zone and (5) mushy zone. 89

Figure 41: Microstructures of the (a) base metal, (b) heat affected zone and (c) fusion line for specimen A at X200 magnification after

etching with oxalic acid. 89

Figure 42: Microstructures of the heat affected zone for specimen C at X10000 magnification after etching with oxalic acid 90

Figure 43: Microstructures of the heat affected zone for specimen C at X10000 magnification after etching with oxalic acid 90

Figure 44: location of EDS analysis. 91

Figure 45: Graph of Spectrum 1 EDS analysis. 92

Figure 46: SEM image with location of EDS analysis (spectrum 2) on the matrix of specimen C. 92

Figure 47: Graph of Spectrum 2 EDS analysis of the matrix of specimen C. 93

Figure 48: Microstructures of the columnar dendritic zone for specimen A welded at 105-110°C inter-pass temperature at (a) X500 and (b) X1000 after etching with oxalic acid. 93

Figure 49: Microstructures of the columnar dendritic zone for specimen B welded at 135-140°C inter-pass temperature at (a) X500 and (b) X1000 after etching with oxalic acid. 94

Figure 50: Microstructures of the columnar dendritic zone for specimen C welded at 165-170°C inter-pass temperature at (a) X500 and (b) X1000 after etching with oxalic acid. 94

Figure 51: Microstructures of the columnar dendritic zone for specimen D welded at 195-200°C inter-pass temperature at (a) X500 and (b) X1000

after etching with oxalic acid. 95

Figure 52: Location of the mushy zone in the weld metal of specimen A to D 95

Figure 53: Micrographs of the microstructures of specimens A to D
at X1000 magnification after electrolytic etching with NaOH 96

Figure 54: Stereographs of the weld after Groesbeck etchant at X6.7
Magnification 97

Figure 55: HAZ microstructure of the 304H austenitic steel base
metal at X1000 magnification after chemical etching with Groesbeck 98

LIST OF EQUATIONS

Equation	Page
Equation 1: Chromium equivalent (Cr_{eq})	22
Equation 2: Nickel equivalent (Ni_{eq})	22
Equation 3: G/R ratio equation	49
Equation 4: Proportionality function	61

I. CHAPTER ONE - INTRODUCTION

1.1 Background

This study will investigate the effect of welding inter-pass temperature on the delta ferrite content in as-welded AISI 304H stainless steel pipe. AISI 304H austenitic stainless steel is used in high temperature service because it is a cost effective solution for a material with the necessary high temperature oxidation and corrosion resistance, strength and creep properties for high temperature service that AISI 304 and AISI 304L do not have. AISI 304H stainless steel has traditionally been used in Fluid Catalytic Cracker regenerator internals, the associated equipment and piping, at temperatures between 650-760°C at the Shell & BP SAPREF Refinery in Durban, South Africa . Work by Schaeffler (1949), DeLong (1956) and later the Welding Research Council (WRC) (1992) has given an understanding of how the chemical compositions of materials influence the amount of delta ferrite produced and furthermore they developed diagrams to estimate the amount of delta ferrite produced in welds from the chemical compositions of materials. The weld chemistry in conjunction with the Schaeffler, Delong and WRC constituent diagrams has been predominantly used as the method to predict ferrite content. Little attention has been given to how welding related factors, for example inter-pass temperature, can influence the amount of delta ferrite nucleated in the weldment after welding. SAPREF has recently struggled to produce welds with low ferrite content after predictive tools indicated that low ferrite contents should be obtained. Thus the attempt to understand whether the welding inter-pass temperature influences ferrite content makes this research project significant. The understanding of how inter-pass temperature influences ferrite content when welding 304H stainless steel, could add to the current body of knowledge concerning factors that can influence ferrite content in addition to the chemistry of the welding consumable.

Austenitic stainless steel that are exposed to service temperatures between 550°C - 900°C are prone to cracking due to high temperature embrittlement as a result of sigma

phase formation and sensitization(Castro & de Cadanet, 1975). They further explained that the brittle sigma phase is formed when delta ferrite in stainless steel welds transform to sigma phase when exposed to high temperature service. Due to the brittle nature of sigmatized welds, repairing of sigmatized welds can only be done by removing the entire weld and re-welding the complete joint. SAPREF has in the past attempted to repair these cracked welds without complete removal. This proved to be a challenge because these sigmatized welds were so brittle that the cracks in the weld bead propagated into the heat affected zone (HAZ) of the base metal. The weld thus has to be completely removed and re-welded. This research project attempts to investigate the role the welding inter-pass temperature could play in the amount of delta ferrite produced because this delta ferrite will eventually transform to the chi, laves and brittle sigma phases during exposure to high temperature service.

1.2 Research objectives

- To investigate the effect of inter-pass temperature on the delta ferrite content of AISI 304H stainless steel weldments when using the shielded metal arc welding process (SMAW)
- To determine the optimum inter-pass temperature and welding variables to be used during the repair welding of AISI 304H stainless steel joints at the SAPREF refinery to produce low ferrite number welds, between FN 5 and FN 8, in order to prevent solidification cracking during welding and consequently excessive sigmatization at service temperatures respectively.
- To evaluate the effect of inter-pass temperature on the solidification microstructures of the welded joints and secondary phases i.e. sigma phase and sensitization ($M_{23}C_6$ carbides), that may have formed during welding and subsequent cooling will be evaluated.

II. CHAPTER TWO - LITERATURE REVIEW

Stainless steels are iron alloys containing 11% chromium and this amount of chromium prevents the formation of rust in unpolluted atmospheres; it is from this characteristic that the term “stainless is derived”. Figure 1 shows corrosion rate to decrease as chromium content increases because a very thin protective and self-healing surface film known as a passive film forms (Sedriks 1996).

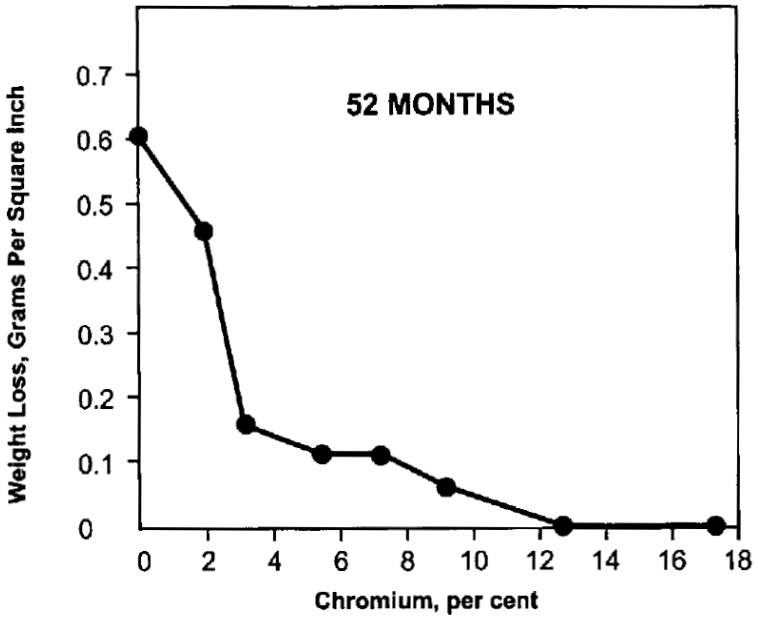

Figure 1: The influence of chromium on the atmospheric corrosion of low-carbon steel (Binder & Brown 1946)

2.1 Metallurgy of Stainless Steels

The base for the various stainless steels is the binary Fe-Cr system shown in Figure 2; the properties of the binary Fe-Cr system are modified by the addition of several major alloying elements such as Ni, Mo, Mn etc. as well as minor ones such as C and N (George & Shaik, 2002).

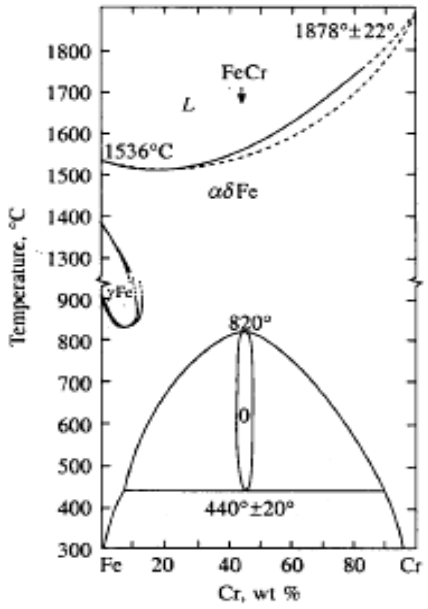

Figure 2: Fe-Cr binary phase diagram (Rivlin and Raynor, 1980)

The Fe-Cr-Ni alloys are the most predominantly used stainless steel. The Important phase relationships in Fe-Cr-Ni stainless steels can be considered to stem from the properties of the binary Fe-Cr and Fe-Ni phase diagrams. The phase relationships in the Fe-Cr-Ni system at 650° are shown in the ternary phase diagram in Figure 3.

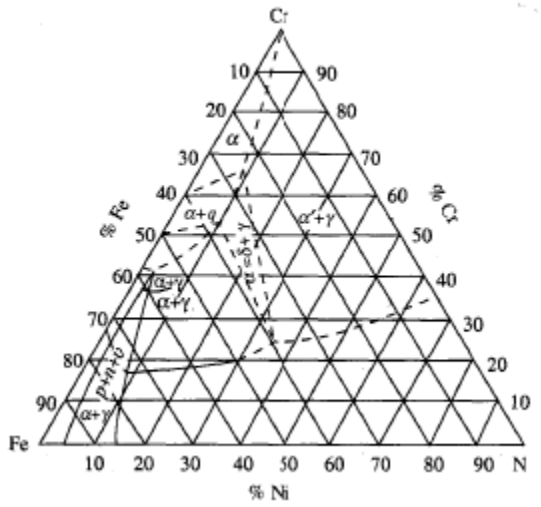

Figure 3: A section of the -Fe-Cr-Ni ternary equilibrium diagram at 650°C (Marshall 1984).

2.1.1 Solidification of stainless steels

A convenient way of understanding the phase relationship in the Fe-Cr-Ni ternary system is by the use of cross-sections through the ternary diagram, such that the proportion of one element is constant. A section of the Fe-Cr-Ni diagram at a constant Fe content of 70% from the work of Kujanpaa, Suutala, Takalo & Moisio, (1979) is shown in figure 4. According to Allan (1995) Figure 3 shows that stainless steels can solidify by the following mechanisms or modes:

- Ferritic or mode A ($L \rightarrow L + \delta \rightarrow \delta$)
- Ferritic-austenitic or mode B ($L \rightarrow L + \delta \rightarrow L + \delta + \gamma \rightarrow \gamma + \delta$)
- Austenitic-ferritic or mode C ($L \rightarrow L + \gamma \rightarrow L + \gamma + \delta \rightarrow \gamma + \delta$)
- Austenitic or mode D ($L \rightarrow L + \gamma \rightarrow \gamma$)

Where: L = Liquid, γ = Austenite and δ = Delta ferrite

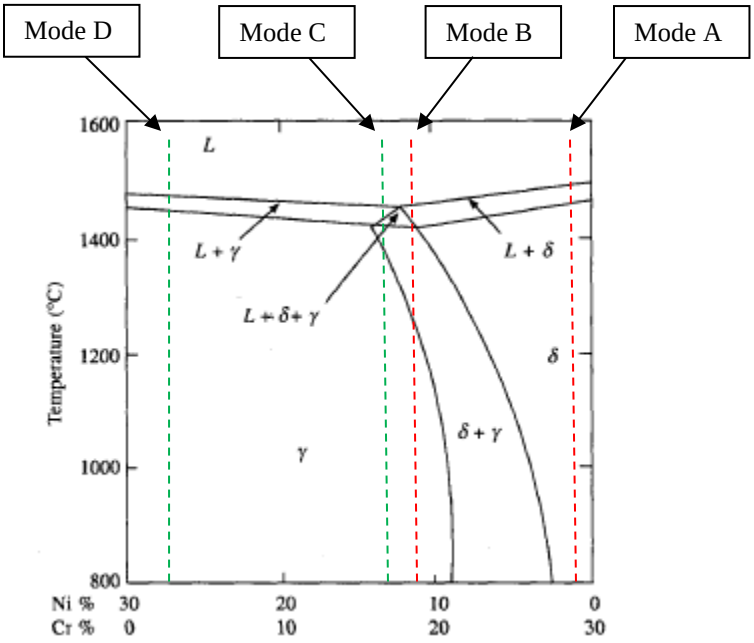

Figure 4: Vertical section of Fe-Cr-Ni phase diagram showing the variation of solidification mode with composition for a constant Fe content of 70% (Kujanpaa et al, 1979).

Allan (1995) and others, furthermore state that the solidification mode and sequence may also be successfully predicted using chromium and nickel equivalent ratios which are calculated using the ferrite and austenite forming elements respectively. Among several equations for chromium equivalent, Cr_{eq} and nickel equivalent, Ni_{eq} one can quote the following by Padilha and Guedes (1994) where all the elements are introduced into the formula in wt. (%).

Equation 1: Chromium equivalent, Cr_{eq}, equation (Padihla & Guedes, 2004)

$$Cr_{eq} = Cr + 1.37Mo + 1.5Si + 2Nb + 3Ti \quad (1)$$

Equation 2: Nickel equivalent, Ni_{eq}, equation (Padihla & Guedes, 2004)

$$Ni_{eq} = Ni + 0.3Mn + 22C + 14.2N + Cu \quad (2)$$

It also clear from Figure 3 that austenite is the stable phase in the Ni-rich side of the diagram while delta-ferrite is the equilibrium phase in the Cr rich side (George & Shaik 2002).

The properties of the Fe-Cr-Ni system can also be modified by the addition of several major and minor alloying elements such as Ni, Mo, Ti, Ni, Mn, C and Figure 5 shows a few compositional and property linkages in the family of stainless steels that can result from these various alloying elements being added to or reduced from Type 304 austenitic stainless steel. Chemical compositons of the various 200 and 300 series austenitic stainless steels is shown in table 1.

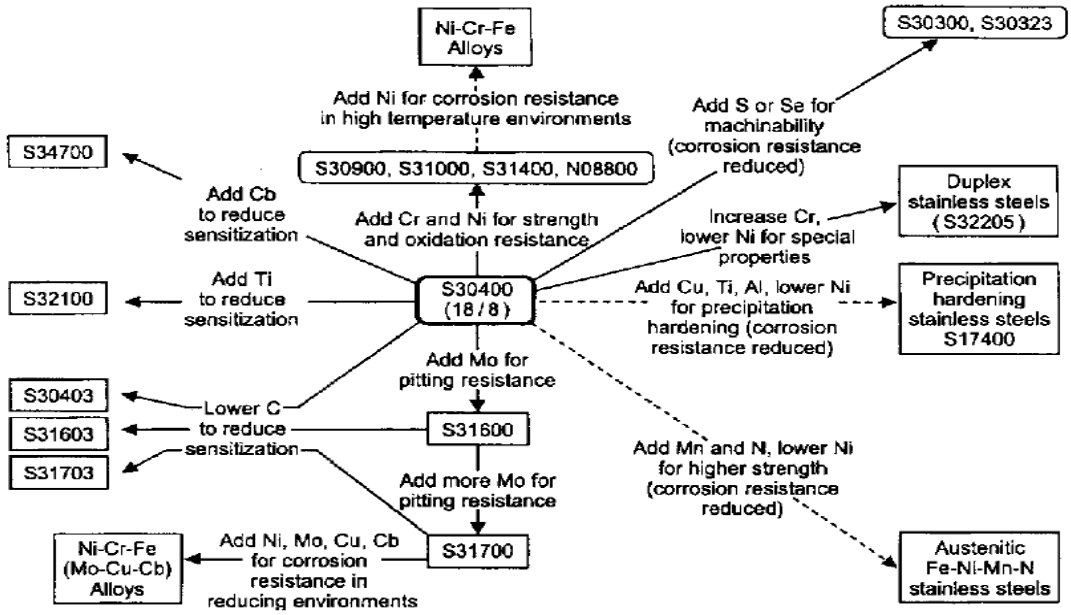

Figure 5: Compositional and property linkages in the stainless steel family of alloys (Sedriks 1996)

Table 1: Chemical compositions in wt% of some typical austenitic stainless steels (Padihla, Plaut & Rios 2007)

Type	UNS designation	C	Mn	Si	Cr	Ni	Mo	N	Others
AISI 201	S20100	≤0.15	5.50-7.50	≤1.00	16.00-18.00	3.50-5.50	-	0.25	-
AISI 202	S20200	≤0.15	7.50-10.0	≤1.00	17.00-19.00	4.0-6.0	-	0.25	-
AISI 205	S20500	0.12-0.25	14.0-15.5	≤1.00	16.50-18.00	1.0-1.75	-	0.32-0.40	-
AISI 301	S30100	≤0.15	≤2.00	≤1.00	16.00-18.00	6.0-8.0	-	-	-
AISI 302	S30200	≤0.15	≤2.00	≤1.00	17.00-19.00	8.0-10.0	-	-	-
AISI 303	S30300	≤0.15	≤2.00	≤1.00	17.00-19.00	8.0-10.0	0.6	-	-
AISI 304	S30400	≤0.08	≤2.00	≤1.00	18.00-20.00	8.0-10.5	-	-	-
AISI 304H	S30409	0.04-0.10	≤2.00	≤1.00	18.00-20.00	8.0-10.5	-	-	-
AISI 304L	S30403	≤0.03	≤2.00	≤1.00	18.00-20.00	8.0-12.0	-	-	-
AISI 304N	S30400	≤0.08	≤2.00	≤1.00	18.00-20.00	8.0-10.5	-	0.10-0.16	-
AISI 304LN	S30451	≤0.03	≤2.00	≤1.00	18.00-20.00	8.0-12.0	-	0.10-0.16	-
AISI 308	S30800	≤0.08	≤2.00	≤1.00	19.00-21.00	10.0-12.0	-	-	-
AISI 309	S30900	≤0.20	≤2.00	≤1.00	22.00-24.00	12.0-15.0	-	-	-
AISI 310	S31000	≤0.25	≤2.00	≤1.00	24.00-26.00	19.0-22.0	-	-	-
AISI 316	S31600	≤0.08	≤2.00	≤1.00	16.00-18.00	10.0-14.0	2.0-3.0	-	-
AISI 316H	S31609	≤0.08	≤2.00	≤1.00	16.00-18.00	10.0-14.0	2.0-3.0	-	-
AISI 316L	S31603	≤0.03	≤2.00	≤1.00	16.00-18.00	10.0-14.0	2.0-3.0	-	-
AISI 316LN	S31653	≤0.03	≤2.00	≤1.00	16.00-18.00	10.0-14.0	2.0-3.0	0.10-0.16	-
AISI 316N	S31651	≤0.08	≤2.00	≤1.00	16.00-18.00	10.0-14.0	2.0-3.0	0.10-0.16	-
AISI 317	S31700	≤0.08	≤2.00	≤1.00	18.00-20.00	11.0-15.0	3.0-4.0	-	-
AISI 317L	S31703	≤0.03	≤2.00	≤1.00	18.00-20.00	11.0-15.0	3.0-4.0	-	-
AISI 321	S32100	≤0.08	≤2.00	≤1.00	17.00-19.00	9.0-12.0	-	-	Ti≥5 x %C
AISI 321H	S32109	0.04-0.10	≤2.00	≤1.00	17.00-19.00	9.0-12.0	-	-	Ti≥5 x %C
AISI 347	S34700	≤0.08	≤2.00	≤1.00	17.00-19.00	9.0-13.0	-	-	Nb≥10 x %C
AISI 347H	S34709	0.04-0.10	≤2.00	≤1.00	17.00-19.00	9.0-13.0	-	-	1.0≥Nb≥10 x %C
654 SMO®	S32654	≤0.02	2.00-4.00	≤0.50	24.0-25.0	21.0-23.0	7.0-8.0	0.45-0.55	Cu = 0.30-0.60

(AISI = american iron and steel institute; UNS = unified numbering system).

2.2 Austenitic stainless steel microstructure

The austenitic stainless steel matrix microstructure is a solid solution, with very low stacking fault energy and a high work hardening capability (Schramm & Reed, 1975). The austenitic stainless steel microstructure has various carbides and intermetallic phases. Table 2 shows the metallic and intermetallic phases, carbides, nitrides, borides and sulphides in decreasing prominence. As seen in Table 2, the carbides that are most prominent are the $M_{23}C_6$ and MC type. The MC type are present in the niobium, titanium, vanadium stabilized steels. The most common intermetallic phases in these steels are the sigma (σ), Laves and chi (χ) phases.

Table 2: Crystal structures and compositions of phases that may occur in stainless steels (Plaut, Herrera.Escriba, Rios & Padilha (2007)

Phase	Unit cell	Atoms per cell	Space group	Lattice parameters(nm)	Composition
			metallic phases		
Sigma (σ)	bct	30	$P4_2/mnm$	a=0.87-0.92 c=0.4554-0.48	$(Fe,Ni)_x(Cr,Mo)_y$
Chi (χ)	bcc	58	I43m	a=0.881-0.895	$Fe_{36}Cr_{12}Mo_{10}$; $(Fe,Ni)_{36}Cr_{18}Mo_4$
Laves (η)	hex.	12	$P6_3/mmc$	a=0.473-0.483 c=0.772-0.786	Fe_2Mo; Fe_2Nb; Fe_2Ta; Fe_2Ti; Fe_2W
G	fcc	116	Fd3m	a=1.115-1.120	$Ni_{16}Nb_6Si_7$; $Ni_{16}Ti_6Si_7$; $(Ni,Fe,Cr)_{16}(Nb,Ti)_6Si_7$
R	hex.	53 (159)	R3	a=1.090; c=1.934	$Fe_{22}Mo_{18}Cr_{13}$; $(Fe,Ni)_{10}Cr_5Mo_3Si_2$
Mu (μ)	rhombohedral	13	R3m	a=0.4762; c=2.5015	$(Fe,Co)_7(Mo,W)_6$; $(Cr,Fe)_7(Mo)_2(Cr,Fe,Mo)_4$
γ'	fcc	4	Pm3m	a=0.3565-0.3601	$(Ni,Co,Fe,Cr)_3(Al,Ti)$
γ''	bct	8	$P4_2/mnm$ I4/mmm	a=0.3624; c=0.7406	Ni_3Nb
η	hex.	8	$P6_3/mmc$	a=0.5109; c=0.8299	Ni_3Ti
δ	orthorombic	8	Pmmn	a=0.5116 b=0.4259 c=0.4565	Ni_3Nb
β	ord bcc	2	Pm3m	a=0.2865-0.2887	NiAl
			Carbides		
$M_{23}C_6$	fcc	116	Fm3m	a=1.057-1.068	$(Cr, Fe, Mo)_{23}C_6$; $(Cr_{16}Fe_5Mo_2)C_6$
MC	ord fcc	8	Fm3m	a=0.4131-0.4698	(Ti,Nb,V)C
M_6C	fcc	112	Fd3m	a=1.085-1.128	$(Fe, Mo, Nb,Cr,Si)_6C$
M_7C_3	pseudo hex.	40	Pnma	a=1.398 c=0.4523	$(Cr,Fe)_7C_3$

The schematic in Figure 6 shows a time-temperature-transformations (TTT) diagram with all the phases and their transformations, which can occur in the austenitic stainless steels when cooled from the liquid state down to room temperature.

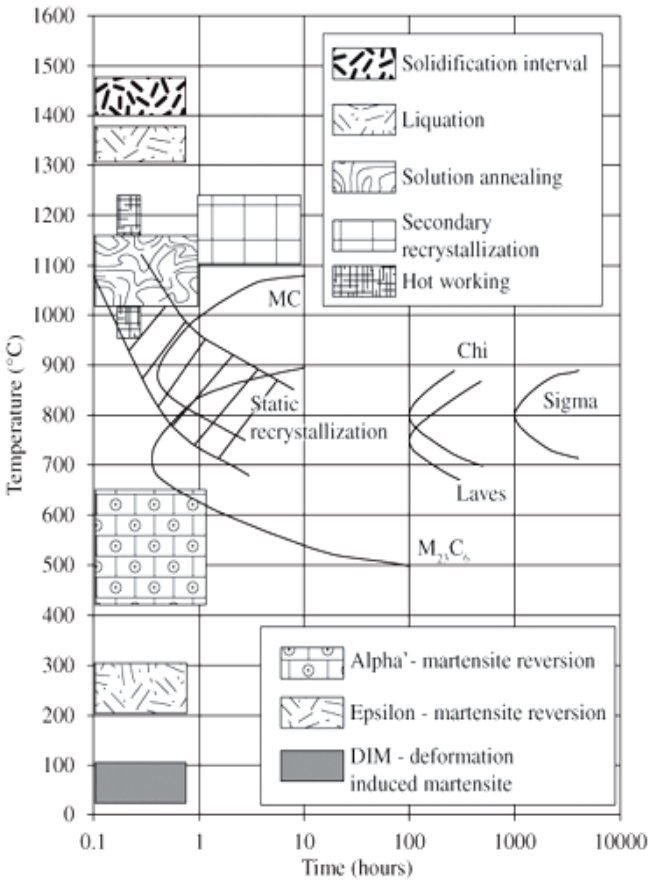

Figure 6: Main transformations that occur in austenitic stainless steel between the liquid state and room temperature (Padilha, Plaut & Rios, 2003)

Figures 7a-c and 8a-c show micrographs taken from different locations in a part fabricated from annealed type 304 stainless steel strip by roll forming, and by gas metal arc welding using type 308 filler metal. The fabrication specimens were etched by swabbing with fresh Acetic Glyceregia which was made by mixing 10ml nitric acid, 10 ml acetic acid, 15 ml hydrochloric acid and 5ml glycerol. Figure 7a shows a location unaffected by fabrication showing the original structure of annealed strip, equiaxed austenite grains and annealing twins. Figure 7b shows a location that was roll formed, showing slip bands resulting from cold working of the annealed strip. Figure 7c shows a location in the heat affected zone where the formed strip was exposed to temperature in

the sensitizing range of 427-816°C during welding, showing precipitation of carbide particles at grain boundaries with some remnants of slip bands resulting from cold working are also apparent.

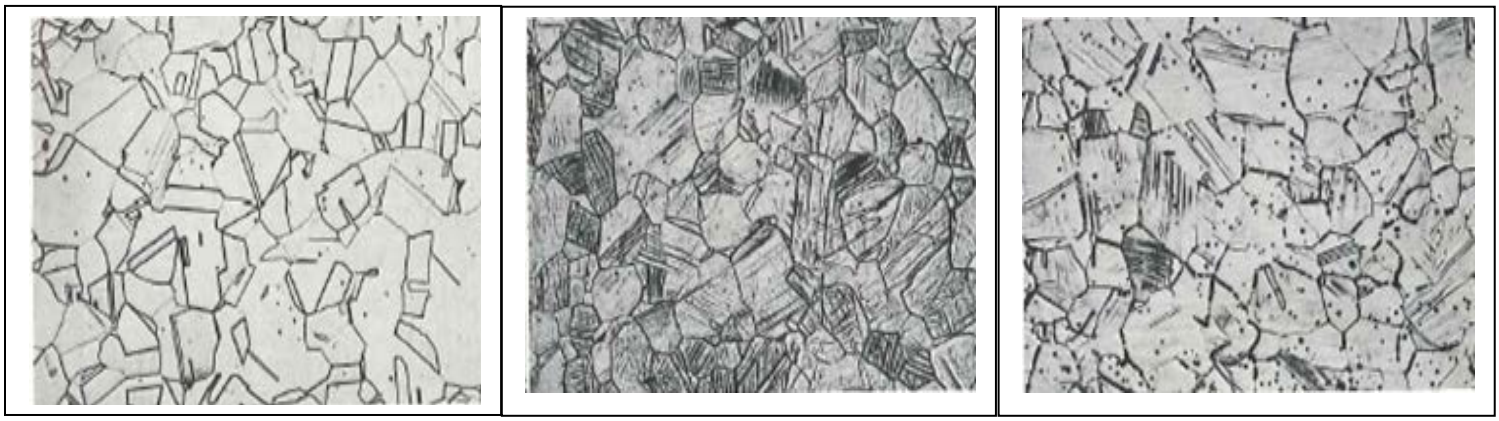

Figure 7: Type 304 base metal and heat affected zone taken at X250 Magnification (Mehl 1972)

Figure 8a shows a location in the heat affected zone where the welding temperature was above 816°C, showing partial recrystallization of the cold worked structure. Figure 8b shows a location at the interface of the base metal (left) and weld metal (right); the heat affected zone is fully recrystallized because of being heated above 1093°C during welding, and is free of carbide precipitation because the strip was cooled rapidly through the sensitization range. Figure 8c shows a specimen of the weld metal, showing a dendritically cored structure containing some delta ferrite (islands at top) and precipitated carbides (small black particles) in an austenitic matrix. Dendritic coring is characteristic of rapidly frozen austenitic weld metal.

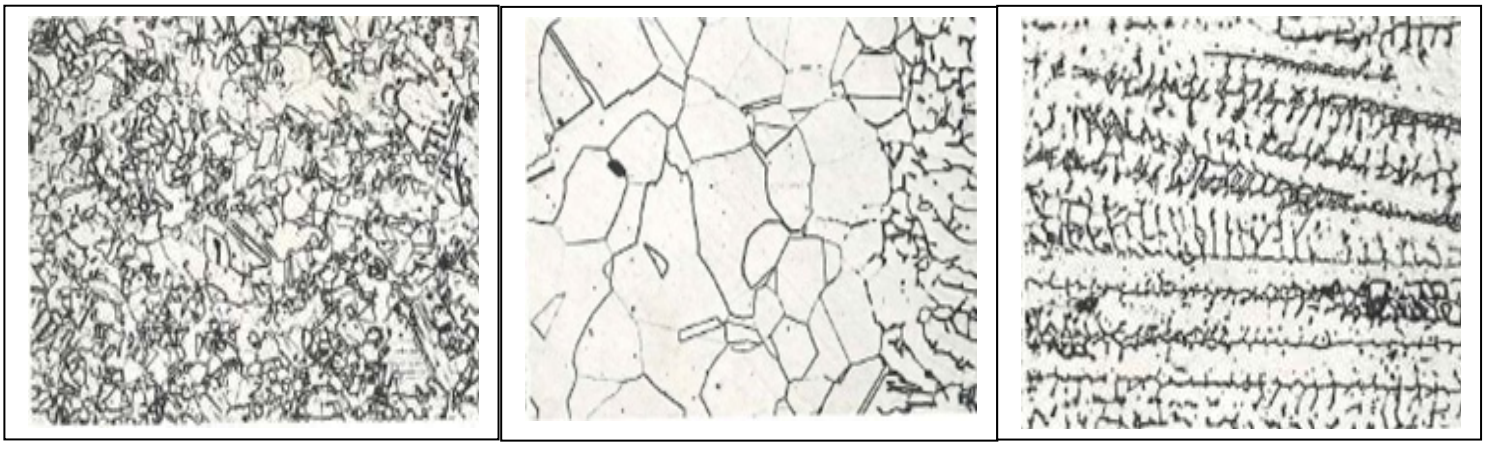

Figure 8: The heat affected zone, fusion line and 308 filler weld metal of the fabrication taken at X250 Magnification (Mehl 1972)

2.3 Hot and cold working of austenitic stainless steel

It is generally well known that austenitic stainless steels cannot be hardened by heat treatments but that cold or warm working (drawing, rolling, forging, etc.) can make such stainless steels harden (Milad, Zreiba, Elhalouan &Baradai, 2007). For austenitic stainless steels, the greater the amount of plastic strain induced, the higher is the stress required to deform the material further. This phenomenon is known as strain (or work) hardening, and is attributed to the increasing difficulty of dislocations movement as their density increases with deformation (Milad et al, 2007).

2.3.1 Hot working of austenitic stainless steels

After solidification, via conventional or continuous casting, wrought austenitic stainless steels are, in general, hot worked. According to Ahlblom and Sandström (1982) and Keown (1980) several factors influence hot ductility of the austenitic stainless steels: temperature, strain, strain rate, chemical composition, grain size and orientation, non-metallic inclusions and prior mechanical or thermal heat treatments. The analysis of the effects of the alloying elements on the hot ductility of the austenitic stainless steels presents increased difficulties due to the fact that practically all alloying elements and impurities influence the amount of delta ferrite that is formed (Plaut, Herrera, Escriba, Rios & Padilha 2007). Figure 9 shows the hot ductility variations, evaluated by hot tensile testing at a constant strain rate of 6 per second (S^{-1}), for several additions to the base-composition of the AISI 304L steel. The curves in Figure 9 show a similar shape and the work of Keown (1980) further divides the curves into the following three stages:

Stage 1 - In the 900 to 1000 °C, temperature range, ductility is low,

Stage 2 - In the 1100 to 1200 ºC range, ductility significantly increases due to dynamic recrystallization.

Stage 3 – In the temperature range 1250-1350 °C, ductility loss is related to the lack of grain boundary cohesion and eventually with the occurrence of some liquation.

From Figure 9 It may also be observed that small Ti additions enhance hot ductility of the 304L steel while all the other element additions (N, Cr, Ni, Mo, S, C and Mn + Si) have a negative effect of the hot ductility. In the case of the AISI 316 steel, 40-90 ppm additions of boron improve the hot ductility (Keown 1980).

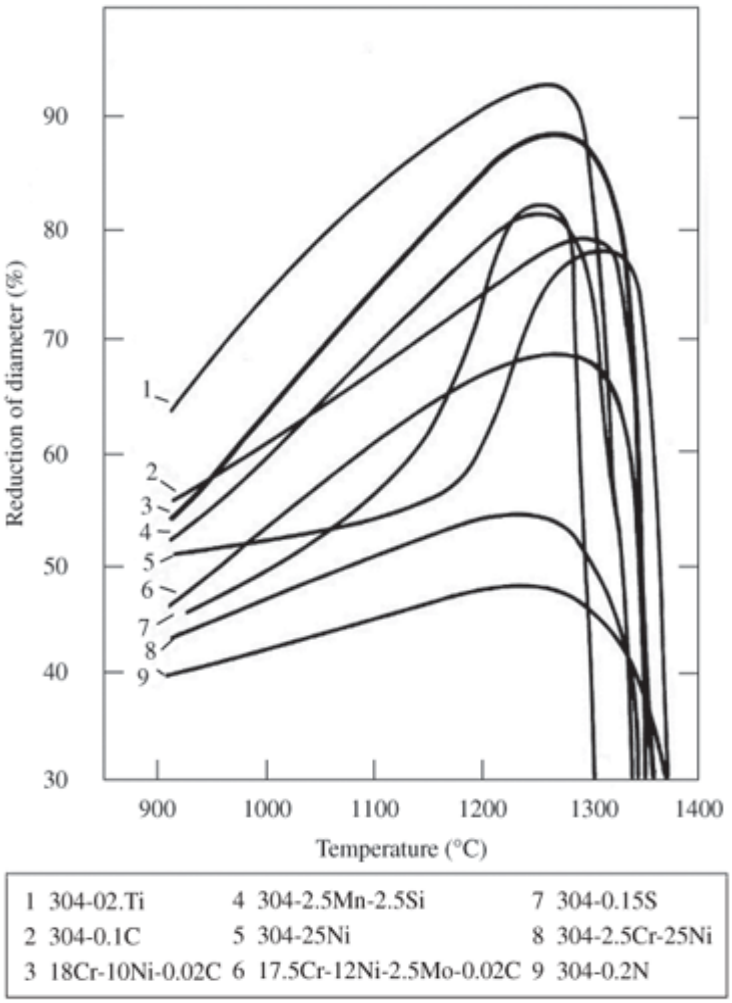

Figure 9: Effect of alloying elements on hot ductility of AISI 304L austenitic stainless steel (Keown 1982)

2.3.2 Cold working of austenitic stainless steels

When Austenite is unstable, it transforms at least partially to martensite and this greatly increases its mechanical strength. In comparison, a highly stable austenite will limit the strain hardening of the alloy (Lacombe Baroux & Beranger, 1993). Reed (1962) further explained that two types of martensites can form spontaneously in austenitic stainless steels. These two types of martensites have a body centered cubic (BCC) and the hexagonal close packed (HCP) metallurgical structure. The martensite with the HCP metallurgical structure is ε-martensite and is formed by mechanical strain induced by cold work. The martensite with the BCC metallurgical structure is ά-martensite, and it is formed thermally on cooling (M´Esz´Arosa & Proh´Aszkab 2005). According to Reed (1962) deformation induced or strain induced martensite (ε-martensite) is a unique feature of austenitic stainless steels. During plastic deformation, dislocation density (or crystalline defects) and in consequence the stacking fault density, within the host material, increases with the degree of deformation. The dislocations and twins are considered to be the major sources for martensitic phase transformation (Mumtaz, *et al.,* 2004). Schramm and Reed (1975) believe stacking faults are in hexagonal symmetry arrangement in FCC lattices, like ε-martensite, n stacking faults can form a hexagonal ε-martensite crystal. As aforementioned, ά-martensite is formed on cooling of the austenitic stainless steel. When enough driving force i.e. decrease in Gibbs free energy exists, the ά-martensite nucleus will rapidly grow as plates and the growth of ά-martensite occurs by the repeated nucleation of new embryos and coalescence (Hedström, Lienert, Almer, Odén, 2008). The fact that magnetization of a material is closely related to the microstructure of the materials makes magnetic measurements a technique for non-destructive testing (Murr, Staudhammer & Hecker, 1982). At room temperature, all austenitic stainless steels are paramagnetic in the fully annealed condition (M´Esz´Arosa & Proh´Aszkab 2005). The hcp ε-martensite is paramagnetic in contrast to the bcc ά-martensite which is strongly ferromagnetic and the only magnetic phase in the low carbon austenitic stainless steels (Reed 1962). The strain induced martensite may revert back into austenite during subsequent annealing, even for temperatures that are lower than the temperature for static recrystallization (Padilha,

Plaut & Rios, 2003). The austenitic stainless steels are generally supplied in the solution annealed condition, performed in the temperature range of 1000 to 1120 °C. It is important to note that even though these stainless steels are supplied in the solution annealed condition they invariably contain some residual delta ferrite in their microstructure (Padilha, Plaut & Rios 2007).

2.4 Delta Ferrite

2.4.1 Importance of delta ferrite in austenitic stainless steels

During the welding process the solidification strength of austenitic stainless steels can be seriously impaired by the presence of relatively small amounts of low melting point impurities such as sulphur and phosphorus. During solidification these low-melting point impurities are forced out to the grain boundaries as they are last to solidify because their melting point is lower than that of the stainless steel. The grain structure is therefore weakened at the locations on the grain boundary where these impurities accumulate. The presence of these impurities, when coupled with the high coefficient of expansion of austenitic stainless steels when compared to that of martensitic and ferritic stainless steels, can cause serious solidification cracking problems called ‘micro-fissures’ (Singh 2011).One method of reducing the effect of micro-fissuring is to disperse these low-melting point impurities among disconnected grain boundaries that surround the islands or colonies of a second phase that has the capacity to absorb the impurities. This can be accomplished by modifying the chemical composition of the steel in such a way to allow the creation of islands or colonies of ferrite in the welds which is dispersed throughout the microstructure (Singh 2011). Due to the high solubility delta ferrite has for sulphur and phosphorus impurities; some delta ferrite is intentionally allowed to be retained as a second phase in weld metal and in castings because it acts as a sink for sulphur and phosphorus; its presence therefore reduces solidification cracking (Sedriks 1996). Table 3 quantifies the solubility of sulphur and phosphorus in delta ferrite and austenite in weight % (wt %).

Table 3: Solubility of sulphur and phosphorus in ferrite and austenite in wt % (Borland and Younger, 1960)

	In δ-Ferrite	In Austenite
Sulphur	0.18	0.05
Phosphorus	2.8	0.25

The type 304H austenitic stainless steel is designed to follow the Ferritic-austenitic solidification sequence or mode B ($L \rightarrow L + \delta \rightarrow L + \delta + \gamma \rightarrow \gamma + \delta$), as shown in figure 3. As seen in the solidification sequence, Type 304H stainless steel will solidify initially as delta ferrite during welding, which has a high solubility for the sulphur and phosphorus impurities at high temperature. Most of the delta ferrite then transforms to austenite upon further cooling and results in an austenitic matrix containing tiny patches of residual delta ferrite. The presence of delta ferrite has the potential to reduce the corrosion resistance of the steel very slightly but its ability to prevent micro-fissuring which can lead to catastrophic failure makes it desirable in small quantities as low as 4 wt% (Singh 2011). Work by Konteki and Armao (2011) revealed that a ferrite content of 4 wt%, FN4, was required to avoid solidification cracking and was best determined by measurement with a magnetic instrument calibrated to AWS A4.2 or ISO 8249.

2.4.2 Influence of delta ferrite on performance of austenitic stainless steels in high temperature service

Control of the structure of stainless steel weld deposits and castings is important because the microstructure of the steel influences many of its properties. As aforementioned, the presence of delta ferrite reduces hot cracking in deposited weld metal, and reduces hot tearing in castings. The adverse effects of delta ferrite for some applications might include the higher magnetic permeability of alloys containing ferrite, or the decrease of impact strength during long-time high-temperature service through an increase in the rate of sigma phase formation (Hull 1973). In the work of Hauser and Vanecho (1982), where the effects of delta ferrite level on tensile and creep-rupture behavior of E308-16 shielded metal-arc stainless steel weld metal with FN 2, 6, 10 and

16 were determined. This study showed that the creep strength decreased as ferrite content increased. The weld metal with the lowest ferrite number of 2 FN had the highest creep strength at all three test temperatures of 537°C, 593°C and 648°C (1000, 1100, and 1200°F). At 648°C and at low creep rates at 593°C, the weld metal with the highest ferrite number of 16 FN had the lowest creep strength (Hauser & Vanecho 1982). The findings in the study conducted by Hasuer and Venecho agreed with earlier work done by Voorhees (1979), which compared the creep rupture times of CF8 castings with 3% ferrite and 16% ferrite and the work of smith (1969), which evaluated the yield, tensile, creep and rupture strengths of Types 304 and 304H wrought stainless steels . The results of this study done by Hauser and Vanecho (1982) are reported Table 4.

Table 4: Creep-Rupture Properties of CF8 Castings Voorhees 1979)

				Secondary creep period							
				Start		Rate	End		Rupture	Elong.,	R.A.,
Spec. no.	Temp., °F	Stress, ksi	Total strain on loading, %	Creep, %	Time, h	%/h	Creep, %	Time, h	life, h	%/4D	E. %
CF8, Lot D-4. Ingersoll-Rand Co., Ht. No. 6876. (2050° F, 3½ h, W.Q.)									*3% calculated ferrite.*		
D4-47	1100	25	16.1	3.2	63	0.012	4.2	146	172.9	24.5	34.4
D4-49	1100	22.5	10.45	1.8	160	0.00265	2.7	500	763.0	16	18.8
D4-62	1100	20	7.25	2.3	1080	0.00083	3.2	2160	4794.1	21	36.0
CF8, Lot D-10. Esco Corp., Ht. No. 40S-25976.									*16% calculated ferrite.*		
D10-28	1100	25	6.2	4.0	4.8	(0.40)	–		15.8	21.5	35.6
D10-65	1100	20	3.0	4.9	50	0.037	7.3	115	182.1	19	23.0
D10-23	1100	16		2.2	78	0.0059	6.0	720	1108.4	17.5	22.5
D10-53	1100	12.5	0.13	1.1	1070	0.00055	1.8	2320	(2.66% creep/3360 h)		
D10-63	1100	10	0.27	[0.00017 to 0.91%/3168 h]							

Figure 10 shows plots of stress rupture curves from the following four different studies:

- The adjusted average creep-rupture values for Types 304 and 304H wrought stainless steels reported by Smith (1969),
- The creep rupture times of CF8 castings with 3% ferrite and 16% ferrite by Voorhees,
- The E308 weld metal with ultra low ferrite FN of 2, Low ferrite of FN 6, Medium Ferrite of FN 10 and high ferrite of FN16.
- The expected minimum creep rupture values for Type 304 stainless steel published in the 1977 ASME Code Case N-47-12 (1592).

The plots in Figure 10 show a general trend of a decrease in creep rupture strength as ferrite content increases. According to Hauser and Vanecho (1982) when compared to the austenitic weld metals, the austenitic castings have the following creep-rupture properties:

• Lower strength.

• Lower secondary creep rate.

• Higher elongation and reduction of area at fracture, especially at the longer rupture times.

The CF8 having a calculated ferrite level of 3% in Figure 10 was significantly stronger than CF8 having a calculated ferrite level of 16%.

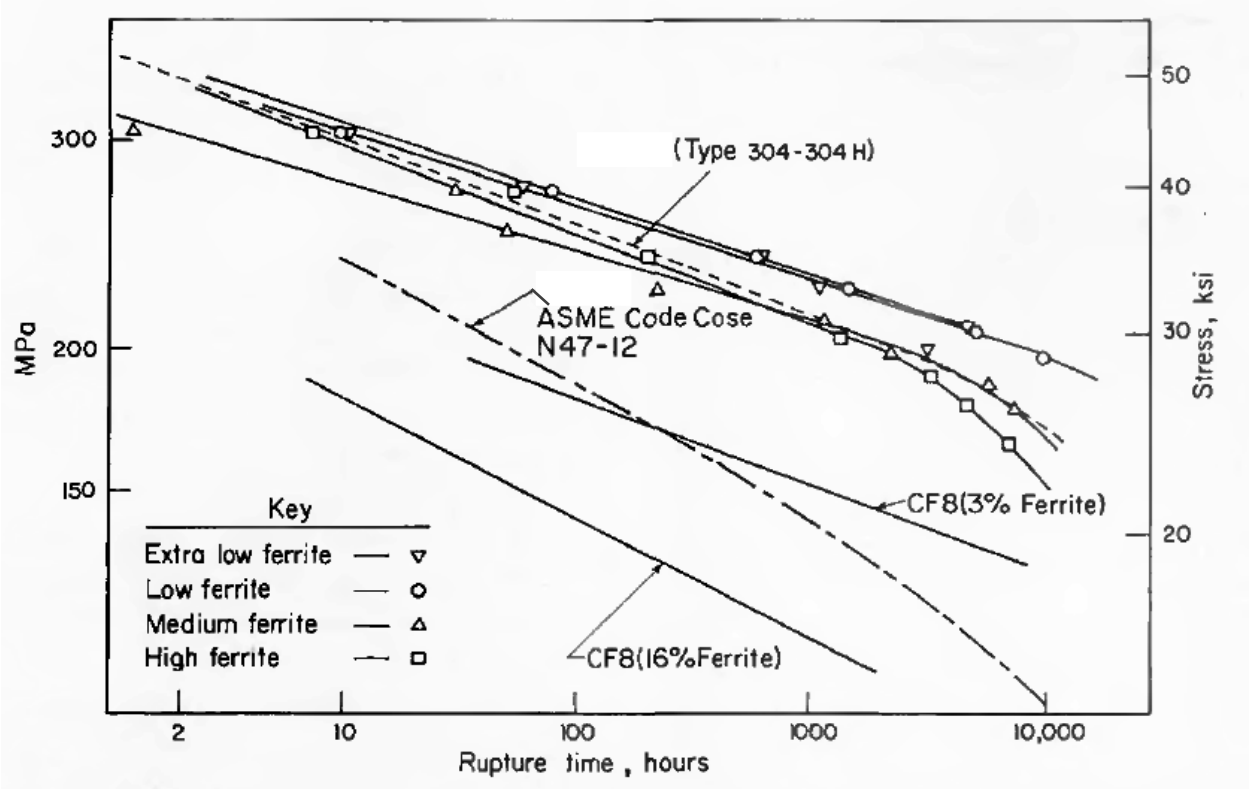

Figure 10: Stress rupture curves for E308 weld metal and CF8 castings at 593° C with different ferrite levels (Hauser and Vanecho 1982)

2.4.3 Effect of alloying elements on delta ferrite formation

According to Castro & de Cadanet (1975) an increase in chromium, niobium, molybdenum and silicon increases the temperature range in which delta ferrite can exist, and can be described as ferrite forming elements.

An increase in the proportion of ferrite formers therefore tends to increase the quantity of ferrite and sigma phase likely to be formed, and to accelerate the formation. High silicon and molybdenum contents have the effect of increasing ferrite stability to higher temperatures and the temperature range over which sigma phase exists increases as well. As an example a steel containing 20 wt% chromium, 10 wt% nickel and 3 wt% molybdenum still forms sigma phase at 1000°C, whereas in molybdenum-free compositions this phase ceases to exist above about 900°C. Work by Ogawa and Tsunetomi (1982) on the hot cracking susceptibility of austenitic stainless steels showed that silicon, when present in appreciable amounts in welded joints decreases the hot cracking resistance. All ferrite formers are present in high amounts in sigma type intermetallic compounds, so the diffusion rates of individual elements play an important role in sigma formation.

Austenite forming elements such as nickel, carbon, nitrogen and copper extend the temperature range where austenite can exist (Castro and de Cadanet, 1975). Therefore higher levels of austenite promoters diminish the tendency for standard stainless steels to form ferrite. Carbon acts mainly by forming complex carbides of chromium; molybdenum and tungsten, which renders these elements unavailable to form other phases. An increase in nickel and nitrogen content has the effect of retarding the diffusion of ferrite formers in the austenite, and consequently slows down the rate of precipitation of ferrite and subsequent transformation to sigma phase. Delta ferrite is therefore controlled and affected by content of chromium, molybdenum, niobium, nickel, carbon, nitrogen, manganese and copper (Priceputu & Moisa, 2011).

2.5 Difference between 304, 304L and 304H type austenitic stainless steels

Type 304 austenitic stainless steel is available in low or high controlled carbon contents, known as L and H grades (Albright & Hansen, 2009). This constitutes three separate grades. The H grade austenitic stainless steel, such as type 304H, has a carbon content greater than 0.04 wt% and is used in the solution annealed condition with grain size requirements of No. 7 or coarser. These compositional and heat treatment restrictions ensure high and reproducible creep rupture strengths at elevated temperatures (Sedriks1996). Types 304 and 304L stainless steels have no requirement for minimum carbon, control of grain size or annealing temperature (Kutz 2002). Type 304, 304L and 304H constitutes three separate grades and it is therefore more economical for mills to melt steel to only two different levels of carbon, and dual certify them as types 304/304L and types 304/304H (Kutz 2002). All austenitic stainless steels are susceptible to sensitization when sufficiently exposed the temperature range of 450-850°C. The low-carbon grades are preferred if sensitization is a problem. (Albright 2009). The high-carbon grades should be used with caution if service-induced carburization may be a problem.

2.5.1 Type 304, 304L and 304H chemical compositions and the significance of alloying elements

The introduction of the argon-oxygen decarburization (AOD) process for refining stainless steel has made profound changes in how existing grades were produced, as well as permitting totally new grades to be developed because, the AOD permits refining carbon to very low levels without removing chromium (Kutz 2002).

The minimum and maximum chemical composition limits for 304, 304L and 304H type stainless steel are almost identical with slight differences in the carbon, nickel and nitrogen contents as seen in Table 5 taken from ASTM A240/A240M.

2.5.1.1 Chromium

Chromium as an alloying element in stainless steel is a strong ferrite former that has outstanding corrosion resistance to oxidizing acids but offers little resistance to reducing acids or halogen acids (Kutz 2002). As aforementioned, the addition of chromium as alloying element forms a protective, self-healing passive film that protects the steel from corrosion making it stainless (Sedriks 1996). Oxidation is the most important high-temperature corrosion reaction and the protective film also enhances the high temperature oxidation resistance of ferrous metals (Davis 1994). The basic mechanism involves the formation of a Cr2O3 and/or a FeCr2O4 spinel protective film (Dillon 1995). Figure 11 shows the temperature range for which different ferrous materials present a satisfactory oxidation resistance. As expected, the maximum operating temperature increases with an increase in the chromium content. Table 5 also shows Type 304 and 304L to have the same minimum and maximum compositional limits for chromium of 17.5 and 19.5 wt% respectively. Type 304H has a higher chromium content range between 18-20 wt% because Type 304H is used at elevated temperatures.

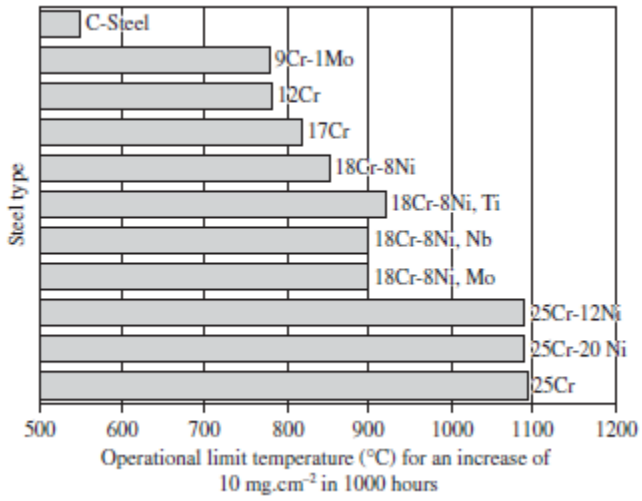

Figure 11: Influence of the chemical composition, especially the Cr content, on the oxidation resistance of steels37. All compositions are in wt. (%) (Dienst 1978)

2.5.1.2 Nickel

Nickel as alloying element in stainless steel is a strong austenite former which offers resistance to reducing solutions but is readily attacked by oxidizing solutions (Kutz

2002). Table 5 further shows that 304,304L and 304H type stainless steels all have the same minimum nickel content limit of 8.0 wt%. The maximum nickel content limits do however differ with 304L type austenitic stainless steel permitting up to 12.0 wt% nickel, compared to the maximum nickel content limit of 10.5 wt% for standard 304 and 304H. It is however important to note that given the high cost of nickel it is not unusual for all three grades to be produced with their nickel content close to the minimum limit of 8.0 wt%. There is therefore little practical difference in their nickel content (Atlas steels, 2011). The addition of nickel increases creep resistance as a result nickel superalloys, which have higher nickel contents, therefore have a comparatively better creep resistance than the austenitic stainless steels (Plaut et al., 2007). Austenitic stainless steels are widely used because they are easier to process and less expensive, by a factor of 6 to 60, depending on the alloy, than the nickel superalloys (Plaut et al., 2007).

2.5.1.3 Carbon

Table 5 taken from ASTM A240/A240M shows Type 304 has a specified maximum carbon content of 0.07 wt% and Type 304L has a specified maximum carbon content of 0.03 wt%. Both Type 304 and 304L do not have minimum carbon content values specified. The 304H type stainless steel has specified carbon content of 0.04 - 0.10 wt%. The Type 304H stainless steel is used in high temperature service because the minimum carbon content requirement of 0.04 - 0.1 wt% in Type 304H guarantees higher allowable stresses i.e. strength, at elevated temperatures above 540°C (Albright *et al*. 2009). It is important to note that the carbon contents of types 304 and 304H overlap between the ranges 0.04 - 0.07 wt%. This overlap in carbon levels between the three grades makes it more economical for mills to melt steel to only two steels with different levels of carbon and dual certify (Kutz 2002). As a result a type 304 stainless steel with less than 0.03 wt% carbon can be dual certified as a type 304L and a type 304 stainless steel. Similarly, a type 304 with a carbon wt% of 0.04 or higher can be dual certified as a type 304H and a type 304 stainless steel.

2.5.1.4 Nitrogen

Nitrogen as an alloying element is an austenite former. The last compositional difference is that 304H does not contain nitrogen whereas the Types 304 and 304L have a 0.10 wt% nitrogen content maximum limit specified. The use of the AOD process for refining steels has made it possible to add a small, precisely controlled amount of nitrogen because the addition of nitrogen increases the room temperature tensile properties without adversely affecting the intergranular corrosion resistance (Kutz 2002). With care in annealing practice, it is now possible to produce type 304 stainless steel with low enough carbon to meet the type 304L specification, yet with a high enough yield strength to meet type 304 requirements (Kutz 2002).

Table 5: Chemistry of 304, 304L and 304H austenitic stainless steel (ASME boiler and pressure vessel code, 2010)

Grade	UNS Number	Carbon (%)	Chromium (%)	Nickel (%)	Molybdenum(%)	Nitrogen (%)
304	S30400	0.07 max	17.5 – 19.5	8.0 – 10.5	-	0.10 max
304L	S30403	0.030 max	17.5 – 19.5	8.0 – 12.0	-	0.10 max
304H	S30409	0.04 – 0.10	18.0 – 20.0	8.0 – 10.5	-	-

2.5.2 Differences in mechanical properties

Mechanical property specification differences are illustrated in Table 6 taken from AMSE 2010, A312. Table 6 shows that the elongation, Brinell and Rockwell hardness requirements to be identical for the 304, 304L and 304H stainless steels. The yield and tensile strength for 304 and 304H at 20°C or 21°C are equal with the minimum yield strength being 205 MPa and a minimum tensile strength being 515 MPa. The 304L has a minimum yield and tensile strength requirement of 170 MPa and 485 MPa respectively at 20°C or 21°C which lower than values for 304 and 304H Type stainless steel at the same temperature. The maximum allowable stress values shown in Table 7 for exposure in the temperature range 65°C – 825°C for types 304 and 304H are also equal to each other while the values obtained for 304L are lower in the same 65 - 825°C temperature range. There is therefore no difference in maximum allowable stresses at high or low temperature service for a type 304 stainless steel dual certified as type 304 and 304H.

Table 6: Mechanical properties of types 304, 304L and 304H austenitic stainless steel at 20 or 21°C (ASME boiler and pressure vessel code, 2010)

Grade	UNS	Tensile Strength (MPa) min	Yield Strength (MPa) min	Elongation (%) min	Brinell Hardness (HB) max	Rockwell Hardness (HRB) max
304	S30400	515	205	40	201	92
304L	S30403	485	170	40	201	92
304H	S30409	515	205	40	201	92

Table 7: Maximum allowable stress values for types 304, 304L and 304H austenitic stainless steel for temperature range 65-825°C (ASME boiler and pressure vessel code, 2010)

Grade	**UNS**	**Maximum Allowable Stress Values *S* for Ferrous Materials (MPa)**									
		-30 to 65°C	**150°C**	**300°C**	**375°C**	**450°C**	**525°C**	**600°C**	**675°C**	**750°C**	**825°C**
304	S30400	138	130	116	109	103	98	65.4	32.9	17.2	8.73
304L	S30403	105	88.1	72.3	68.6	65.7	60.2	32.9	-	-	-

As aforementioned, the compositional carbon restrictions i.e. having a minimum carbon content of 0.04 wt% and the heat treatment restrictions specified for Type 304H ensure high and reproducible creep rupture strengths at elevated temperatures (Sedriks 1996). Due to its lower carbon content, Type 304L has a lower yield and tensile strength than that of Type 304 and Type 304H which have higher carbon contents. Figure 12, taken from API 530, uses the same stress curves for types 304 and 304H. In figure 12, It is important to note that above 538°C, the stress values for type 304 only apply if the carbon content is 0.04 wt% or higher i.e. thereby meeting the minimum carbon requirements for type 304H.

Key

1 Specified minimum tensile strength
2 Tensile strength
3 Specified minimum yield strength
4 Yield strength
5 Elastic allowable stress, σ_{el}
6 Rupture allowable stress, σ_r
7 Limiting design metal temperature
8 Minimum rupture strength
9 Average rupture strength
10 Elastic design governs above this stress

NOTE Above 538 °C, the stress values for type 304 apply only if carbon content is 0,04 % or higher.

Figure E.12 — Stress curves (SI units) for ASTM A 213, ASTM A 271, ASTM A 312 and ASTM A 376 types 304 and 304H (18Cr-8Ni) stainless steels

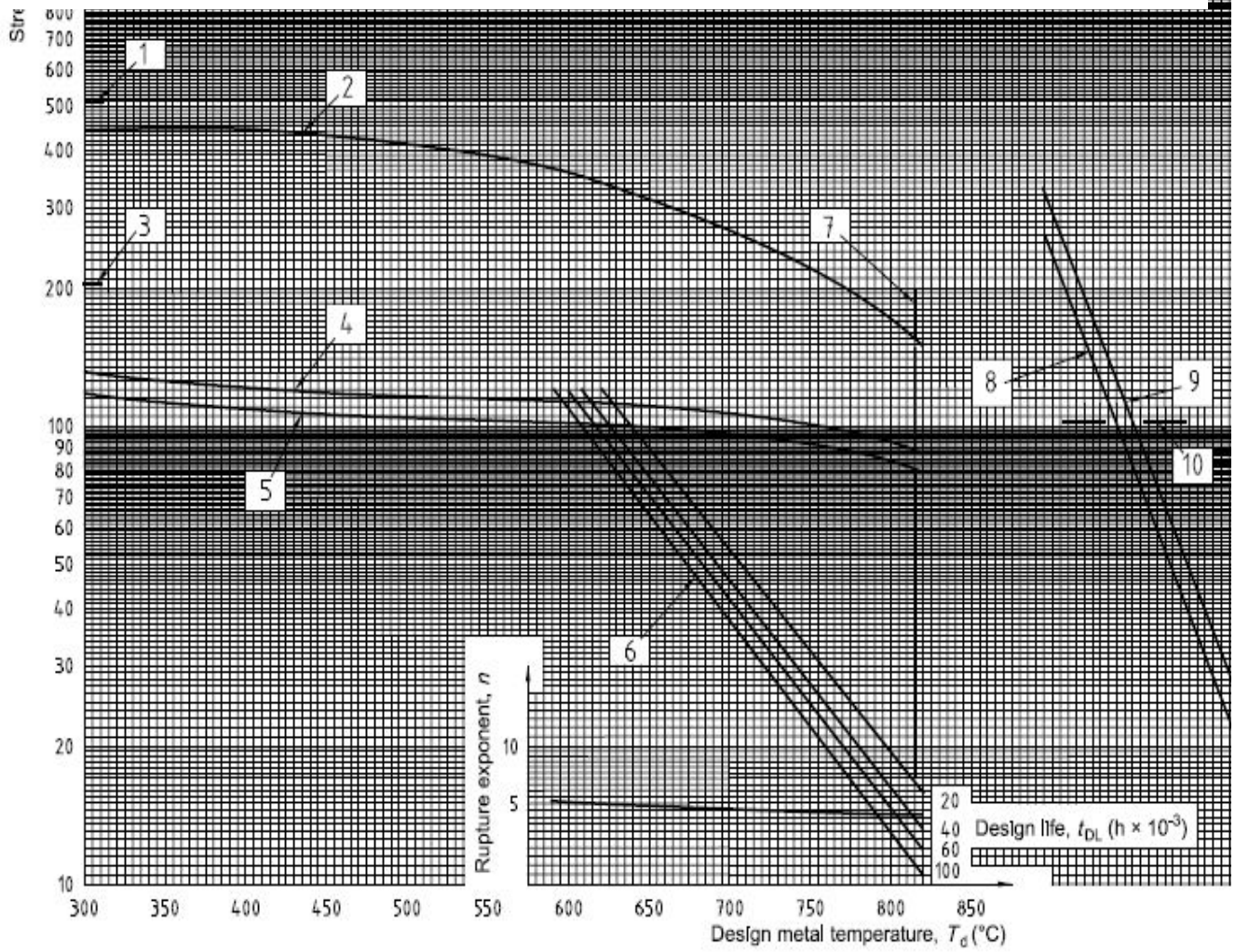

Figure 12: Stress rupture curves for ASTM 312 Type 304 and 304H (American Petroleum Institute 530)

2.6 Shielded metal arc welding (SMAW) process

Shielded metal arc welding (SMAW) is one of the oldest welding processes and is the simplest and one of the most versatile for welding ferrous base metals and several non-ferrous base metals (8th Edition of the AWS Welding Handbook vol. 2, 1998). It is also the most commonly used welding process in fabrication and maintenance jobs (Kaushish 2008). The SMAW method is commonly called Manual Metal Arc Welding (MMA), referring to the fact that in a majority of cases it is carried out by a welder guiding the stick electrode (Svensson 1994). The shielded metal arc welding (SMAW) process as illustrated in Figure 13 uses a covered electrode consisting of a core wire around which a concentric clay-like mixture of silicate binders and powdered materials is extruded. Materials such as such as fluorides, oxides, carbonates, metal alloys and cellulose are some of the common powdered materials used in the clay-like covering. The main coating types that exist can be divided into acid, cellulosic, rutile and basic electrodes with each the electrodes possessing characteristics and mechanical properties typical to the type (Svensson 1994). The covered electrodes are produced in diameters normally ranging from 2 to 8 mm with the smaller diameters used with low currents for joining thin sections in all welding positions; and the larger electrode diameters used with high currents to achieve greater deposition rates when welding in the flat and horizontal positions (AWS Welding Handbook, 1998). The covering around the core wire is the source of arc stabilizers, gases to displace air, metal and slag to protect, support, insulate the hot weld metal and allows the addition of alloying elements (Svensson 1994). The top section of the electrode core wire is however not covered with the covering and is left bare. This bare section of the electrode is clamped in an electrode holder, which in turn is connected to a power source by a welding cable. The work is connected to the other power source terminal. The arc is initiated by touching the electrode tip against the work and then drawing it slightly. The current passes through the metal rod and tip of the electrode is heated by resistance heating and action of the arc (Svensson 1994). Under the intense heat of the arc of about 5000°C, a small part of the base metal, the core wire and covering of the electrode melt (Kaushish 2008). The molten base metal, core wire, and metal powders in the covering coalesce

to form the weld. Cleaning the weld bead after each pass is required, and is done by removing the slag covering that insulates and protects from is required after each pass with a chipping hammer.

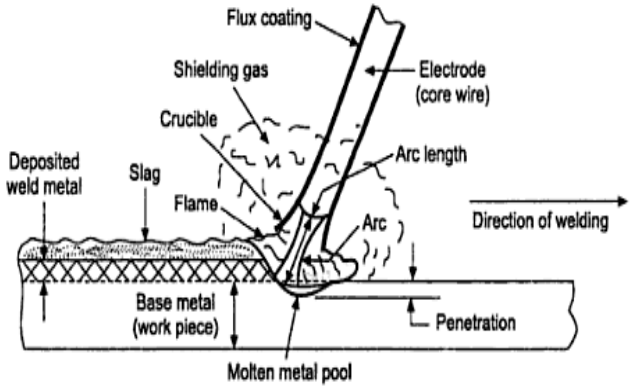

Figure 13: Shielded Metal Arc Welding Process (Kaushish 2008)

The SMAW process has many advantages, some of these advantages are: the simplicity and lightness of the equipment. This makes it easy to transport and solid-state power sources are available which are small and low in weight enabling them to be manually carried to job locations where the welds to be made are in confined locations or remote from heavy power supplies. The low operational cost associated with SMAW is often the most attractive advantage. These are just a few of the reasons why the SMAW process has a wide application in the construction, shop fabrication, pipeline and maintenance industries. The current range used for SMAW may vary between 50 and 2000 Amps with voltages varying between 10 and 50 volts (Kaushish 2008). SMAW remains dominant because of its simplicity and versatility. Many engineers and welders are comfortable with the process as a result of long experience with it. However, other more productive arc welding processes are replacing SMAW in many applications such as semiautomatic submerged arc welding (SAW) used in the welding of thin sheet and thick plate which is used in the fabrication of heavy sectioned pressure vessels (AWS Welding Handbook vol. 2, 1998).

2.7 Importance of inter-pass temperature

The welding inter-pass temperature is defined as the temperature of the material in the weld area immediately before the second pass and each subsequent pass of a multiple pass weld is made. According to Funderburk (1998), the inter-pass temperature affects the mechanical and microstructural properties of weldments because both yield and ultimate tensile strength (UTS) of the weld metal are a function of inter-pass temperature. The work of Svensson & Hidesjo (1999), shown in table 8, supported this because in their work, the yield and tensile strength dropped and as the interpass temperature increased, while the impact toughness did not vary to any significant degree.

Table 8: Effect of interpass temperature on the mechanical properties (Svensson & Hidesjo, 1999)

Weld no	Interpass temp (°C)	Yield strength (MPa)	Tensile strength (MPa)	Yield/tensile strength ratio	Impact toughness at -60°C (J)
12	50	1003	1008	0.99	55
13	110	978	987	0.99	48
14	250	832	932	0.89	57

The minimum inter-pass temperature is to be measured in the base metal no less than 75 mm from the point of welding. If the requirement is to control the maximum inter-pass temperature, the temperature measurements has to be taken 25 mm from the weld toe (Funderburk 1998).

2.8 Post solidification phase transformation – The effect of solidification mode on the delta ferrite microstructure in austenitic stainless steels

According to Kou (2003), it is important to understand post-solidification phase transformations because, these phase transformations can change the solidification microstructure and properties of the weld metal. Understanding post-solidification phase transformations involving the ferrite-to-austenite transformation of austenitic stainless steel in the weld metal is therefore important for the microstructural evaluation in this research project. The development of weld metal microstructure in austenitic stainless

steels is shown in Figure 14. The delta ferrite can be (*a*) interdendritic, (b) vermicular or (c) lathy. Figure 14 also shows (d), a schematic vertical or isoplethal section of the Fe-Cr-Ni ternary phase diagram at 70 wt% Fe and above 1200°C. This has also been called a Fe-Cr-Ni pseudo-binary phase diagram. The apex in figure 14d, point 1 in the isoplethal section, is the start of the of the three-phase eutectic triangle. The triangle is formed by points 1, 2 and 3 and the three phases of the three-phase eutectic triangle are Liquid (L), austenite (γ) and delta ferrite (δ).

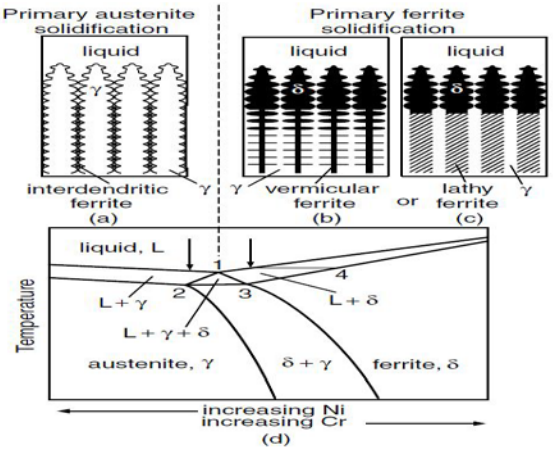

Figure 14: Solidification and post solidification transformation in Fe-Cr-Ni welds (a) interdendritic ferrite, (b) vermicular ferrite and (c) lathy ferrite (d) a schematic vertical or isoplethal section of the Fe-Cr-Ni ternary phase diagram at 70 wt% Fe and above 1200°C (Kou 2003)

Figure 14 shows that for all compositions that are on the left of the apex, austenite will be the primary solidification phase and those on the right of the apex will solidify with delta ferrite as the primary solidification phase before transformation to austenite. Therefore for the nickel-rich alloy on the left-hand side of the apex of the three-phase eutectic triangle, austenite (γ) will be the primary solidification phase. The light dendrites shown in figure 14*a* are austenite, while the dark particles between the primary dendrite arms is the delta-ferrite (δ) that forms when the three-phase triangle is reached during the terminal stage of solidification. This delta ferrite which is found in between the austenite dendrites is called interdendritic delta ferrite. For dendrites with long secondary arms, interdendritic ferrite particles can also form between secondary dendrite arms. For a chromium-rich alloy i.e. an alloy on the right-hand side of the apex

of the three-phase eutectic triangle, delta ferrite (δ) will be the primary solidification phase. The dark dendrites shown in figure 14b are therefore delta ferrite that is first to form. The core of the delta-ferrite dendrites, which forms at the beginning of solidification, is richer in Cr (point 4), while the outer portions, which form as temperature decreases, have lower chromium contents. As the chromium rich alloy cools into the ($\delta + \gamma$) two-phase region, the outer portions of the dendrites having less Cr transform to austenite, thus leaving behind Cr-rich "skeletons" of d-ferrite at the dendrite cores. This skeletal ferrite is called vermicular ferrite. In addition to vermicular ferrite, primary delta ferrite dendrites can also transform to lathy or lacy ferrite upon cooling into the ($\delta + \gamma$) two-phase region, as shown in figure 14c.

Plaut *el al*. (2007) and Kou (2003) further elaborate on the primary ferrite and austenite solidification modes and their transformation path in greater detail. According to Plaut and Kou, the primary austenitic solidification mode can be sub-divided into two modes. The two modes of primary austenite solidification modes are namely;

- Primary austenitic solidification mode (A), which follows the solidification sequence L $\rightarrow$ L + $\gamma \rightarrow \gamma$ phase transformation. In this solidification mode, no delta ferrite exists in the microstructure.
- Austenitic-ferritic solidification mode (AF), where the ferrite present is eutectic ferrite and follows the solidification sequence L$\rightarrow$ L + $\gamma \rightarrow$ L+ γ + $\delta \rightarrow \gamma$ + δ phase transformation.

The primary ferrite solidification mode can be further sub-divided into three modes and these modes are namely;

- Ferritic-austenitic solidification mode (FA), where the ferrite present is vermicular (skeletal) ferrite. Mode FA follows the solidification sequence L$\rightarrow$ L + $\delta \rightarrow$ L + δ + $\gamma \rightarrow \gamma$+ δ phase transformation.
- Ferritic-austenitic solidification mode (FA), where the ferrite is a lathy ferrite. Here the two FA modes follow the same solidification sequence L$\rightarrow$ L + $\delta \rightarrow$ L + δ + $\gamma \rightarrow$ γ + δ phase transformation.

- Ferritic solidification mode is the primary ferrite solidification mode (F), where the ferrite is present as Widmanstätten patterns. Mode F follows the solidification sequence L → L + δ → δ phase transformation. In this mode, no austenite exists in the microstructure.

Figure 15 shows these five above mentioned solidification modes and the different ferrite morphologies in greater detail. The solidification mode sequence can also be predicted using the chromium and nickel equivalent ratio apart from predictions using the Fe-Cr-Ni pseudo-binary phase diagram (Plaut, Herrera, Escriba, Rios & Padihla, 2007). The work of Korinko & Malene (2001) recommended that a calculated Cr_{eq}/Ni_{eq} ratio range of 1.52 to 1.9 be maintained to control the primary mode of solidification as ferrite-austenite (FA) in order to prevent solidification cracks in type 304L stainless steel. Primary austenite solidification will occur when the Cr_{eq}/Ni_{eq} ratio is less than 1.48 and primary ferrite solidification will occur when this ratio is greater than 1.48 (Folkhard, Rabensteiner, Perteneder, Schabereiter & Tosch, 1984). Earlier work by Elmer *et al.* (1989) supports the work of Korinko and Malene (2001) and Folkhard *et al.* (1984) by pointing out that alloys with a low Cr_{eq}/Ni_{eq} ratio solidify with austenite as the first phase before any ferrite, prior to the alloy entering the three-phase eutectic triangle of the Fe-Cr-Ni pseudo-binary phase diagram, and furthermore that their ferrite content will decrease with increasing in cooling rates because, solute redistribution during solidification is reduced when cooling rates are high. These low Cr_{eq}/Ni_{eq} ratio alloys will therefore not have a sufficient amount of delta ferrite to prevent hot solidification cracking. On the other hand, when the Cr_{eq}/Ni_{eq} ratio of the alloy is high, the alloy will solidify with ferrite as the first phase before any austenite, prior to the alloy entering the three-phase eutectic triangle of the Fe-Cr-Ni pseudo-binary phase diagram. Furthermore, the ferrite content of the high Cr_{eq}/Ni_{eq} ratio alloy will increase with increasing cooling rates because the delta ferrite to austenite transformation has less time to occur at high cooling rates. These high Cr_{eq}/Ni_{eq} alloys will therefore contain sufficient delta ferrite in their structure to prevent hot solidification cracking.

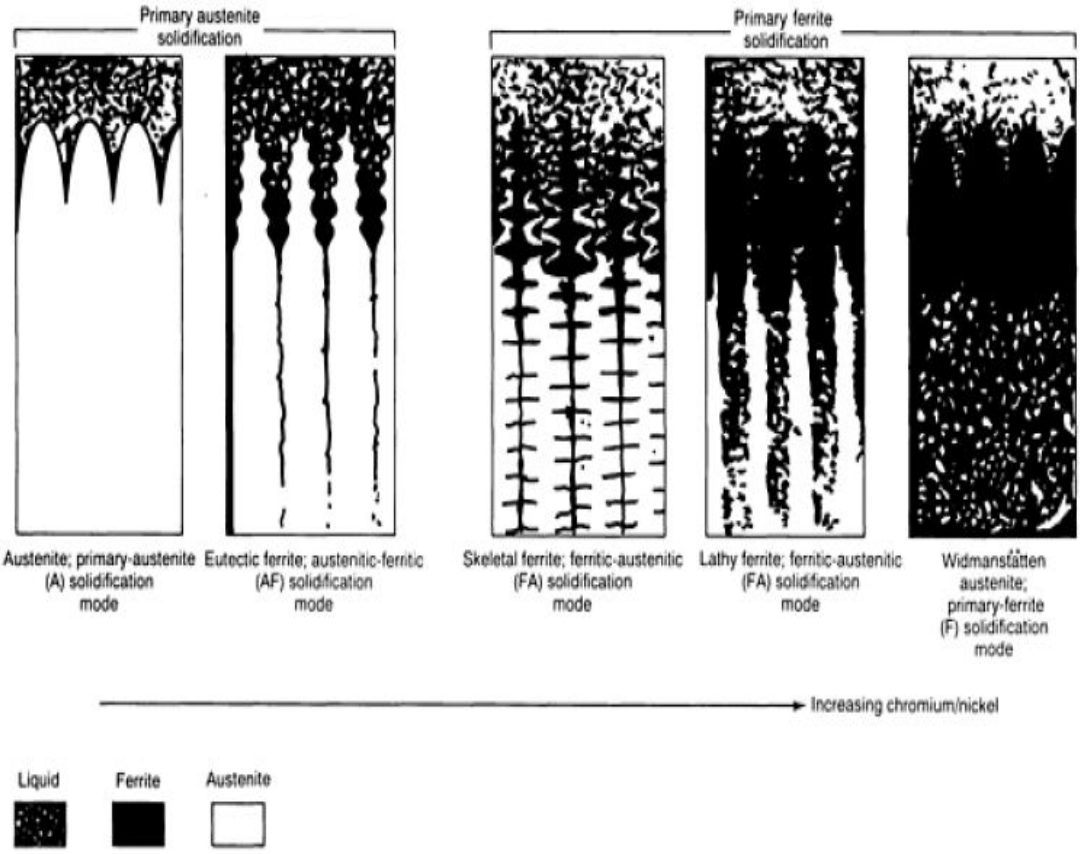

Figure 15: Solidification and transformation modes and resultant ferrite morphologies (Kou 203)

2.9 Effect of constitutional supercooling on the weld metal matrix microstructure

The theory of constitutional supercooling by Chalmers and Rutter (1953) describes the breakdown of a planar solid/liquid interface during solidification. Losert, Shi and Cummings (1998) also experimentally investigated the evolution of a dendritic pattern from a planar solid–liquid interface during directional solidification of a binary alloy. Losert *et al.* (1998)state that when alloy solidification occurs rapidly, the usually smooth solid–melt interface becomes unstable and transforms to a pattern of shallow cells, deep cells, or an array of dendrites with side-branch structure, depending on the growth conditions. The solidification front instability is caused by constitutional supercooling which is a condition which can occurs during solidification when the liquid ahead of the solidification front is supercooled below its freezing temperature, even though it is hotter than liquid at the front. According to Kou (2003) this is termed constitutional

supercooling, to emphasize that it arises from variations in liquid composition. As constitutional supercooling increases, the solidification mode of the matrix will also change. As seen in figure 16 the change will happen from planar (region A) to cellular (region B) and from cellular to columnar dendritic (region C) and then to region D where a equiaxed dendritic structure will exist. The region where dendrites, whether they be columnar or equiaxed, and the liquid phase coexist is often called the mushy zone. At a very high degree of constitutional supercooling the mushy zone can become so wide that heterogeneous nucleation of equiaxed dendrites is easier than columnar dendrites that would have to stretch all the way across the mushy zone (Kou 2003).

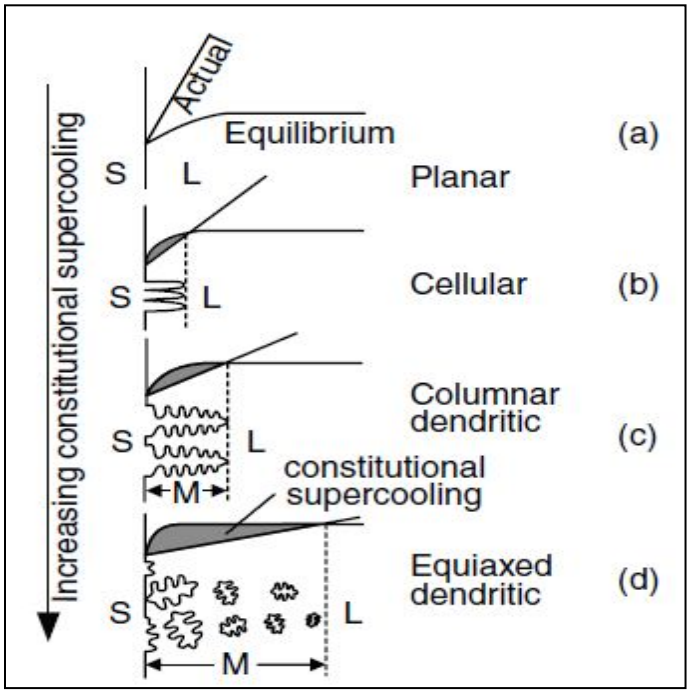

Figure 16: The effect of constitutional super-cooling on solidification mode on the (a) planar, (b) cellular, (c) columnar dendritic and (d) equiaxed dendritic grains 0f the weld metal (Kou 2003)

The Schematic in figure 17 and microstructures in figure 6 show more clearly the effect of constitutional supercooling on the microstructure within the grains of the weld metal. The changes in solidification mode of the matrix from (a) planar to (b) cellular , columnar (c) dendritic, and (d) equiaxed dendritic can be seen as the degree of constitutional supercooling at the pool boundary increases. Constitutional supercooling therefore

increases in figure 16, 17 and 18 from a-d. Heterogeneous nucleation aided by constitutional supercooling promotes the formation of equiaxed grains in the weld metal. While the solidification mode can vary from one weld to another as shown in figure 17 and figure 18, it can also vary within a single weld from the fusion line to the centerline as shown in figure 19 and 20. These multiple solidification modes within a single weld from the fusion line (FL) to the center line (CL) can be explained by the G/R ratio equation 3:

Equation 3: G/R ratio equation (Kou 2003)

$$\left(\frac{G}{R}\right)_{CL} \ll \left(\frac{G}{R}\right)_{FL} \quad (3)$$

Where:

R is the growth rate

G is the temperature gradient

CL is the centre line of the weld

FL is the fusion line of the weld

According to the G/R ratio equation, the ratio *G*/*R* decreases from the fusion line towards the centerline (Kou 2003). As a result of this decrease of the G/R ratio from the fusion line to the centre line the increase in constitutional supercooling may change the solidification mode from planar to cellular, columnar dendritic, and equiaxed dendritic across the fusion zone, as depicted in figure 17 and figure 18 where the grains are shown to grow epitaxially from the fusion line. The grains first initially grow with the planar mode from the fusion line, along the growth direction <100> of the base-metal grain. A short distance away from the fusion line, solidification changes to the cellular mode and even further away from the fusion line, solidification again changes to the columnar dendritic mode. At this point the cells evolve into dendrites and their side arms will start to block off the neighboring cells. This evolution of the dendrites will continue until supercooling becomes so great that equiaxed dendrites nucleate and grow,

blocking off the columnar dendrites. The equiaxed dendrites usually nucleate close to the centre line of the weld (Kou 2003).

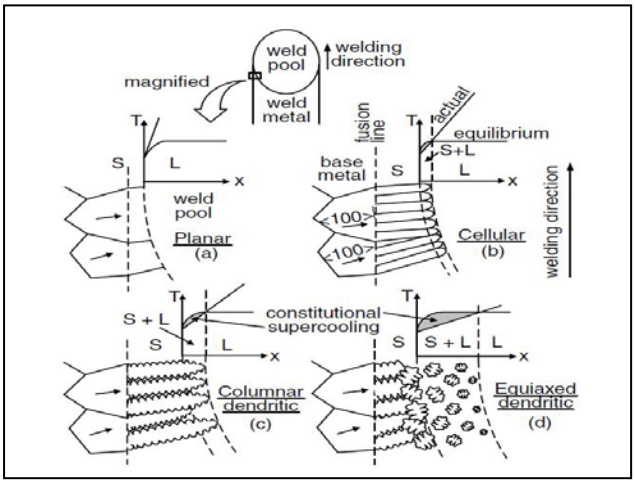

Figure 17: The effect of constitutional supercooling on solidification mode during welding resulting in (a) planar, (b) cellular, (c) columnar dendritic and (d) equiaxed dendritic grains (Kou 20003

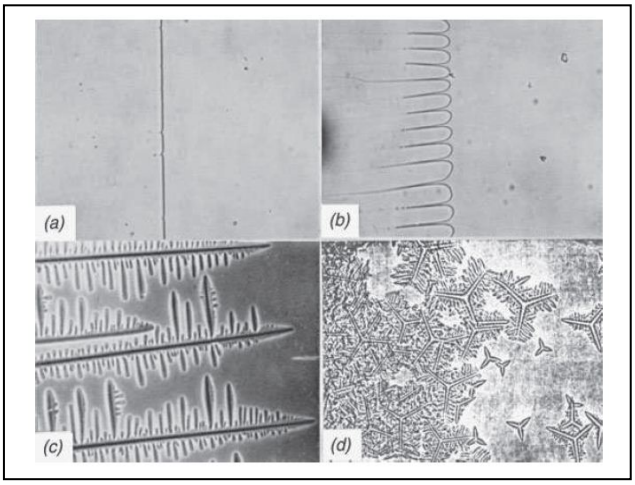

Figure 18: Microstructures depicting the effect of constitutional supercooling on solidification mode during welding planar resulting in (a) planar, (b) cellular, (c) columnar dendritic and (d) equiaxed dendritic grains (Kou 2003)

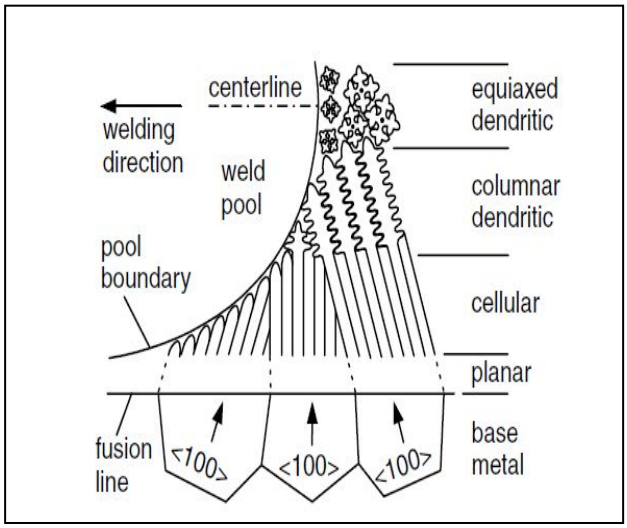

Figure 19: The variations in solidification mode in a single weld across the fusion zone (Kou 2003)

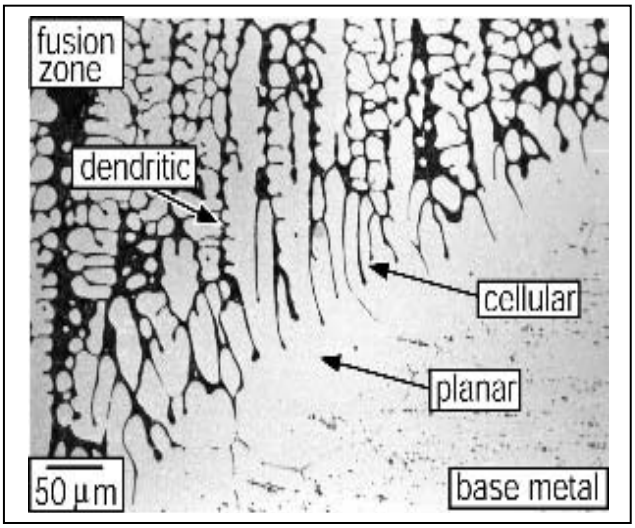

Figure 20: Microstructure showing the variations in solidification mode in a single weld across the fusion zone (Kou 2003)

2.10 Sigma phase transformations

In the as-welded condition type 304H stainless steels do not normally contain any sigma phase because the rapid cooling rate retains the microstructure existing at very high temperature where sigma phase does not form. However after long-term exposure at elevated service temperatures between 550-900°C delta ferrite in the weld metal transforms into sigma, chi and laves phases (Castro & de Cadanet, 1975). Of the aforementioned three delta ferrite transformation phases, sigma phase has been studied the most. Transformation to sigma phase is most rapid in the 800-850°C range. Sigma phase forms in austenitic stainless steels containing more than 16 wt% chromium, but less than 32 wt% nickel. The sigma phase has a complex tetragonal structure with 30 atoms per unit cell (Sedriks 1996). Sigma forms very slowly when forming from the austenite phase in the 300 series austenitic stainless steels, first developing at the grain boundaries. Its formation is favoured by high chromium contents, silicon, molybdenum, titanium, small grain size and cold work (Sedriks 1996). The sigma phase is the most deleterious of the delta ferrite transformation phases but can require exposure times of thousands of hours, or even of several ten thousands of hours at the temperature range of its formation for the mechanical consequences of sigma formation to become apparent. The presence of sigma phase increases hardness, but it decreases ductility, notch toughness and localized pitting corrosion resistance. The loss of ductility and toughness due to sigma phase, is generally intolerant at temperatures under 120-150°C but has little effect on these properties in the temperature range where it forms (Jorge, Hau & Seijas, 2006). The embrittlement resulting from the nucleation of ferrite is important only when this phase is present in sufficient quantity to form a continuous network, as the sigma phase then creates a path for brittle fracture.

2.10.1 Factors that Influence delta ferrite to sigma phase transformation in weld metal

There are a number of factors that influence the presence of delta ferrite and its quantity in weld metal. For ferrite to be formed in an austenitic weld, certain compositional and microstructural conditions are required.

2.10.1.1 Compositional conditions

The structure of a weld after complete cooling depends on the quantity of ferrite which formed at very high temperatures, and consequently upon relative proportions of austenite formers and ferrite formers. The combination of the base material and welding consumable can be either strong, intermediate or non-ferrite forming. As mentioned, sigma phase formation is promoted by strong ferrite formers and suppressed by strong austenite formers.

2.10.1.2 Structural conditions

The microstructure of welds cooled in still air can facilitate the formation of compounds in steel, for example sigma phase. These compounds have such a composition that they would not form in the same alloy when forged and quenched from annealing temperatures. This is because segregation during cooling can locally raise the concentration of ferrite formers, therefore promoting the formation of ferrite and sigma type compounds without the necessity of extensive diffusion. This is especially true in the case of austenitic-ferritic welds, because delta ferrite is richer in ferrite formers than austenite; moreover diffusion rates are higher in ferrite than what they are in austenite. Transformation to sigma phase is therefore more rapid when it is formed from ferrite than austenite. It is even possible that, when the weld deposit contains a high proportion of elements that accelerate the formation of intermetallic compounds, the ferrite that is present from the initial weld runs is transformed into sigma phase by reheating in to the 550-900°C sigma forming temperature range during deposition of subsequent passes. This transformation can happen by eutectoid type decomposition (Castro & de Cadanet, 1975).The schematic in figure 19a-d, reveals the transformation sequence of delta ferrite (δ) islands into sigma phase (σ) and the precipitation sequence of sigma phase on grain boundaries as exposure time increases. In figure 21a, the islands of delta ferrite that have nucleated in the austenite matrix are observed. In 21b, shows that sigma phase is starts to transform within the nucleated delta ferrite islands. Figure 21c, shows that that next preferred sigma phase nucleation site is on the triple points of the grain boundaries. Figure 21d, shows that once the delta ferrite islands and triple points

are saturated with sigma phase, the next preferred sigma phase nucleation site is the actual grain boundaries. It is important to note that the precipitation mechanisms at the different sites are not the same, for instance; the delta ferrite seems to decompose by means of a eutectoid reaction (ferrite -> sigma + austenite) while at the grain boundaries and triple points precipitation occurs by the traditional precipitation mechanism (Plaut *et al*. 2007).

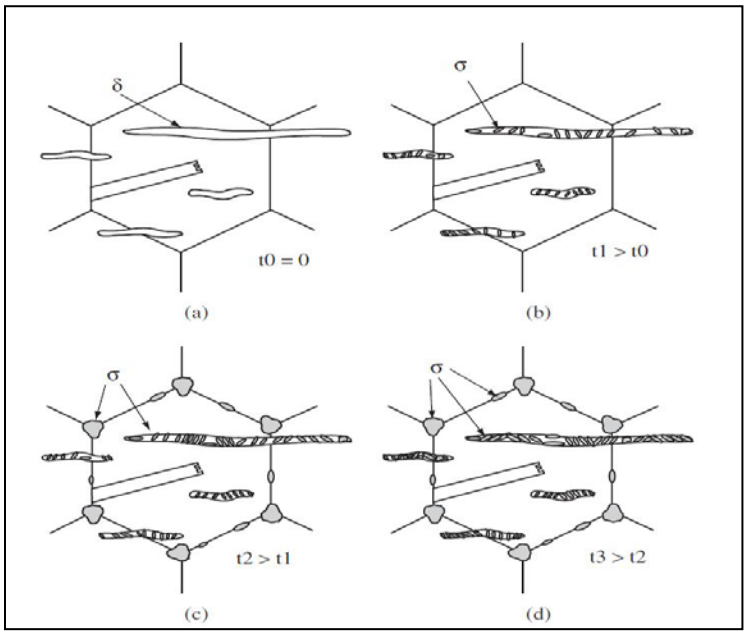

Figure 21: Sigma phase precipitation in an austenitic stainless steel containing delta ferrite (Escriba el al, 2006)

2.11 Measurement & Predictive Estimation of Delta Ferrite in Weld Metal Deposits

2.11.1 Methods and difficulties in measurement of delta ferrite

There are several methods of measuring ferrite; some of the commonly used methods are:

- Metallographic evaluation
- X-ray diffraction
- Magnetic permeability
- Magnetic determination
- Calculation of ferrite from chemistry.

2.11.1.1 Metallographic evaluation

The metallographic method was initially used as the primary method to quantify the amount of delta ferrite present in weld metal.
Difficulty: The statistical accuracy of this method, which was done by point counting, was however highly influenced by the ferrite colony size. The introduction of automated techniques had done little to improve upon operator variances. The biggest deterrent from using this method to quantify ferrite content for the entire sample was the observation that changes in ferrite content within the same substrate made quantification representative of the entire sample difficult.

2.11.1.2 X-ray diffraction

The use of x-ray diffraction as a ferrite measurement technique can also be used.
Difficulty: The limitation with this technique is that the diffraction patterns tend to diffuse in nature and are subject to interpretation which makes this method very subjective. Consistent accuracy is therefore a challenge using this technique.

2.11.1.3 Magnetic permeability measurements

Ferrite quantification through magnetic permeability measurements is another method that can be utilized to quantify the amount of ferrite present. Magnetic permeability is proportional to ferrite percentage or ferrite number and can be measured with the aid of a Severn Gage. This method requires that a magnetic field be induced on the substrate and the resulting field strength be measured to establish the magnetic permeability. With this technique, the overall permeability of a two phase alloy containing one ferromagnetic and one non-ferromagnetic phase depends on the individual permeability, the content and demagnetization factor of the ferromagnetic phase at a given strength of the magnetizing field (Priceputu et al. 2011).

2.11.1.4 Magnetic determination

The magnetic determination method can also be used to quantify the ferrite present. Magnetic determinations are done with the use of a ferrite scope to quantify the amount of ferrite present in the sample and give the ferrite content by producing a ferrite percentage or ferrite number. An experiment by Lundin, Chou & Sullivan (1980) measured the ferrite content using this technique. In order to minimize the error due to weld metal inhomogeneity, the average value of 15 determinations was taken from different locations in the centre, and four inches along the pad was used. The ferrite number readings were made on all ground pads using an Aminco-Brenner Magne Gage.

2.11.1.5 Calculation of ferrite from chemistry

Ferrite quantity can also be predicted from the weld metal chemistry. Ferrite determination from chemistry has been extensively used in industry and is considered a statistically viable option for ferrite prediction. Schaeffler, DeLong and the World Research Council (1992) introduced constitution diagrams as a non-destructive method to relate alloy composition to the amount of ferrite present in an alloy. Schaeffler-DeLong and Delong-WRC diagrams are simple graphical methods as long as the values calculated are not too high. Schaeffler (1949) first studied quantitatively the effect of these elements upon the structure, and particularly upon the ferrite content of weld metals deposited under well-defined thermal conditions (Castro & de Cadanet, 1975). Schaeffler (1949) published what has become known as the Schaeffler diagram in Figure 22. This diagram proposed a relationship among alloy elements that promote the formation of ferrite (chromium-equivalent elements) and elements that promote the formation of austenite and the suppression of ferrite (nickel-equivalent elements). To use this diagram, both the chromium and nickel equivalents are first calculated from the composition of a given weld bead and these equivalents are then plotted as coordinates on the Schaeffler constitution diagram. This allows an estimated weld-metal microstructure to be determined from the boundaries given in the diagram (ASM, 1993).

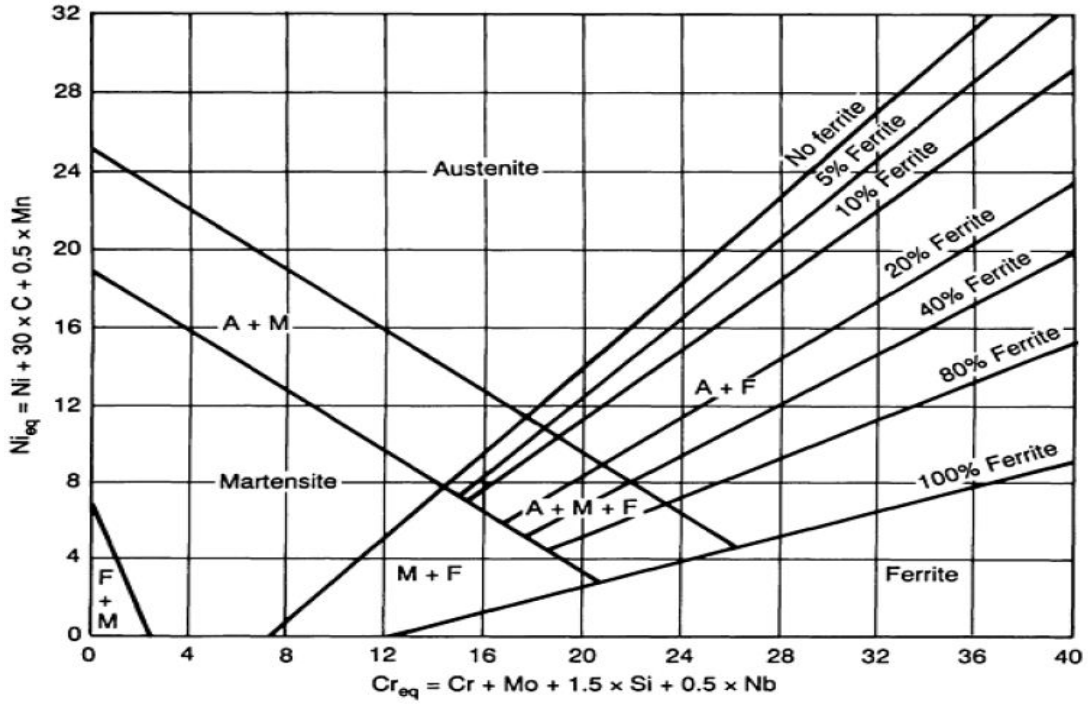

Figure 22: Schaeffler constitution diagram for stainless steel weld metal (Schaeffler, 1949)

DeLong (1974) recognized the effect of nitrogen in promoting austenite at the expense of ferrite. This is because nitrogen, as a strong austenite phase promoter, retards the formation of ferrite. He developed the DeLong diagram in figure 23 that covered a more-restricted composition range than the Schaeffler diagram but included the effect of nitrogen. Delong's work therefore increased the accuracy of the Schaeffler diagram and revealed that, for a given chemistry, his estimations predicted increased ferrite over that of Schaeffler.

In 1974 the DeLong diagram in figure 23 was published and in that same year, the measurement of ferrite in austenitic stainless steel weld metals was standardized by the ANSI/AWS A4.2 specification. This meant that ferrite number determinations moved towards magnetically determined ferrite numbers (FN), rather than the metallographically determined "percent ferrite" used by the Schaeffler diagram (ASM 1993).

The DeLong diagram became part of the "Boiler and Pressure Vessel Code" of the American Society of Mechanical Engineers (ASME) but was subsequently replaced by the WRC diagrams in the 2005 publication of the ASME boiler pressure vessel code.

The Schaeffler and Delong diagrams were replaced by the WRC-1988 and subsequently the WRC-1992 diagram in figure 24 because they were found to contain a number of flaws.

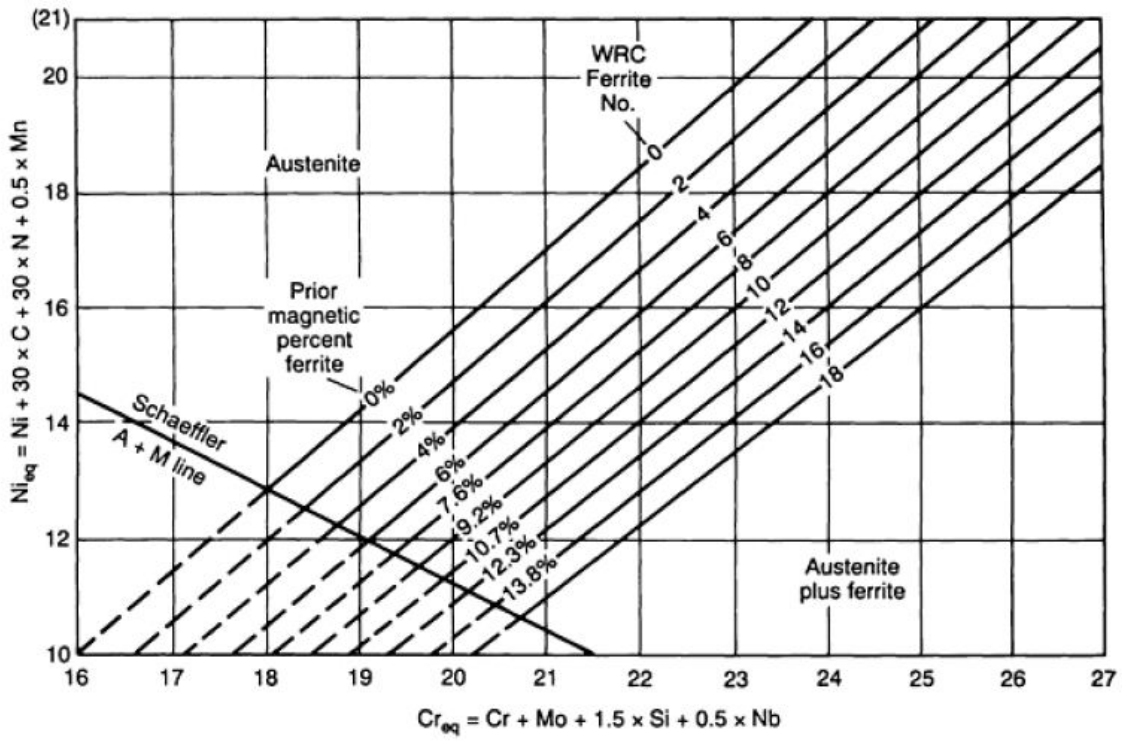

Figure 23: DeLong constitution diagram for stainless steel weld metal, the Schaeffler austenite-martensite boundary is included for reference (Long & De Long, 1974)

According to Siewert, McCowan and Olson (1989) the WRC-1988 diagram accounted for the following flaws in the Schaeffler and DeLong diagrams:

(i) The fact that the DeLong diagram is essentially a finely tuned subset of the Schaeffer range, designed specifically for the 300-series stainless steel welds containing small amounts of ferrite, was the first flaw. The refined nature of the DeLong diagram forced engineers to reference the Schaeffler diagrams for alloys containing more than 15 wt% ferrite. The DeLong diagram also gives a relationship between the ferrite number and magnetic percentage ferrite content. For ferrite content percentages of 4 and less, the ferrite number will be equivalent to the ferrite content percentage.

(ii) Secondly, the Schaeffler diagram did not have the improved degree of accuracy or accountability for nitrogen that the DeLong diagram developed. Earlier work by Kontecki and Szumachowski (1984) also highlighted that the effect of manganese on ferrite formation had also been incorrectly established. This work also concluded that the existing nickel equivalent of the WRC-DeLong diagram resulted in consistently underestimating weld metal ferrite for high manganese weld metals. A modification of the nickel equivalent for the WRC-DeLong diagram by deleting the manganese factor and inserting a small constant value regardless of manganese level, provided reasonable agreement between calculated and measured ferrite numbers over the manganese range considered. They, Szumachowski and Kontecki, also found in their work that weld metal manganese content varied from 1 to 12 wt% and had almost no effect on the deposit ferrite number.

(iii) The third flaw was that the DeLong diagram over estimated the ferrite number (FN) of highly alloyed metals such as alloy 309 (Bermejo 2012).

In 1992 the WRC prediction diagram published by Kontecki and Siewert (1992) further modified the 1998 diagram which addressed the problems associated with the Schaeffler and DeLong diagrams. As mentioned earlier, this diagram replaced the DeLong diagram in the AMSE codes published in 1995. The authors completely removed the manganese coefficient from the nickel equivalent equation and eliminated the systematic ferrite number overestimation for highly alloyed weld metal and the WRC-1992 diagram, shown in figure 24, now covers a much broader range of compositions than the Delong diagram. The WRC-1992 diagram however, has a narrower composition range than the Schaeffler diagram because it extends only over the composition range of commercial alloys with which it was developed. The contribution of copper was included in the nickel equivalent as a coefficient of 0.25 multiplied by the copper content of the alloy, due to the development of duplex stainless steels containing significant amount of copper in recent years (Kontecki & Siewert, 1992).

Work by Lippold and Savage (1982) shows that the solidification mode of austenitic stainless steels is more accurate than the FN for predicting resistance to solidification cracking. This is because during solidification as primary delta ferrite, more phosphorus and sulphur are absorbed into the delta ferrite before it transforms to austenite resulting in greater dispersion of these harmful elements in the microstructure. For this reason, solidification mode boundaries, depicted as broken lines in figure 24, were included in the WRC-1992 diagram. These lines enable the user to predict the primary solidification mode of austenitic welds. The A and AF phase fields on the diagram denote primary austenite solidification. Alloys in these areas will potentially be susceptible to solidification cracking. Alloys situated in the F and FA phase fields solidify as primary delta ferrite and will be resistant to hot cracking. The phase fields in figure 24 are explained in detail as follows:

- Area A denotes primary solidification as austenite with no further transformation down to room temperature (high Ni_{eq}).
- Area AF denotes primary solidification as austenite with subsequent partial transformation to ferrite on cooling (slightly high Ni_{eq}).
- Area FA denotes primary solidification as ferrite with subsequent partial transformation to austenite (slightly high Cr_{eq}) representing the favoured solidification mode.
- Area F denotes primary solidification as ferrite with no further transformation (high Cr_{eq}).

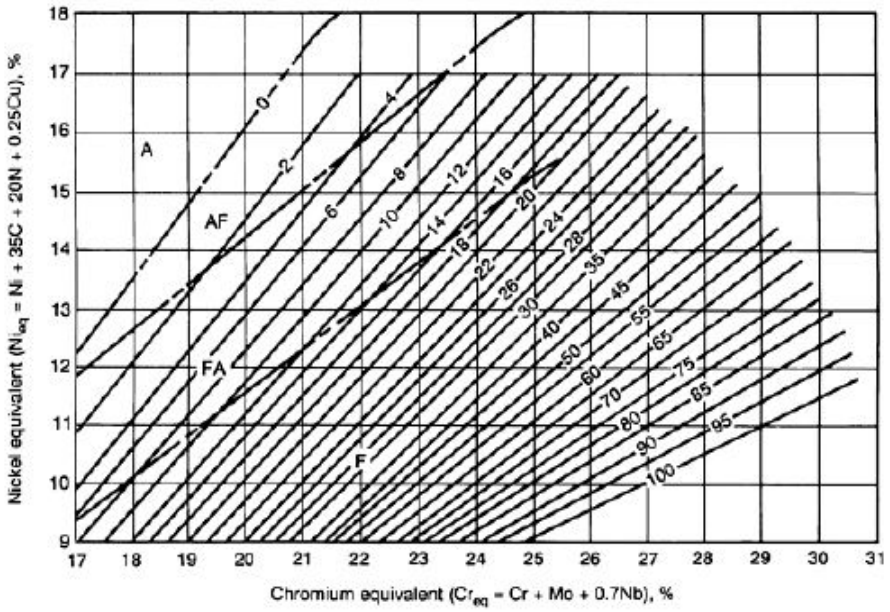

Figure 24: WRC-1992 constitution diagram (Kontecki and Siewert, 1992)

2.12 Control of Ferrite Content/Ferrite Number

2.12.1 Heat Input

Heat input to the base metal or underlying weld beads must be restricted when conditions can induce corrosion due to sensitization or embrittlement due to sigma formation. In this respect, the submerged arc welding and pulsed spray MIG welding processes have disadvantages because of the high heat input of these processes. These high heat input welding processes require the use of filler wires with higher a ferritic tendency than moderate energy processes to prevent hot cracking during solidification (Castro & de Cadanet, 1975). A case study looking into weld cracking in a 72 inch stainless steel duct using SMAW and SAW conducted by Wilks (2002) supported this higher ferritic tendency filler wire requirement for the high heat input processes. He showed that virtually all circumferential and longitudinal welds done with SAW contained significant cracks while the welds done with SMAW contained no cracks. The cracks evaluated generally propagated down the centerline of the weld, but fracture deviated along the details of the weld solidification structures. These solidification structures contained impurity concentrations along the grain boundaries as

this region was the last to solidify. The higher ferrite tendency filler wires would therefore reduce solidification cracking susceptibility by retaining delta ferrite. As discussed earlier, this retained delta ferrite however does increase the risk of forming the detrimental sigma phase when in high temperature service. The study concluded that the SMAW welds did not have these distinct solidification boundaries, because the size of the weld beads were smaller and therefore cooled faster in comparison to the SAW weld beads (Wilks 2002). SMAW therefore limits the ferrite formation more effectively than the SAW and MIG welding processes. SAW and MIG welding processes are used during fabrication because the high heat inputs give faster production while SMAW is used for field repairs due to its mobility.

2.12 .2 Cooling Rate

The effect of heat input is similar to that of pre-heat temperature; as a result as either the heat input or the preheat temperature increases, the rate of cooling decreases for a given base metal thickness (Funderburk, 2000). The following proportionality function shows this relationship between preheat temperature, heat input and cooling rate:

Equation 4: Proportionality function (Funderburk 2000)

$$R \propto \frac{1}{T_o H} \qquad (4)$$

Where: R is the cooling rate (°C/ sec),
T_o is the preheat temperature (°C)
H is the heat input (kJ/mm)

According to Castro and de Cadanet (1975) the amount of ferrite nucleated, and its distribution in the microstructure of the weld deposit depend on the cooling rate. Work by Padilha, Tavares & Martorano (2013), showed that the chemical composition of the steel affects formation and distribution of delta ferrite more than the cooling rate. Castro *et al.* (1975) also found that the ferrite particles were finer as the cooling rate increased due to lower heat input. According to Padilha *et al.* (2013), the influence of cooling rate on delta ferrite formation was weak, although a slight decrease in delta ferrite fraction with increasing cooling rate could be observed in their work. Castro *et al. (*1975)

furthermore showed that when welding with the SMAW process, the cooling rate does not vary over a sufficiently wide range to affect the ferrite content of the deposit to any great extent. Work by Rao and Prasannukumar (1984) also show that ferrite structure differs with ferrite content; for low ferrite contents the structure was a discontinuous and vermicular and for higher ferrite contents a continuous vermicular ferrite network was seen.

2.12.3 Welding Process

2.12.3.1 Shielded metal arc welding (SMAW) process

This welding process is the least efficient welding process in converting electrical energy to useful heat and therefore makes it easier to control the ferrite content of the weld metal within a limited range. The current to be used is determined by the wire diameter so the cooling rate does not vary greatly between the different wire diameters.

2.12.3.2 Gas Tungsten Arc Welding (GTAW/TIG)

When using the GTAW process it becomes more difficult to control ferrite numbers because when welding under argon gas the composition of the weld deposit is almost identical to the filler metal. This obliges the steel manufacturer to fabricate stainless steel wires with more restricted compositional ranges than those usually achieved for the fabrication of plates or forgings (Castro & de Cadanet, 1975).

Work by Lundin *et al.* (1980) showed that the nitrogen addition, which can be in the shielding gas when welding with GTAW, was an effective way of reducing and/or controlling ferrite content. Further, that the nitrogen addition had relatively very little effects on fissuring tendency in material, 304 and 304LN plate, evaluated. This research work showed it was possible to reduce the ferrite content from 5FN to 0.5FN and maintain fissuring resistance by adding nitrogen to the shielding gas (Lundin *et al.* 1980).

2.12.3.3 Submerged Arc (SAW) and Metal Inert Gas (MIG) Welding:

Keeping the ferrite content low with these welding techniques is very difficult because these high energy processes, like spray transfer MIG and especially Submerged Arc Welding, generally require the use of filler wires having higher ferrite tendency than moderate energy processes to prevent solidification cracking. This in turn results in greater ferrite content in the weld metal (Castro & de Cadanet, 1975).

2.12.4 Welding Consumable Considerations

When welding on intermediate ferrite forming base material as in the case of AISI 304H stainless steel, it is recommended that only filler metals having relatively low ferrite content be used for welding. It is relatively easy to control the ferrite content of the weld metal within a limited range when welding with a covered electrode as in the case with SMAW. This is because the electrode manufacturer can precisely adjust the composition of the covering with respect to that of the core wire. Special electrodes of this type meant to produce either low or high ferrite content weldments are called 'controlled' ferrite consumables are and commercially available (Castro & de Cadanet, 1975).

2.13 Sensitization of austenitic stainless steel

2.13.1 Sensitization Theory

According to Lee (1985), three predominant sensitization theories exist. These three theories are namely; the chromium depletion theory, noble carbide theory and the segregation theory. Sensitization according to the chromium depletion theory attributes sensitization to the precipitation carbides in regions adjacent to the grain boundaries to levels below what is required for passivation (Lee 1985). Figure 25 shows the grain boundary structure of sensitized steel due to chromium depletion. Figure 25 also shows how chromium carbides precipitate on the grain boundaries leaving the chromium depleted zone adjacent to the grain boundary. Bruemmer and Was (1994) in their work further state that the depletion of chromium is controlled by the thermodynamics of

carbide formation and differences between the diffusivities of chromium and carbon and that carbide formation occurs in a temperature range where carbides are thermodynamically stable and chromium diffusion is sufficiently rapid for carbide nucleation and growth in a finite time frame. A method of illustrating precipitation behavior is by the use of a time-temperature precipitation (TTP) diagram which is shown in Figure 26. The TTP diagram shows that carbide nucleation and growth occurs first in the chromium rich delta ferrite and on the delta ferrite-austenite boundary, followed by precipitation at high angle grain boundaries, incoherent twin boundaries and finally, at coherent twins. The diagram shown in Figure 26 specifically for 304 type austenitic stainless steel but trends time-temperature precipitation diagrams are also available for 316 SS, duplex alloys and high-chromium stainless steels. It is important to note that delta ferrite will not be present in all alloys, but is possible in many austenitic stainless steels depending on bulk composition and processing treatment. Carbon is an extremely effective austenite stabilizer, and its content is a critical factor in determining whether ferrite will remain in 304 type stainless steel. The effect of carbon content on the isothermal precipitation of $M_{23}C_6$ chromium carbides in 304 type austenitic stainless steels is shown in the time-temperature sensitization (TTS) curves in figure 27. Figure 27 shows that as carbon content decreases, the time required for sensitization increases while as temperature required for sensitization decreases.

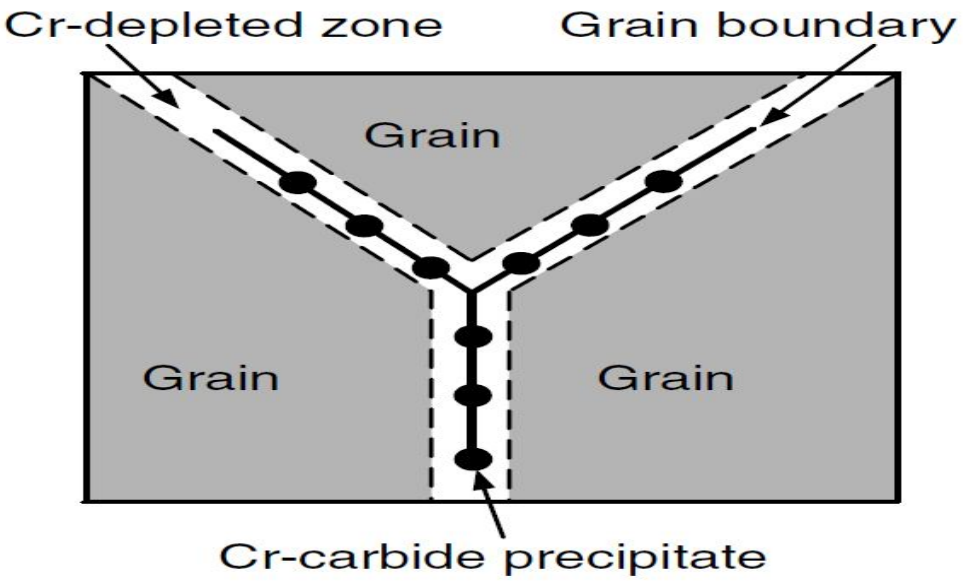

Figure 25: Grain boundary structure of sensitized steel (Kou 2003)

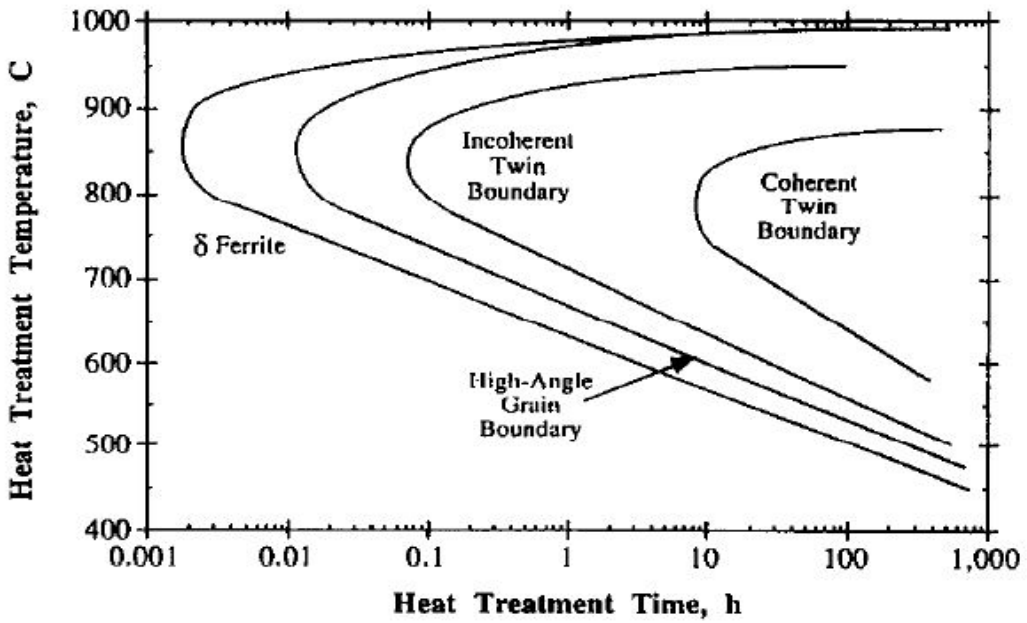

Figure 26: Time-temperature-precipitation (TTP) for 304 type stainless steel (Stickler & Vincier, 1961)

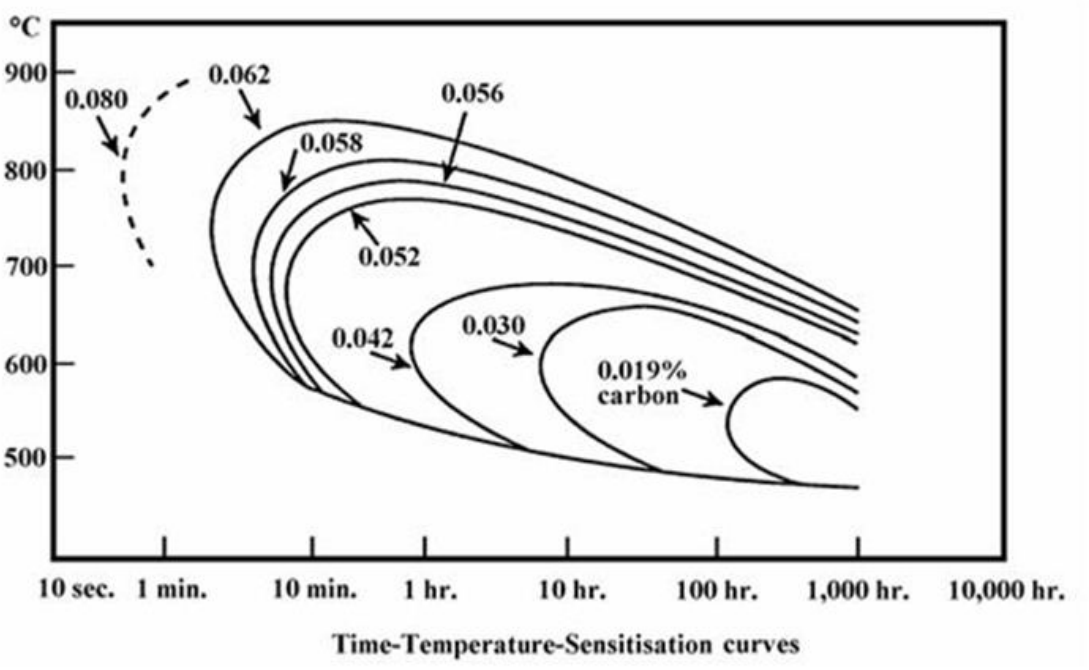

Figure 27: Time-temperature-sensitization (TTS) carbide precipitation curves for type 304 stainless steel (Nickel Institute, 1992).

2.13.2 Low Temperature HAZ Sensitization (LTS) behaviour

Low temperature sensitization occurs in the localized heat affected zone (HAZ) adjacent to the weld upon welding austenitic stainless steel (Povich 1978). Tedmon *et al.* (1971) noted that the "local" equilibrium concentration of chromium in the precipitated chromium carbide decreases considerably as sensitization temperature decreases. It is important to note that Tedmon (1971) was first to separate the "nucleation" and "diffusion" reactions of chromium depletion. Schmidt *et al*. (1983) quantified the compositions of the chromium carbide particle formed during low temperature sensitization (LTS) at temperatures below 500°C to contain 28 wt% chromium, compared to carbides formed at higher temperatures, 600-800°C, which contain 70-95 wt% chromium. Low temperature sensitization-enhanced susceptibility to corrosion still existed, even in the case where the chromium content of the carbide was only 28 wt% because other mechanisms such as low temperature solute segregation may contribute to the increased susceptibility toward corrosion (Schmidt et al., 1983).

Work by Andresen, Solomon and Taylor (1981) showed that slow cooling rates required to produce sensitization in 304L and 316L are not normally encountered during conventional welding practices. The American Petroleum Institute (API) recommended practice 852 (2009), which gives welding guidelines for chemical, oil and gas industries recommends a maximum welding inter-pass temperature of 175°C to prevent low temperature sensitization during welding for welding austenitic stainless steels. Tedmon's (1971) work which separated the nucleation and diffusion reactions of carbide precipitation and growth showed that carbides may be nucleated by "brief" exposure to temperatures in the normal sensitization range, as experienced during welding, without a detrimental degree of chromium depletion. Povich (1978) conducted quantitative TEM studies on a welded section that underwent a low temperature heat treatment directly after welding. The quantitative TEM studies concluded that no "new" carbides nucleated during low temperature heat treating carbides and that the carbides nucleated during welding increased in size after the heat treatment. The relevance of LTS to industrial processes may be described as follows: When type 304 stainless steel components are welded together, carbides are nucleated in the HAZ but produce very limited

sensitization. However, after many years at process operating temperatures, the degree of sensitization may progress via LTS to enhance the possibility that intergranular stress corrosion cracking would occur (Povich 1978).

2.14 Etching of austenitic stainless steels

Metallographic etching is a technique used to highlight different metallurgical features of metals at microscopic levels. Some of the features highlighted include grain boundaries, phase differences and non-metallic inclusions (Petzow 1978). By studying the character, quantity and distribution of these different metallurgical features, metallurgists are capable of predicting and explaining physical properties and performance failures of a given metal sample. An optical microscope with a magnification ranging between 50X to 1000X is required to evaluate the metallurgical features of most metals. To evaluate these metallurgical features, a metallic sample must be polished to a very fine mirror-like finish and then etched in a chemical solution to create contrast needed between the different phases and features of the metals microstructure. The chemical solutions used are known as etchants and are used to selectively corrode some of the features. The etched metallurgical features show up as darker regions. This is possible because differences in the composition, structure or phase of a metal will create electrochemical potentials that alter the relative rates of corrosion when exposed to an etchant. Metal etching can be either electrolytic or chemical.

2.14.1 Electrolytic etching

According to Petzow (1978), electrolytic etching which is also known as anodic etching applies electrical potential to the specimen using an external electrical circuit. Figure 28 shows a typical setup consisting of the specimen, which is the anode and its counter-electrode, the cathode, immersed in an electrolyte. The electrolyte is the etchant that is to be used. The voltage is regulated with a voltmeter. During electrolytic etching, the specimen is submerged face-up in the electrolyte. The stainless steel cathode is the placed in the electrolyte while the anode is placed on the surface of the specimen.

When the current is applied, the positive metal ions leave the specimen surface and diffuse into the electrolyte; an equivalent number of electrons remain in the material.

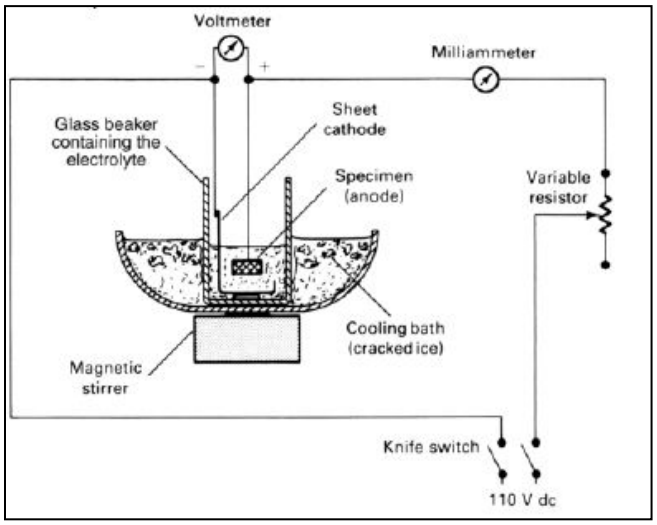

Figure 28: Basic laboratory setup for electrolytic etching and polishing (Petzow 1978)

This results in direct etching, shown as segment A—B of the current density versus voltage curve in Fig 29. In segment A-B of figure 27, the specimen is dissolved without the formation of a precipitated layer. Segment B-E of figure 27 shows the region of the curve where an insoluble layer is precipitated on the surface of the anode, also known as indirect etching. In segment B-E, metal ions leaving the material react with nonmetal ions from the electrolyte and form an insoluble compound; the precipitated layers will then form on the specimen surface (Petzow 1978). Direct or electrolytic etching therefore involves the process of electrolysis, which is also the basis for electro-polishing.

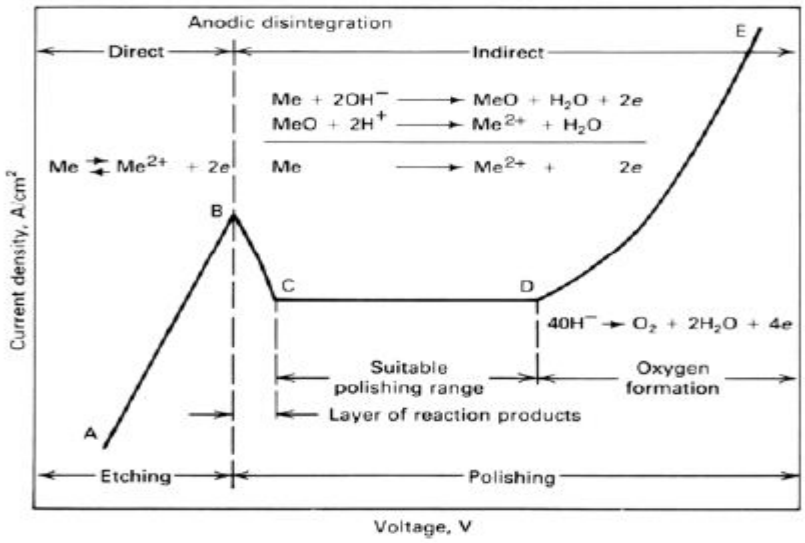

Figure 29: Idealized current density versus applied voltage for many common electrolytes with regions for electrolytic etching and polishing as indicated (Petzow 1978)

Electrolytic etching using strong basic solutions produces coloured films and is widely used with stainless steels to color delta ferrite or sigma phase. Electrolytic reagents, which are often used in the etching of austenitic and duplex grades, provide great control of the etching process and are highly reproducible (Bramfitt & Benscoter, 2002). These electrolytic etching reagents are generally quite simple in composition. The metallurgical feature selectivity of various hydroxide electrolytic etching reagents has been shown in table 9. Strong hydroxide etching solutions attack sigma phase preferentially to carbides and weak hydroxide solutions attack carbides much more readily than sigma phase. Therefore, to reveal sigma phase, 10 *N* KOH or 20% NaOH is employed, and to reveal carbides, concentrated ammonium hydroxide, NH4OH, is used. Table 8 below shows some etchants that can be used for electrolytic etching of stainless steel to reveal delta ferrite and sigma phase. Research conducted by Van der Voort (2011), austenitic stainless steel underwent electrolytic etching in 20% NaOH, caustic, at 3 Volts dc for 10 seconds. The delta ferrite was colored tan and blue while the sigma phase was colored orange-brown with carbides visible, but not clearly etched (Van der Voort 2011).

Table 9: Electrolytic etchants for etching sigma phase, carbides and delta ferrite (Bramfitt & Benscoter,2002)

Etching Reagent	**Comments**
50g NaOH and 100ml H_2O	Electrolytic etch at 2-6 V dc, 5-10 s to reveal sigma phase in austenitic grades
56g KOH and 100ml H_2O	Electrolytic etch at 1.5-3 V dc for 3 s to reveal sigma phase (red-brown) and ferrite (Bluish). Chi colored same as sigma.
20g NaOH and 100ml H_2O	Electrolytic etch at 20 V for 5-20 s to outline and color delta ferrite tan
10ml HCl and 90ml methanol	Electrolytic etch at 1.5 V dc, 20°C to attack sigma phase. Use at 6 V dc for 3-5 s to reveal structure.
10g oxalic acid and 100ml H_20	Popular electrolytic etch, 6 V dc, 25-mm spacing. 15-30 s reveals carbides, grain boundaries revealed after 45-60 s; sigma phase outlines after 6 s. Lower voltage (1-3 V dc) can be used. Dissolves carbides. Sigma strongly attacked. Austenite note attacked. Good for revealing carbides. Use with care under a hood.

2.14.2 Chemical etching

Unlike electrolytic etching, normal etching does not require external current because the etching solutions contain an oxidizing agent, such as nitric acid or hydrogen peroxide, that takes the place of the electric current used in electrolytic etching. The elaborate equipment used in electrolytic etching is therefore not required for chemical etching. Uniform dissolution of the surface of a particular metal in a specific solution is due to the presence of either a passivating oxide film or a viscous diffusion layer. The rates of metal removal are high enough to remove scratches and deformation from fine grinding. Chemical etching is a very versatile technique and can be applied to etching of round, curved surfaces and for simultaneous etching of all of the sides of a square, rectangular, or flat specimen. One major disadvantage is that a given volume of solution can only polish a limited number of specimens as some solutions must be mixed fresh and must be discarded immediately after use; they therefore cannot be stored as stock solutions. Another disadvantage is that many of the etching solutions are dangerous to

use with most having to be used under a chemical hood, to avoid contact with the solution or its vapors. The sample can be held with tongs and submerged in the etching solution for the etching operation. Some chemical etchants work better by swabbing and with these chemical etchants; the solution is placed in a shallow, wide dish and the solution is rubbed against the surface of the specimen using cotton that has dipped in the etchant. With some specimen, the solution volume relative to the sample size is important. Therefore, for best results, attention must be given to the technique. Most specimens are ground to 600-grit SiC, although in a few instances, a coarser final grind works best. In general, the finer the mechanical finish, the less time is required for chemical polishing, and difficulties with pitting and other preferential attack are reduced. A film sometimes forms on the specimen surface, which must be removed by treatment with an appropriate solution. Table 10 lists some etchants that commonly used for the chemical etching austenitic stainless steel.

Table 10: Chemical etchants for etching sigma phase, carbides and delta ferrite (Bramfitt & Benscoter, 2002)

Etching Reagent	**Comments**
3 parts HCl, 2 parts glycerol, 1 part HNO_3	Glyceregia. Popular etch for all stainless steel grades. Use fresh; never store. Discard when reagent is orange colored. Use with care under a hood. Add HNO_3 last. Swab a few seconds to a few minutes. Attacks sigma phase, outlines carbides. Substitution of water for glycerol increases attack rate.
15ml HCl, 5ml HNO_3 , 100ml H_2O	Dilute aqua regia for austenitic grades. Uniform etching of austenite; outlines carbides, sigma phase, and ferrite (sometimes attacked)
4g $KMNO_4$ (potassium permanganate), 4g NaOH and 100ml H_2O	Groesbeck's reagent. Use at 60-90°C to min. Colors carbides dark, sigma phase gray, ferrite and austenite not affected.
1g picric acid, 5ml HCl, 100ml ethanol	Villela's reagent. Use at room temperature to 1 min. Outlines second-phase particles (carbides, sigma phase, and delta ferrite); etches martensite. Can be stored.

III. CHAPTER THREE - EXPERIMENTAL PROCEDURE

In this study on the effect of inter-pass temperature on the ferrite number of welded joints, the samples were welded using the shielded metal arc welding process. The ferrite number of the weld metal was determined with a ferritescope on the as-welded samples. Specimens were extracted, ground, polished and etched for evaluation of their metallurgical features under an optical microscope.

3.1 Materials Used:

Base metal material: In this study of the effect of welding inter-pass temperature on the weld metal ferrite number, 304H type austenitic stainless steel was used as the base metal to be welded. The pipe samples were 100 mm long with a wall thickness of 7.62 mm. The samples were cut longitudinally with a single-V joint preparation where the sample was cut longitudinally. The stainless steel used was 304H off-cuts from a previous repair done by Avenger-LTA at the SAPREF Refinery. The samples were welded by an Avenger-LTA welder, qualified to weld 304H stainless steel, in their fabrication workshop located at the SAPREF Refinery in Durban. The chemical composition of test material is presented in table 11 were determined using the Spectrotest TXC25 manufactured by Spectro. The minimum required carbon content 0.04 wt% was achieved. It is important to note that the carbon content of 0.04% narrowly meets the carbon requirement for a type 304H stainless steel. Figure 30 graphically shows the specified carbon content limits and the overlaps of the three separate grades, type 304, 304L and 304H.

This essentially means that the stainless steel used in this project was a dual certified and can be categorized as both type 304 and type 304H austenitic stainless steel.

Table 11: Chemical composition of the 304H austenitic stainless steel samples

Grade	UNS Number	Carbon (wt%)	Chromium (wt%)	Nickel (wt%)	Molybdenum (wt%)	Nitrogen (wt%)
Composition of Spec	S30409	0.04 - 0.1	18.0 - 20.0	8.0 – 10.5	-	-
304H	S30409	0.04	17.1	8.18	0.57	-

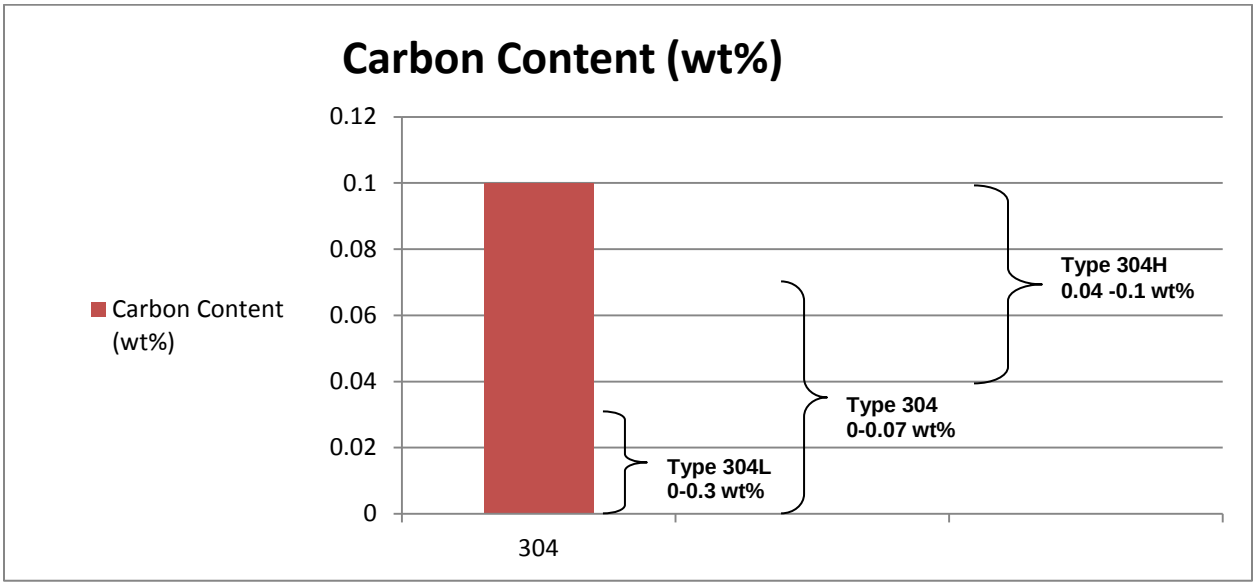

Figure 30: Carbon compositional limits of ASTM A240/240M Type 304, 304L and 304H austenitic stainless steel

Welding consumable: The 308H covered electrode was the welding consumable used to weld 304H stainless steel samples. The 308H electrodes was manufactured by Avesta Welding and supplied by Bohler Uddeholm Southern Africa. The batch of welding electrodes used had the chemical composition shown in table 12. The electrode diameter was 2.5 mm and the length of the electrode was 300 mm. The welding current recommended by the manufacturer for the 308H electrode was between 50-80 volts direct current electrode positive (DCEP).

Table 12: Chemical composition of the 308H welding electrode (Avesta 308H welding consumable certificate, 2014)

Welding Consumable	Carbon (wt%)	Chromium (wt%)	Nickel (wt%)	Molybdenum (wt%)	Nitrogen (wt%)	Copper (wt%)	WRC-1992
308H	0.072	20.1	10.5	0.01	0.049	0.02	3

3.2 Equipment Used:

Ferritescope: The MP 30 ferritescope calibrated to AWS A4.2 manufactured by Fischer in Germany was used to measure the ferrite numbers of the 100 mm welded samples. Raysonics (Pty) Ltd conducted the ferritescope measurements.

Grinding and polishing machines: Manual grinding and polishing machines in the metallogrpahy laboratory at the Witwatersrand University were used to grind and polish the samples.

Metallographic compression mounting press: The Struers CitoPress-1 automatic compression mounting press was used to mount the specimens extracted from the samples.

Electrolytic etching machine: The electrolytic etching equipment used in this research was built by the University of the Witwatersrand.

Grinding and polishing consumables: Polishing pads, silicon carbide grit paper, cotton swabs, abrasive cutting disks, phenolic resin commonly known as Bakelite powder,

Light microscope: To evaluate the microstructures and metallurgical features of the welded samples the Lecia DM6000M digital microscope was used.

Infrared thermometer: The Top Tronic, T306 model, infrared thermometer was used to measure and control the inter-pass temperature. The T306 model can be used from the minimum temperature -50°C up to the maximum temperature of 700°C.

Chemical analysis: To do the chemical analysis of the 304H base metal and weld metal stationary metal analyzers at the SAPREF refinery central stores was used. This metal analyzer used was the Spectrotest TXC25 manufactured by Spectro. Analysis for the nitrogen content was done by Scrooby's laboratory services using the combustion method.

3.3 Procedure:

3.3.1 Joint preparation and welding

Single-V longitudinal joints were prepared for welding on one side of the four 100 mm long samples with the shielded metal arc welding (SMAW) process. The joints had a bevel angle of between 50-60°C, a root face of 2 mm and a root gap of 3 mm. The four samples were marked as A, B, C and D and each of the weld joints were welded at a different inter-pass temperature between 100 – 200°C. In order to remove the moisture from the 308H electrodes, they were placed in an oven heated to 250°C for 30 minutes

prior to the welding of the samples. The electrodes that were not in use were kept in the oven during the welding operation. Table 13 represents welding variables for each of the welds which include the inter-pass temperature ranges and welding amperages and voltage used for the welding of samples A, B, C and D. The electrode manufacturer's maximum recommended Amperage was 80 Amps. This could be achieved with samples A and B which were welded at inter-pass temperatures of 105-110°C and 135-140°C respectively. Keeping within the manufacturers amperage limits while trying to maintain an inter-pass temperature of 165-170°C and 195-200°C was difficult to do when welding samples C and D. This was because the heat loss was so high in austenitic stainless steel resulting in rapid cooling of the weld bead and base metal leaving insufficient time to adequately clean the weld bead by removing the slag layer before welding on the next pass. The decision was then made to increase the heat input slightly when welding sample 3 by increasing the amperage from 80 to 82 to achieve the required165-170°C inter-pass temperature. When welding sample 4 the amperage was further increased from 82 to 103 Amps to allow sufficient heat input for proper removal of the slag before applying the next pass at the required inter-pass temperature of 195-200°C. The voltage remained in the recommended range of 20-30 V. The weld direction and bead sequenced was kept the same for all the samples.

Figure 31 shows the welded pipes with after sections were cut out for mounting.

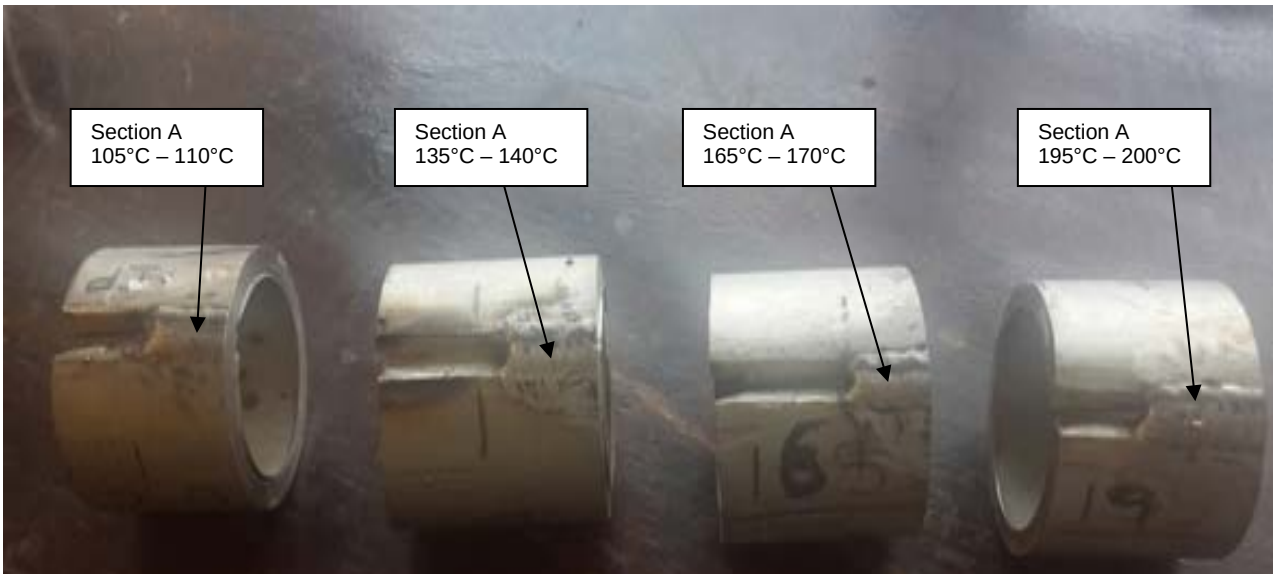

Figure 31: Welded pipe samples after sections were cut out

The inter-pass temperature was measured with an infrared thermometer. The measurement location was on the base metal, 2.5 mm from the weld toe for all the welding passes at reference point A as shown in Figure 32. Reference point A was located 25 mm from the weld toe where welding of the bead started.

Table 13: Welding variables used for welding the pipe samples

	Inter-pass Temperature	Root Run (Amps)	1st Pass (Amps)	2nd Pass (Amps)	3rd Pass (Amps)	Cap (Amps)	Voltage DCEP
Sample 1	105 - 110°C	40	80	80	80	80	20-30V
Sample 2	135 - 140°C	40	80	80	80	80	20-30V
Sample 3	165 - 170°C	40	81	82	82	82	20-30V
Sample 4	195 - 200°C	40	82	103	103	103	20-30V

3.3.2 Ferrite measurement

After the welding of the four pipe sections was completed, the weld bead was cleaned using a stainless steel wire brush and a ferrite number measurement using the Fischer MP30 ferritescope. All the readings were taken in the centre line of the as-weld bead along the full length of the 100 mm weld bead of the samples as shown at location B of the schematic in Figure 32. The ferritescope was chosen to measure the ferrite content in addition to FN numbers determined using the WRC 1992 constitution diagram because it was believed to be an accurate method. Other ferrite measurement methods include metallographic evaluation and x-ray diffraction. The metallographic evaluation method is done by point counting with the aid of a microscope, this is however not accurate due to inhomogeniety that exists in the weld metal microstructure and the evaluation will therefore not be representative for the entire welded sample. The the x-ray diffraction method is also not as accurate as the ferritescope because the diffraction patterns from x-ray diffraction tend to diffuse in nature and furthermore they are subject to interpretation which makes this method subjective. Consistent accuracy is therefore a challenge using the metallographic evaluation and the x-ray diffraction techniques. In order to minimize the error due to weld metal inhomogeneity, the average of 45 ferrite measurements was taken along the full length of the weld bead using the ferritescope

for each welded sample. The 45 measurement readings were from measurement sets 1-15 with each measurement set consisting of 3 readings.

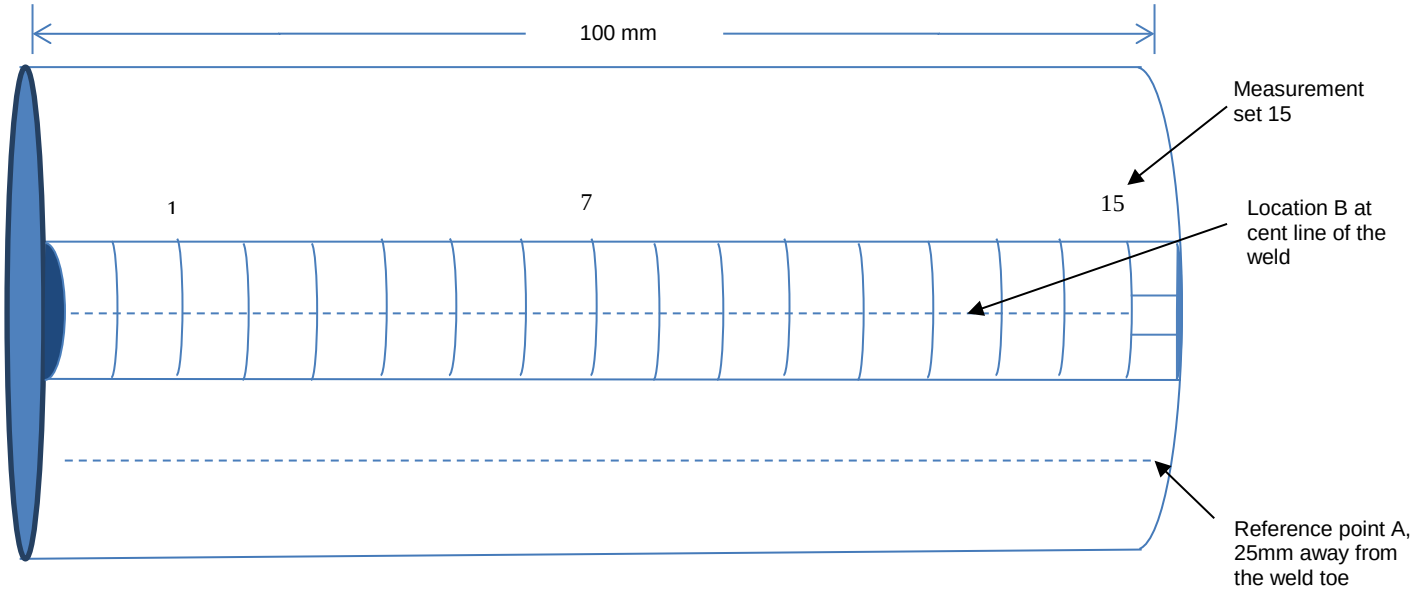

Figure 32: Top view of the weld bead on the welded samples with the centre line of weld bead marked as location A

3.3.3 Specimen extraction and sectioning

For sample preparation in order to do microscopic analysis; specimens of the welded joints were extracted (cut out) from each of the four 100 mm length 3" pipe welded samples to sizes appropriate to facilitate easy handling using a band saw. After the specimens were extracted, they were clamped in a vise and cross-sectioned in a metallographic abrasive cutter to an appropriate size to enable hot mounting. The metallographic sample cutter used, utilized a wear resistant silicon carbide disk as its blade. Lubricating fluid was continuously supplied as a coolant during cutting or sectioning to prevent burn damage on the surface of the specimen and to reduce the wear rate of the cutting disk. A gradual force was applied on the cutter during the sectioning of the weld joint specimen to prevent fracture of the disk and burn damage, and excessive blade wear. After extraction and sectioning was complete, the appropriately sized specimens, shown in Figure 33, were rinsed under running water to remove all cutting residue from their surface.

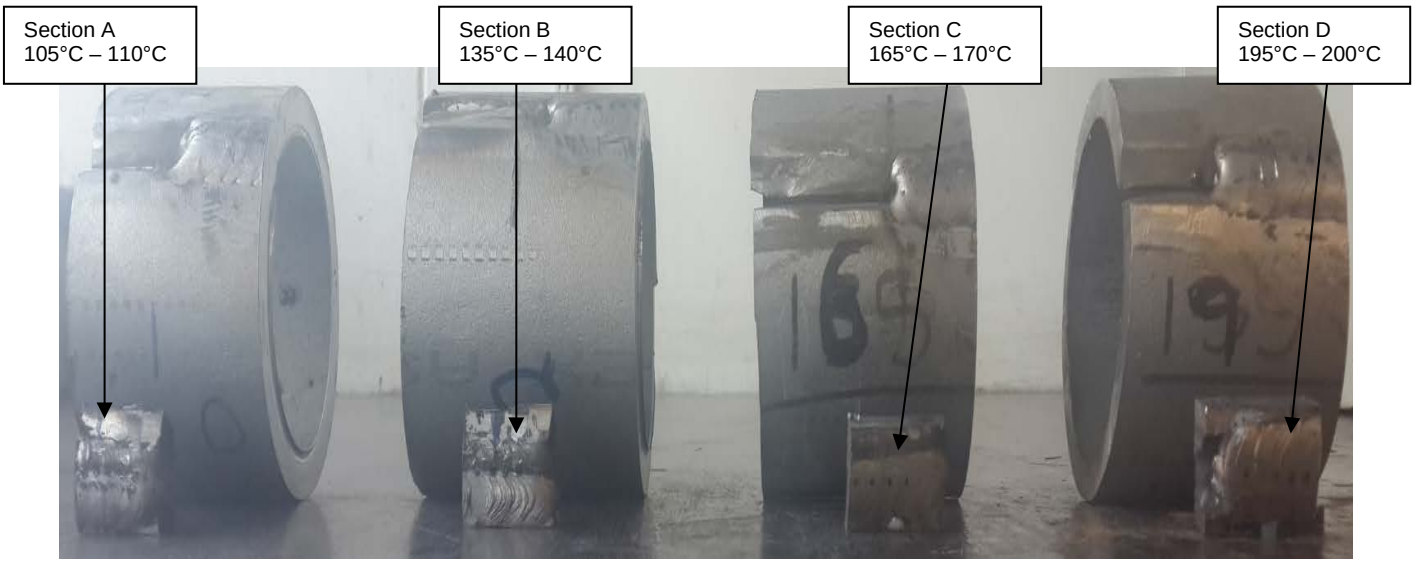

Figure 33: Welded pipe samples with sections that were cut out for mounting and sample preparation

3.3.4 Specimen mounting

Prior to starting the specimen mounting operation the mounting press mold assembly was cleaned with a cloth to remove all debris from previous mounting operations. One specimen was placed in the centre of the mounting assembly ram and the ram was thereafter lowered. Two scoops of the Bakelite resin was poured into the lowered mold. The mold assembly was locked tightly and the automatic mounting press was started.
The mounting time for the specimen was set for 10 minutes at a temperature of 200°C.
When mounting press indicated that mounting of the specimen was complete, the assembly cover was unlocked and the mounted specimen was removed from the press. The mounting press mould assembly was then cleaned and all residues from the mounting operation were removed. The process was repeated for the mounting of each specimen. The mounting made the specimens easier to handle during grinding, polishing and etching steps that followed. The mould that the specimens were in was 30mm in diameter which allowed sufficient space for the marking of the mounted specimens with a hand held engraver according to their inter-pass temperatures for identification. The specimens A, B, C and D were marked as 105-110°C, 135-140°C, 165-170° and 195-200°C respectively.

3.3.5 Specimen grinding and polishing

After mounting, all four specimens were prepared for electrolytic etching and microscopic analysis by course grinding, fine grinding and polishing. Course and fine grinding was done on silicon carbide grit papers of various sizes which were stuck on the rotating wheels of the grinding machines. The polishing was done using diamond and alumina oxide paste on the polishing machines. The grinding steps used continuous water injection onto the rotating grinding silicon carbide grit paper as a lubricant during grinding. The course grinding step was done using P240 sized silicon carbide grit paper for a maximum of three minutes. The samples were intermediately cleaned between the course and fine grinding steps by rinsing under running water and swabbing with cotton wool. Intermediate cleaning was done to ensure that all metal and grit residue was removed to prevent contamination of the grit paper that was to be used in the next grinding step. The next grinding step after coarse grinding was fine grinding and for this step P600 sized silicon carbide grit paper and the even finer P1200 sized silicon carbide grit paper was used. Fine grinding was done for a maximum of 4 minutes with both the P600 and P1200 grit paper with intermediate cleaning done with water and a cotton swab and drying with compressed air between the two fine grinding steps.
Table 14 shows the summary of the grinding and polishing steps used in preparation of the specimens for etching and microscopic analysis.

Table 14: Specimen preparation grinding and polishing steps and times

	Course Grinding (P240 SiC Grit)	Fine Grinding (P600 SiC Grit)	Fine Polishing (P1200 SiC Grit)	Rough Polishing (1um Diamond Paste)	Fine Polishing (Alumina Oxide)
Sample 1 (105-110 °C)	45 seconds	135 seconds	122seconds	163 seconds	180 seconds
Sample 2 (135-140°C)	40 seconds	115 seconds	130 seconds	163 seconds	180 seconds
Sample 3 (165-170°C)	45 seconds	129 seconds	127 seconds	163 seconds	180 seconds
Sample 4 (195-200°C)	47 seconds	125 seconds	130 seconds	163 seconds	180 seconds

After grinding was completed, the specimens were polished using soft polishing cloths with diamond paste and alumina oxide as polishing lubricants for rough and final polishing respectively. Rough polishing was done for a maximum of three minutes on the polishing machine utilizing a polishing cloth with 1 micron (um) diamond paste as the lubricant. The specimens were cleaned with a cotton swab dipped in ethanol for intermediate cleaning after the rough polishing step. As the last polishing step, final polishing was done for three minutes on a separate polishing machine which used a soft cloth and alumina oxide as the lubricating and polishing medium. After final polishing the specimens had a thin matte film on their surface which was removed by swabbing with cotton wool dipped in ethanol immediately after polishing to give a mirror surface finish. Samples A, B, C and D were placed in a vacuum desiccator after final polishing to protect the surface from any oxidation caused by the presence of moisture and dust.

3.3.6 Specimen etching

For the evaluation of the delta-ferrite and sigma phase that may have transformed from delta ferrite, the four specimens were placed in a glass beaker and submerged in sodium hydroxide solution commonly known as caustic, NaOH, one at a time for electrolytic etching. A caustic solution with a concentration 21% was used as the electrolyte to reveal the different metallurgical features e.g. delta ferrite, sigma phase, chromium carbides and grain boundaries in the stainless steel welded samples. The cathode and anode were connected to an external circuit. The stainless steel cathode wire was then placed inside the electrolyte and the anode wire was placed on the surface of the metal sample. The etching process was done for a maximum of 60 seconds at 66 volts. To reveal the primary solidification phase of the specimens were etched with Villela's reagent by swabbing for 1 minute at room temperature. In addition to Villela's reagent, the specimens were electrolytically etched using oxalic acid for 45 – 60 seconds at room temperature to evaluate the morphology of the primary solidification phase. To reveal the $M_{23}C_6$ chromium carbide phase that may have precipitated during welding of the four specimens, the four specimens were etched by immersion in

Groesbeck etchant at 60°C for 10 min. The etching with Villela's reagent and Groesbeck was done at Megchem (Pty) Ltd.
After every etching operation, the specimens were removed from the glass beaker using tongs and rinsed under running water. The specimens were then dried using a handheld electric hair dryer and stored in a desiccator for storage.

3.3.7 Microscopy

After drying the etched specimens, they underwent metallurgical evaluation under the light microscope. The specimens were each evaluated at X50, X100, X500 and X1000 magnification and photomicrographs of the microstructures observed at various magnifications were taken. The specimens were evaluated for their solidification phases, sigma phase and the presence of $M_{23}C_6$ chromium carbides that may have formed during welding and subsequent cooling of the specimens.

IV. CHAPTER FOUR - RESULTS

In this chapter, the results of the ferrite numbers measured with the ferritescope and theoretical ferrite numbers determined from the weld metal chemistry and WRC-1002 constitution diagram are presented. The microstructures of the following metallurgical features obtained are also presented: delta ferrite morphology, sensitization, sigma phase transformation in the heat affected zone of the base metal and the mushy zones of the weld metal.

4.1 Ferrite numbers

A total of 45 ferrite content measurements were taken by Raysonics (Pty) Ltd for each of the welded samples in order to reduce the effect of metallurgical inhomogeneity on the ferrite content measurement. In table 15, the average of three reading was recorded in each of the 15 measurements recorded for samples A to D. Figure 34a-d shows the graphical representation of the ferrite measurements of Samples A to D. Table 15 showed that sample A, welded at an inter-pass temperature range of 105-110°C, had a ferrite content which ranged between 1.9 – 3.1% with an average ferrite content of 2.3% which is equivalent to FN 2.3. Figure 34a shows a graphical trend of the ferrite measurements for sample A. Sample B which was welded at the inter-pass temperature of 135-140°C had a ferrite content which ranged between 3.1 – 4.6% with an average ferrite content of 3.8% which is equivalent to FN 3.8. Figure 34b shows the graphical trend of the ferrite measurements for sample B. Sample C which was welded at an inter-pass temperature of 165-175°C had ferrite content which ranged between 2.2 – 3.0% with an average ferrite content of 2.3% which is equivalent to FN 2.3. Figure 34c shows the graphical trend of the ferrite measurements for sample C. Sample D which was welded at 195-200°C inter-pass temperature had a ferrite content which ranged between 1.7 – 3.6% with an average ferrite content of 2.7% which is equivalent to FN 2.7. Figure 34d shows the graphical trends for this sample D. Figure 35 shows the

graphical comparison the ferrite average ferrite measurement values obtained for samples A, B, C and D.

Table 15: Ferritescope ferrite content measurement readings for sample A to D welded at various inter-pass temperatures

Measurement Location on pipe	**Specimen A** **105°C-110°C**	**Specimen B** **135°C-140°C**	**Specimen C** **155°C-170°C**	**Specimen D** **195°C-200°C**
1	2.5	3.7	2.2	2.4
2	3.1	4.6	2.6	2.9
3	2.6	4.5	2.6	3.1
4	2.4	4.1	2.6	3.1
5	1.9	4.0	3.0	2.9
6	2.3	3.8	2.7	3.2
7	2.3	3.5	2.7	3.6
8	1.9	3.1	2.3	2.6
9	2.5	3.7	2.7	2.6
10	2.2	3.5	2.5	2.1
11	2.1	4.1	2.3	1.7
12	2.4	4.0	2.9	2.4
13	2.4	4.0	2.4	2.5
14	2.5	3.5	2.8	2.9
15	2.4	3.0	2.4	2.0
Measurement Average	**2.3**	**3.8**	**2.3**	**2.7**

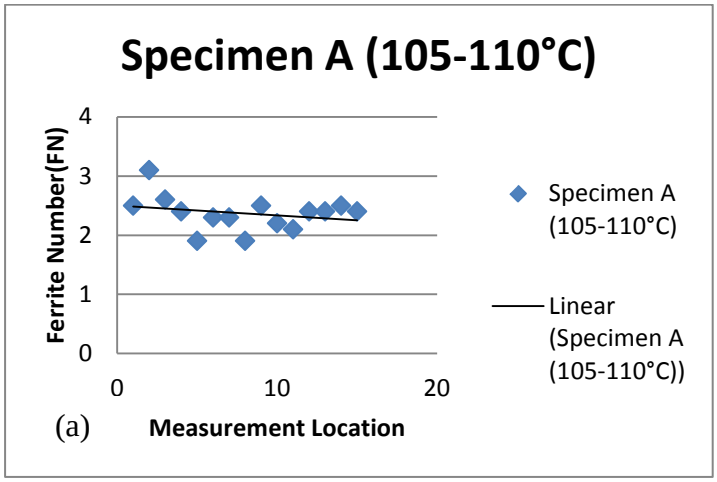

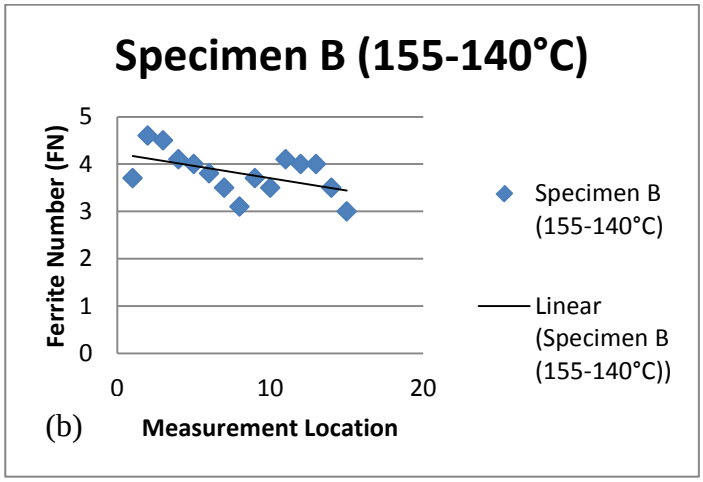

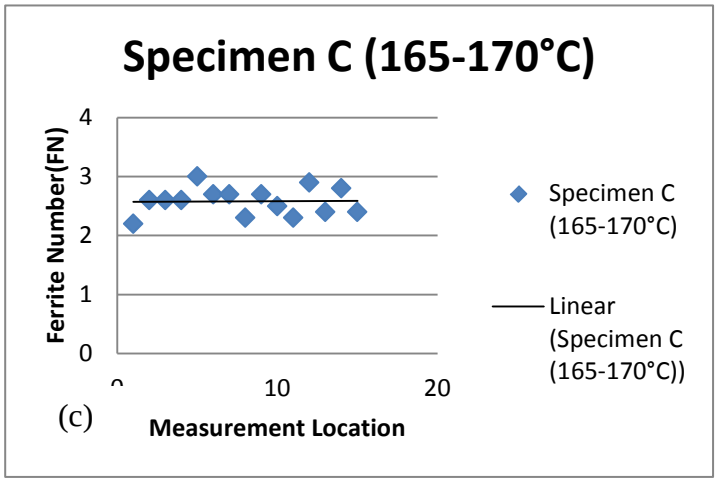

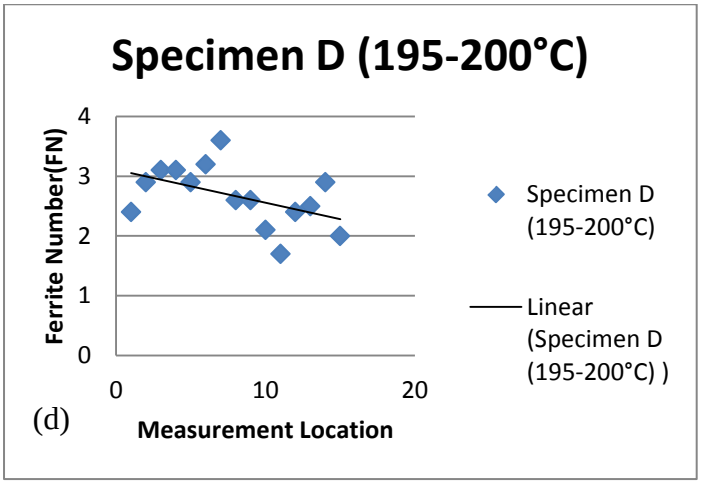

Figure 34a-d: Graphical representation of ferrite content measurement readings from table 10

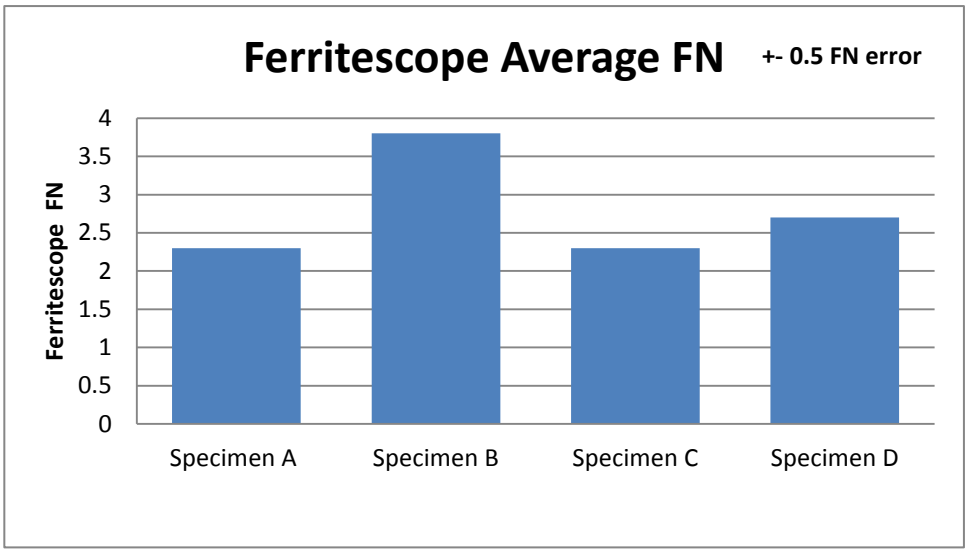

Figure 35: Graphical comparison of the average ferrite content measurement readings from table 14

The chemistry of the as-deposited weld metal for specimens A, B, C and D in table 16 was determined with a spectrometer with the combustion method used for the nitrogen content analysis.

Table 16: Chemical compositions of the weld metals of specimens A to D

Specimen	Inter-pass Temp (°C)	Carbon (wt %)	Chromium (wt %)	Nickel (wt %)	Molybdenum (wt %)	Niobium (wt %)	Copper (wt %)	Nitrogen (wt %)
A	105 - 110	0.042	18.5	9.89	0.12	0.015	0.059	0.115
B	135 - 140	0.044	18.5	9.82	0.12	0.014	0.053	0.0780
C	165 - 170	0.048	18.6	9.55	0.17	0.015	0.094	0.0782
D	195 - 200	0.047	18.7	9.47	0.18	0.013	0.096	0.0800

The Cr_{eq}/Ni_{eq} ratio of the weld metal and WRC-1992 ferrite numbers in table 17 was determined using the weld chemical composition in table 16. As seen in Figure 36 and 37, the Cr_{eq}/Ni_{eq} ratio and FN values showed an increase with an increase in inter-pass temperature respectively.

Table 17: The calculated chromium-nickel-equivalents and WRC-1992 ferrite numbers of the weld metals of specimens A to D

Specimen	$Cr_{equivalent}$	$Ni_{equivalent}$	Cr_{eq}/Ni_{eq} Ratio	WRC-1992 FN
A	18.63	13.67	1.36	1.0
B	18.62	12.93	1.44	2.0
C	18.78	12.81	1.46	2.5
D	18.88	12.73	1.48	3.0

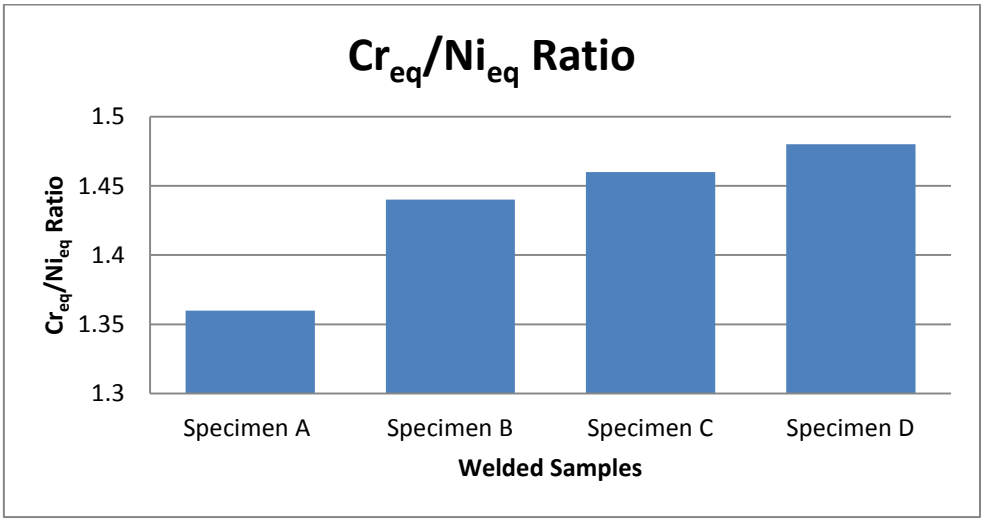

Figure 36: Graphical comparison of the Cr_{eq}/Ni_{eq} ratio from table 17

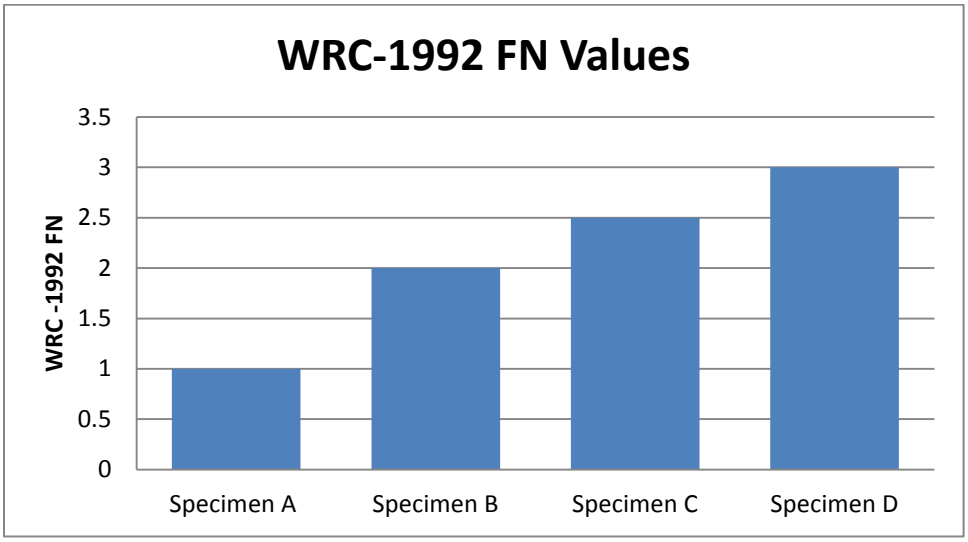

Figure 37: Graphical comparison of the WRC-1992 calculated ferrite numbers (FN) from table 17

The ferrite numbers were predicted by plotting the WRC-1992 constitution diagram in figure 38, using the chromium and nickel equivalents calculated from the weld chemistry.

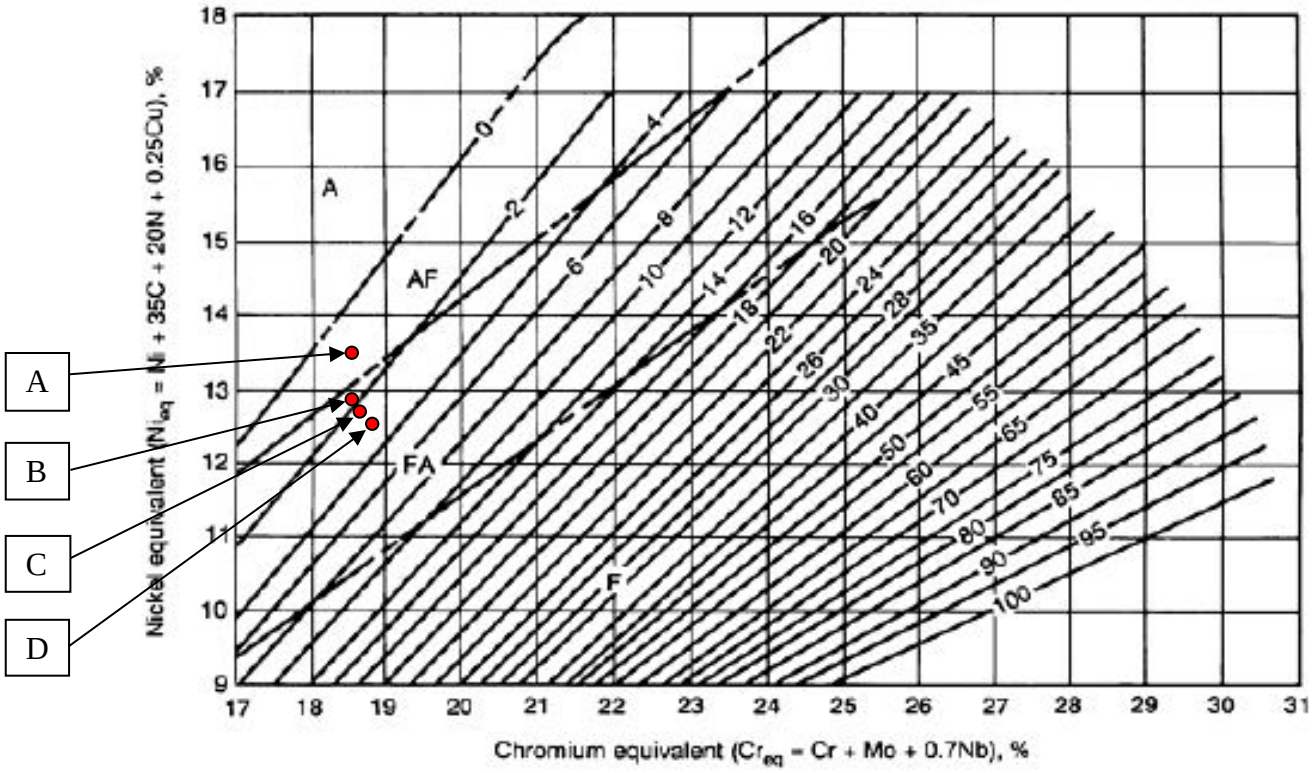

Figure 38: Ferrite numbers plotted on WRC-1992 calculated using the weld metal chemistry of specimens A, B, C and D

4.2 Metallurgical feature evaluation

The microstructures of the four specimens were determined with various etchants. The solidification phases and the secondary phases that resulted from transformation and precipitation during welding at the various inter-pass temperatures were evaluated. The phases of interest were austenite, delta ferrite, sigma phase and $M_{23}C_6$ chromium carbides.

4.2.1 Solidification phases

Specimens A, B, C and D welded at inter-pass temperatures of 105-110, 135-140, 165-170 and 195-200°C respectively were etched in Villela's reagent to determine the primary solidification phase. Figure 39a-d shows the photomicrographs at X200 magnification.

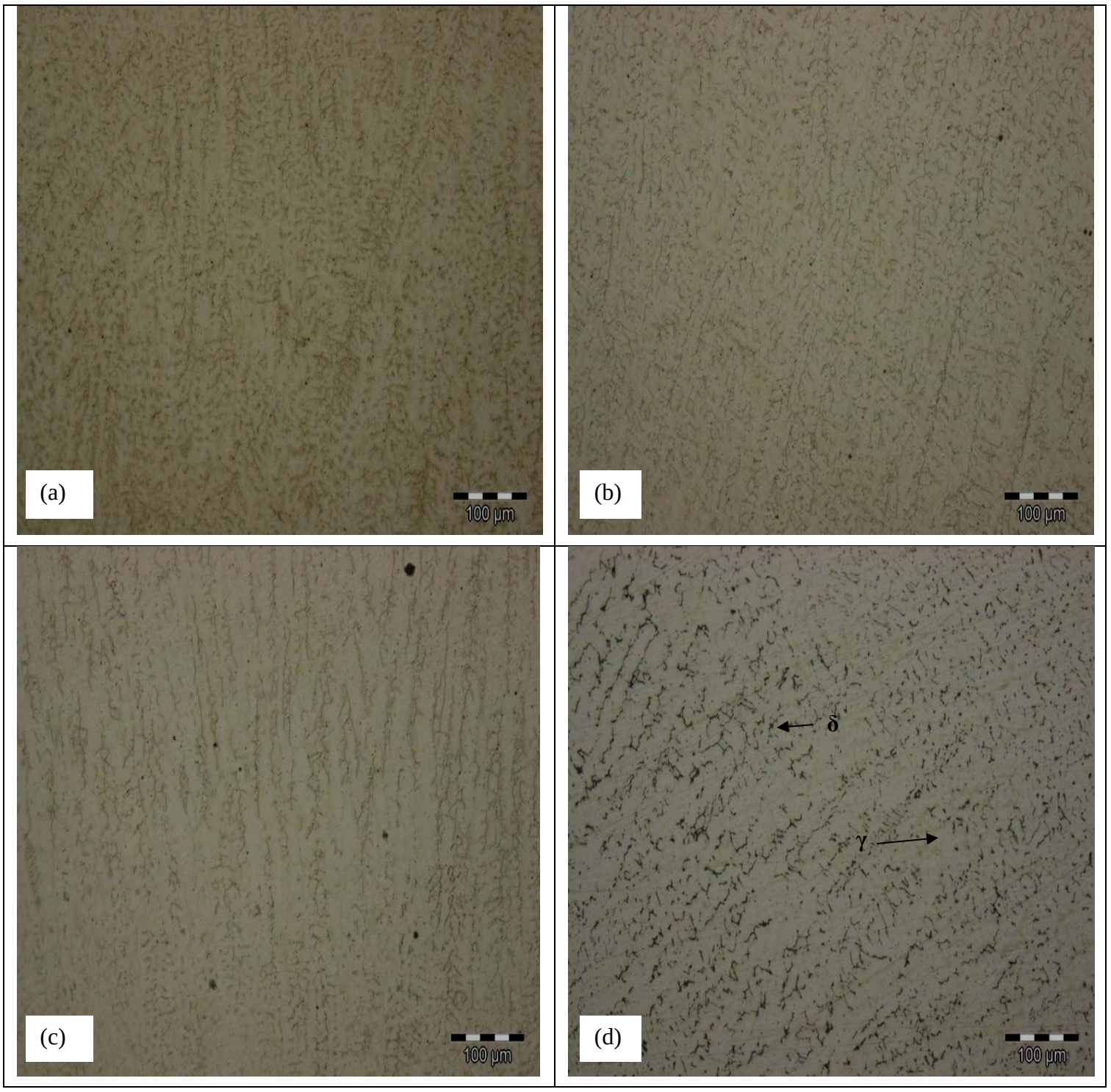

Figure 39: Weld metal microstructure of specimens A to D at X200 magnification after chemical etching with Villela's reagent

The microstructure of specimens A, B, C and D were electrolytically etched with oxalic acid for metallurgical evaluation at X200.

4.2.2 Presence of carbides in the heat affected zone

The schematic of the welded joint in figure 40 shows regions 1, 2, 3, 4 and 5 of the welded joint which are the base metal, heat affected zone of the base metal, the fusion line of the base metal and weld metal, the columnar dendritic region of the weld metal and the mushy zone of the weld metal respectively. Figure 41a-c show the etched base metal, heat affected zone and fusion line of sample A. Figure 41a-c show the etched microstructure of base metal, heat affected zone and fusion line for specimen A which are region 1, 2 and 3 of the weld joint schematic in figure 40.

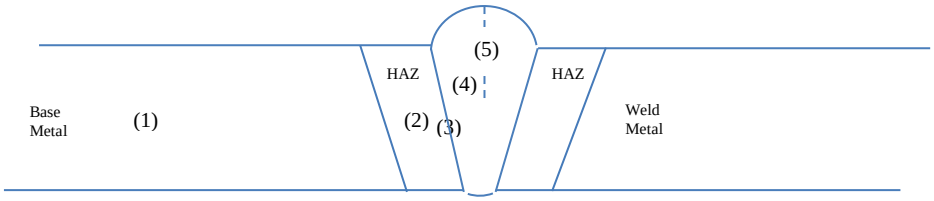

Figure 40: Schematic of weld joint showing (1) base metal, (2), heat affected zone-HAZ, (3) fusion line, (4) columnar dendritic zone and (5) mushy zone.

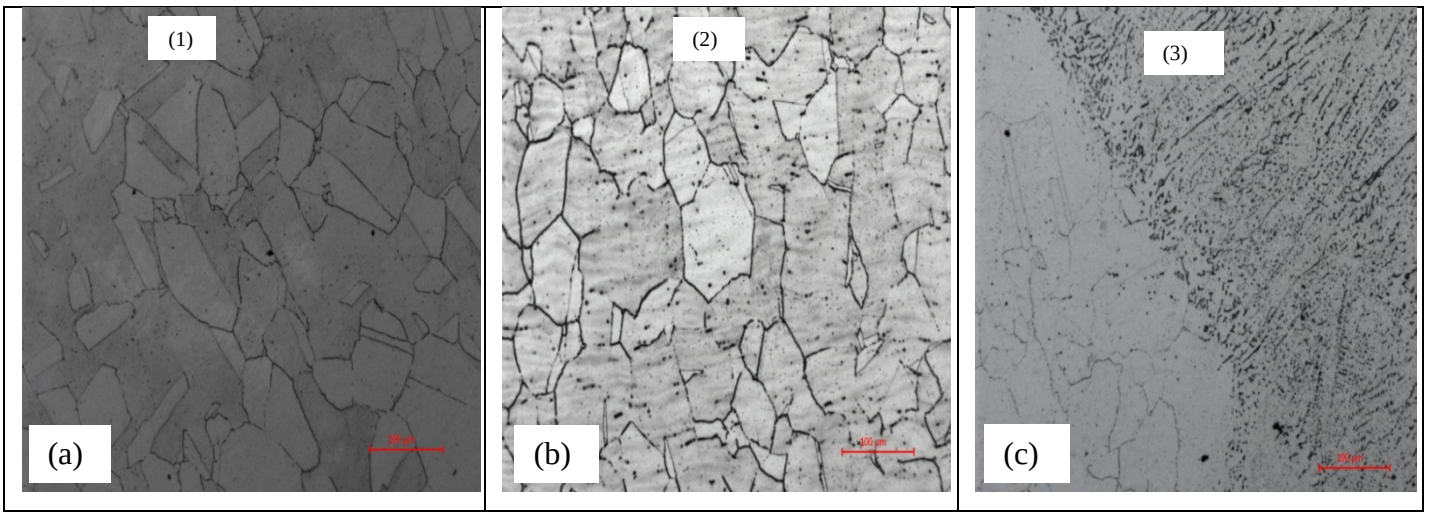

Figure 41: Microstructures of the (a) base metal, (b) heat affected zone and (c) fusion line for specimen A at X200 magnification after etching with oxalic acid.

Figure 42 is a backscatter SEM image taken at X1000 and Figure 43 is an in-lens SEM image of specimen C taken at X10000 in the heat affected zone of specimen C.

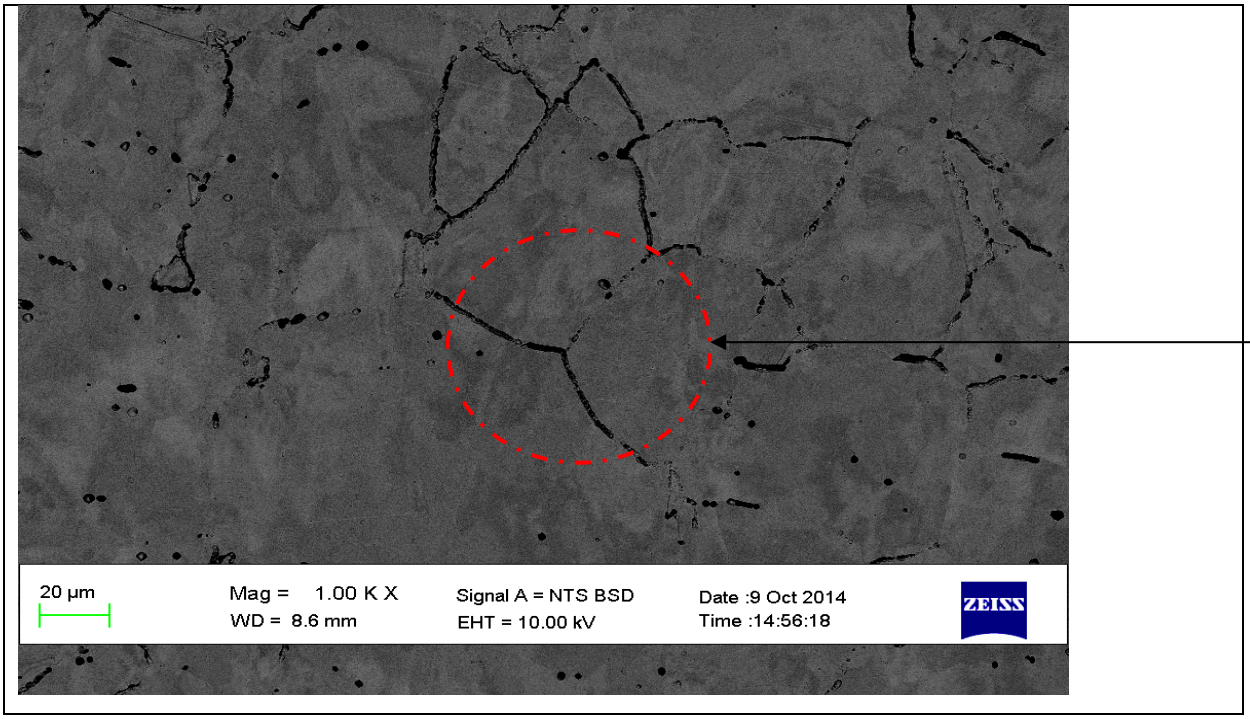

Figure 42: Microstructures of the heat affected zone and fusion line for specimen C at X1000 magnification after etching with oxalic acid.

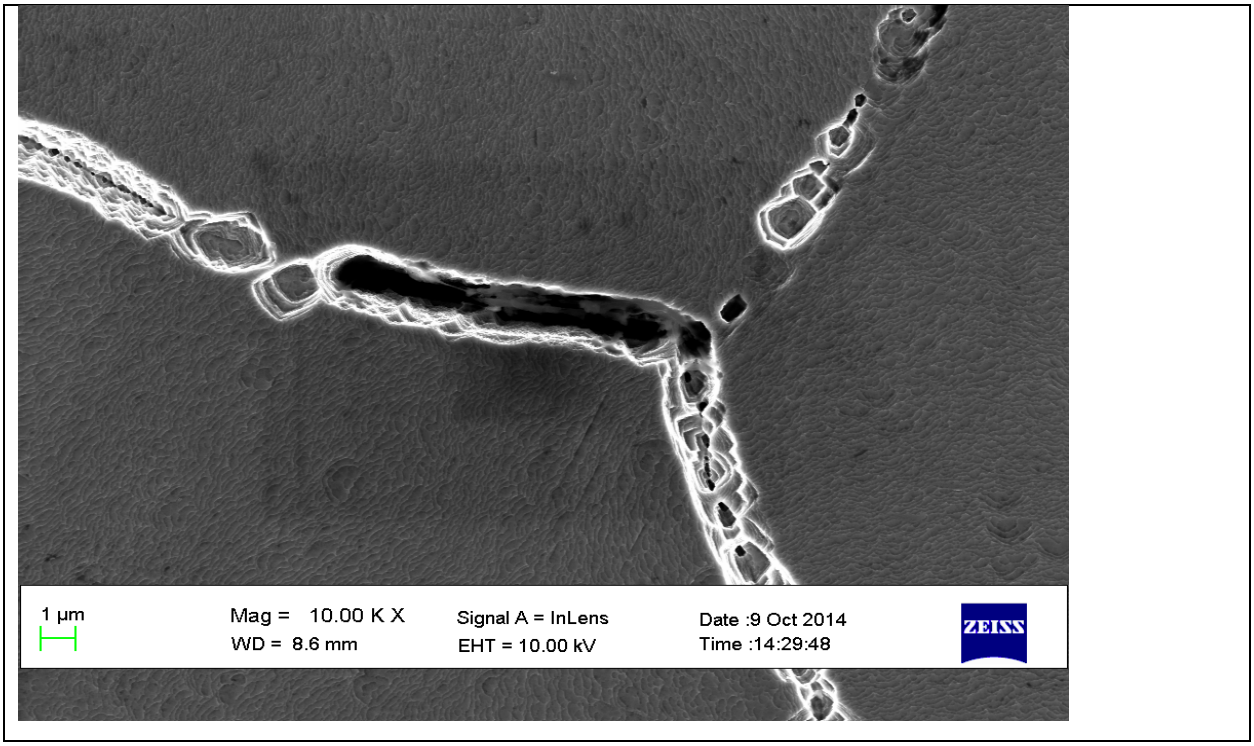

Figure 43: SEM Image of the heat affected zone for specimen C at X10000 magnification after etching with oxalic acid

An EDS analysis was done on grain boundary precipitate and matrix of specimen C to confirm that the elemental composition of the black phase on the grain boundary. Figure 44 shows spectrum 1 i.e. the location on the grain boundary precipitate where the EDS analysis was done. Table 18 shows the composition in weight % and atomic % for the EDS analysis of spectrum 1 in Figure 44. Figure 45 is a graphical representation of the results in table 18. Figure 46 shows spectrum 2 i.e. the location in the matrix where the EDS analysis was done. Table 19 shows the weight % and atomic % for the EDS analysis of spectrum 2 in Figure 46. Figure 47 is a graphical representation of the results in Table 19. When comparing the graphs for spectrum 1 and 2 in Figure 45 and 46 respectively, it is important note that carbon has a high peak. In addition to carbon, chromium and iron (Fe) also had noticeable peaks.

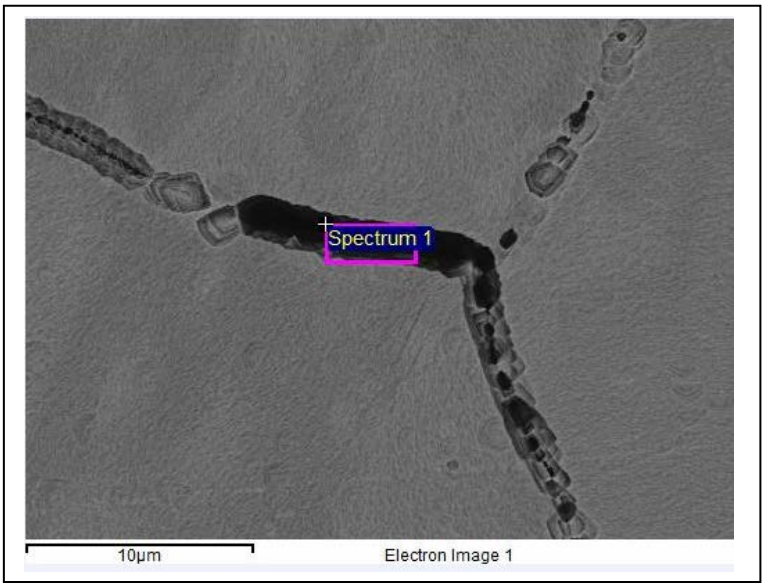

Figure 44: SEM image with location of EDS analysis for spectrum 1 on the grain boundary precipitate of specimen C.

Table 18: Weight % of different elements for EDS spectrum 1 on the grain boundary precipitate of specimen C.

Element	Weight%	Atomic%
C K	16.65	46.63
O K	1.54	3.23
Si K	0.35	0.42
Cr L	18.92	12.24
Fe L	55.99	33.73
Ni L	6.55	3.75

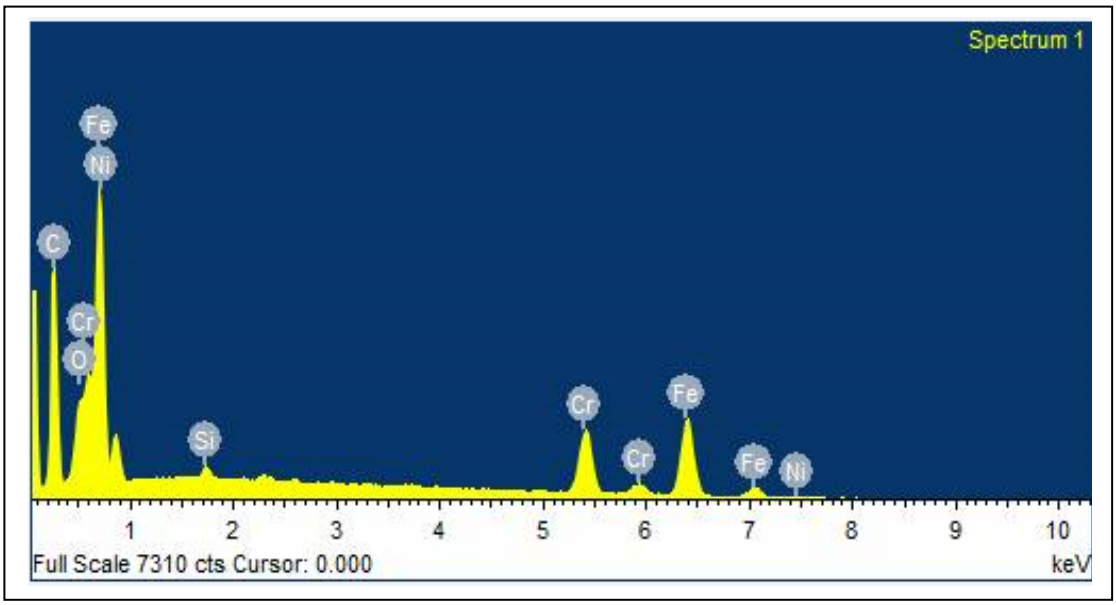

Figure 45: Graph of Spectrum 1 EDS analysis of grain boundary precipitate of specimen C.

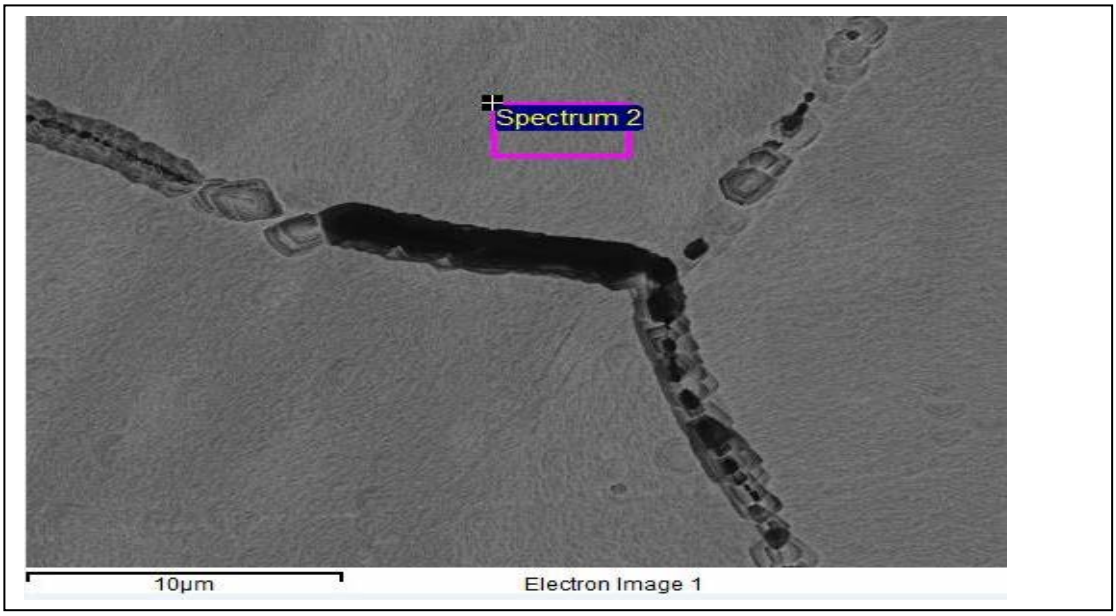

Figure 46: SEM image with location of EDS analysis (spectrum 2) on the matrix of specimen C.

Table 19: Weight % of different elements for EDS spectrum 2 on the matrix of specimen C.

Element	Weight%	Atomic%
C K	1.79	7.73
Cr L	22.10	22.03
Fe L	66.80	62.01
Ni L	9.31	8.22

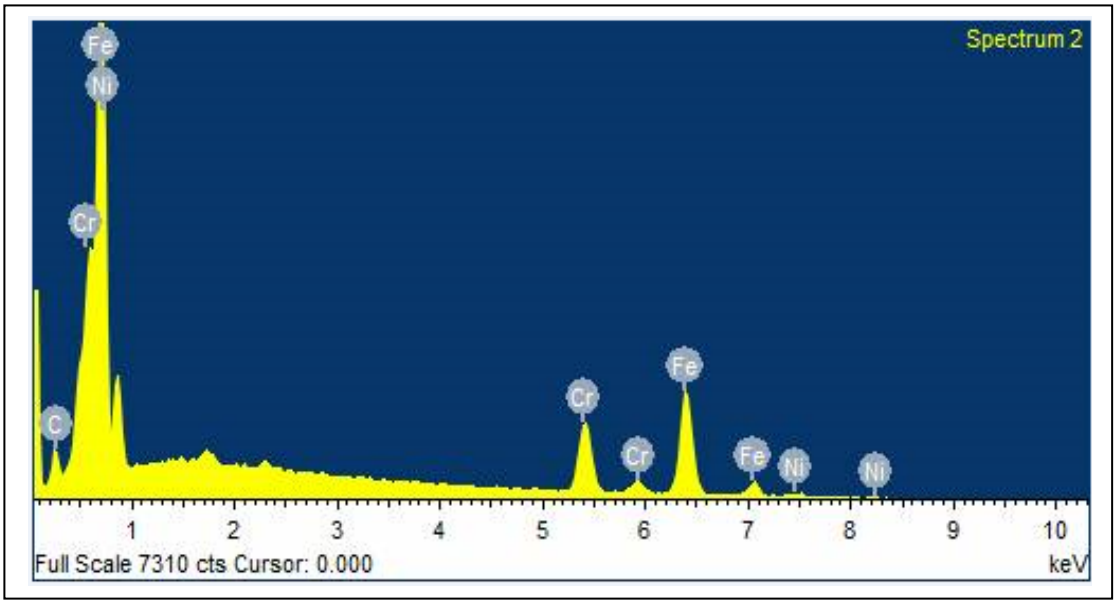

Figure 47: Graph of Spectrum 2 EDS analysis of the matrix of specimen C.

4.2.3 Delta ferrite morphology

Figures 48a-b, 49a-b, 50a-b and 51a-b were electrolytically etched with oxalic acid for metallurgical evaluation at X500 and X1000 magnification. Figures 48 to 51 show the microstructures of the columnar dendritic zone, region 4 in Figure 48, of the weld metal for samples A to D respectively at X500 and X1000 magnification.

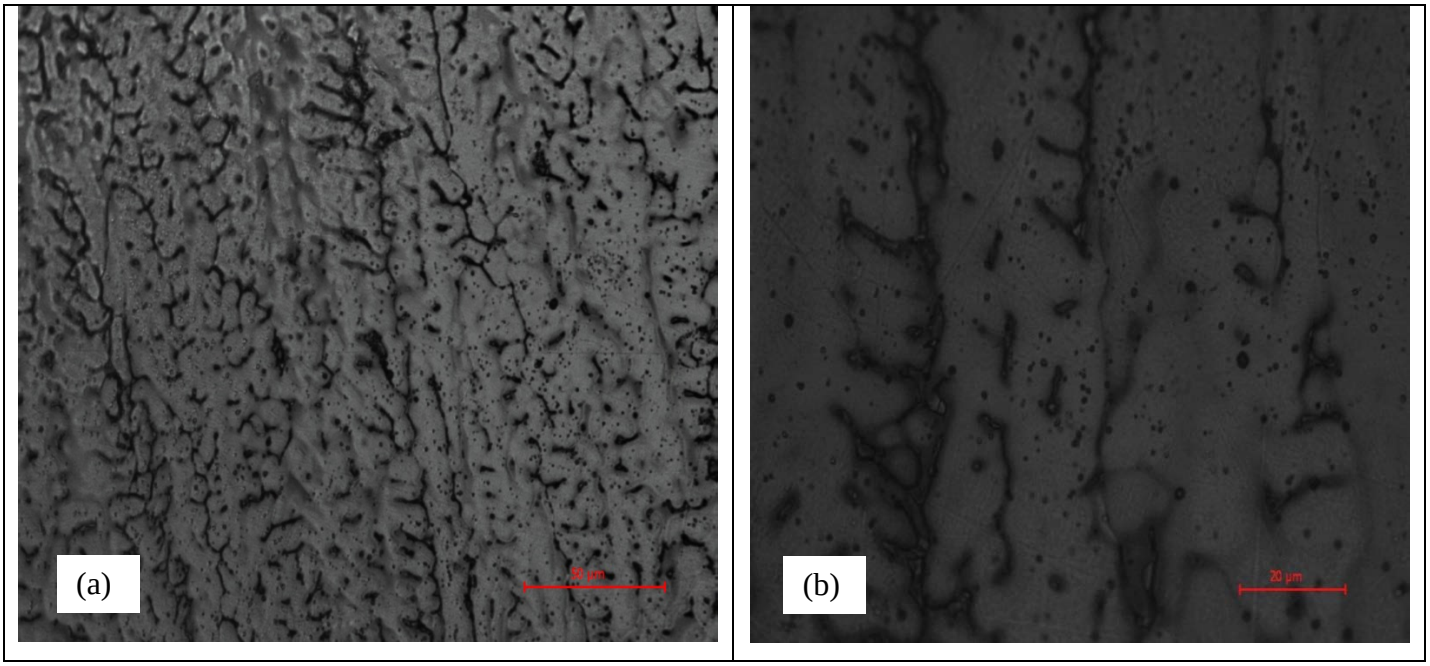

Figure 48: Microstructures of the columnar dendritic zone for specimen A welded at 105-110°C inter-pass temperature at (a) X500 and (b) X1000 after etching with oxalic acid.

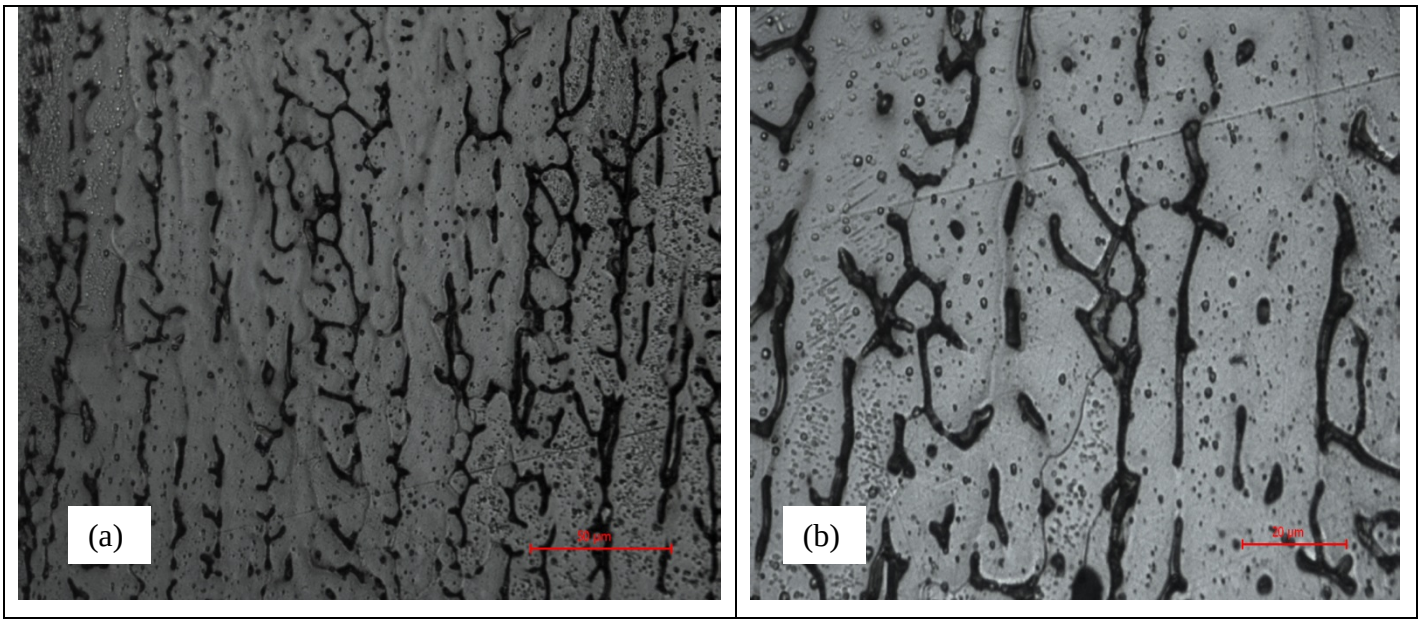

Figure 49: Microstructures of the columnar dendritic zone for specimen B welded at 135-140°C inter-pass temperature at (a) X500 and (b) X1000 after etching with oxalic acid.

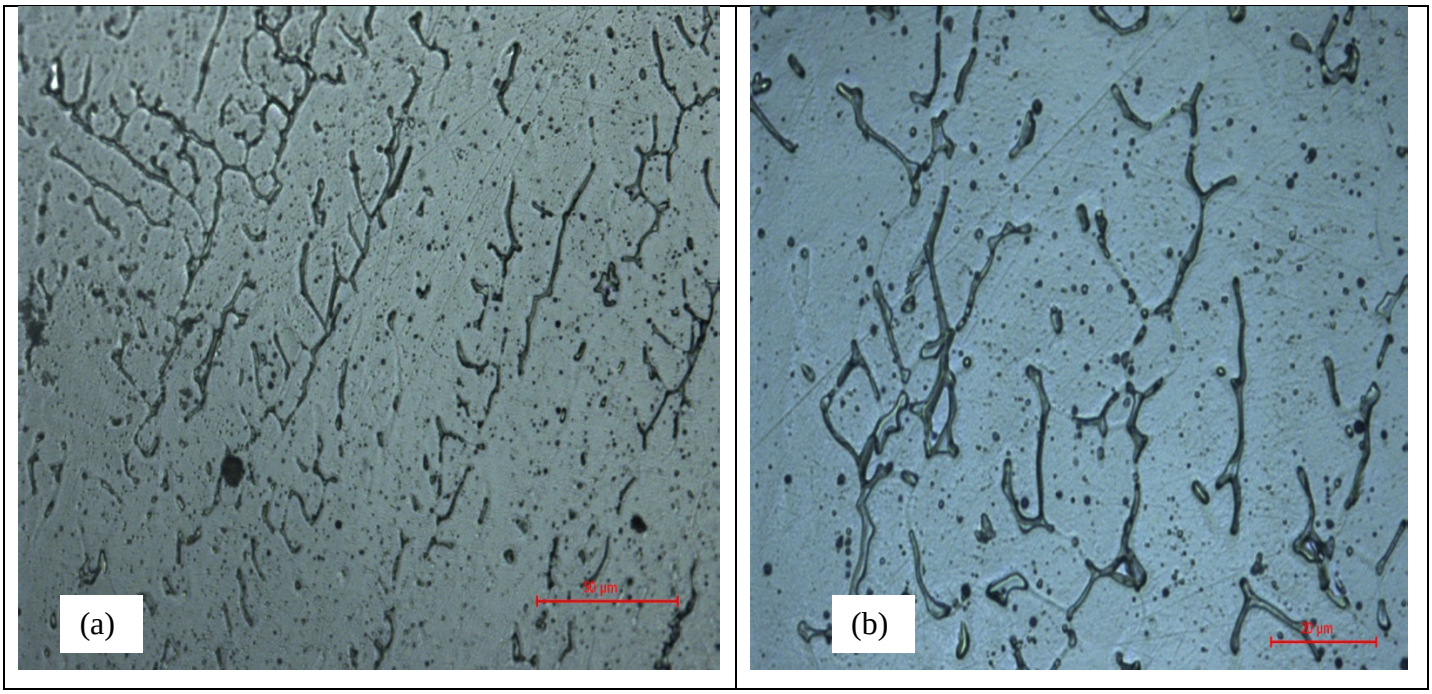

Figure 50: Microstructures of the columnar dendritic zone for specimen C welded at 165-170°C inter-pass temperature at (a) X500 and (b) X1000 after etching with oxalic acid.

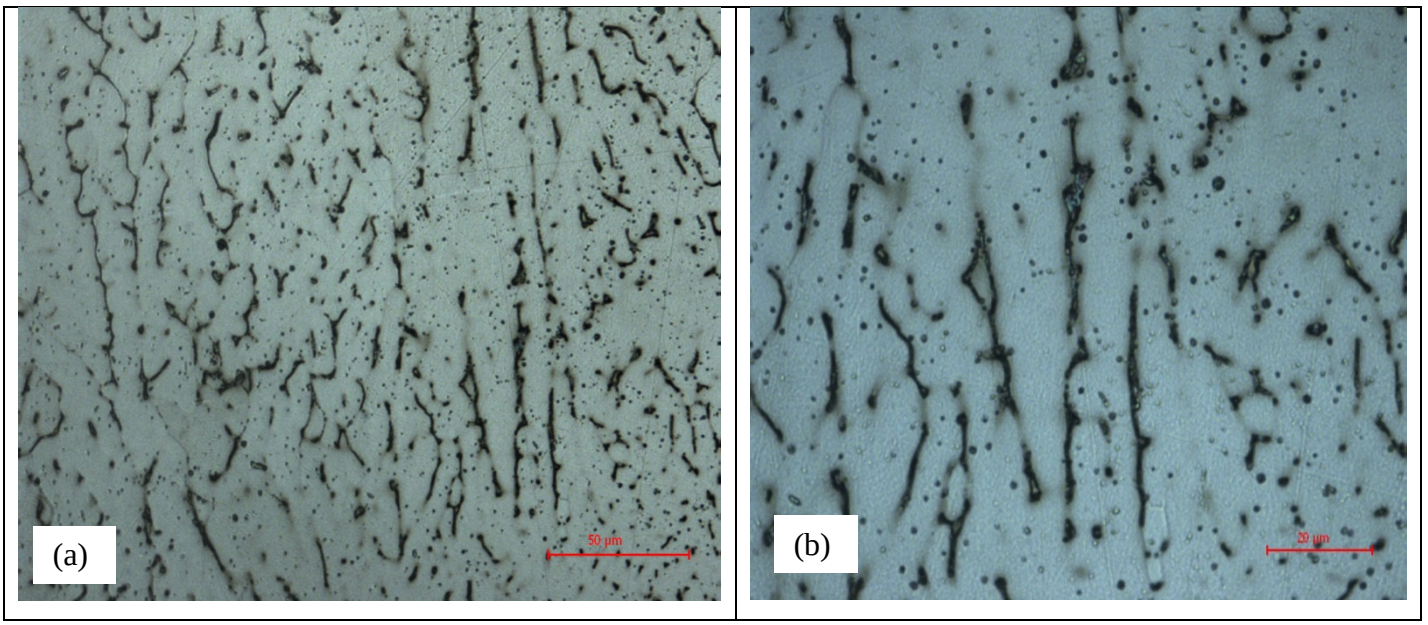

Figure 51: Microstructures of the columnar dendritic zone for specimen D welded at 195-200°C inter-pass temperature at (a) X500 and (b) X1000 after etching with oxalic acid.

4.2.4 Evaluation for Sigma phase transformation in the weld metal

For evaluation of the delta ferrite phase in the weld metal, specimens A to D were electrolytically etched with 21% NaOH, and evaluated with the optical microscope at X1000 magnification. The micrographs were taken in the mushy zone near the centre-line of the weld beads of specimens A, B, C and D as shown in Figure 52.

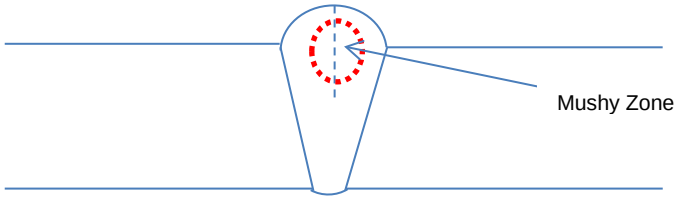

Figure 52: Location of the mushy zone in the weld metal of specimen A to D

Figure 53a-d shows the micrographs taken in the mushy zone of specimens A-D at X1000.

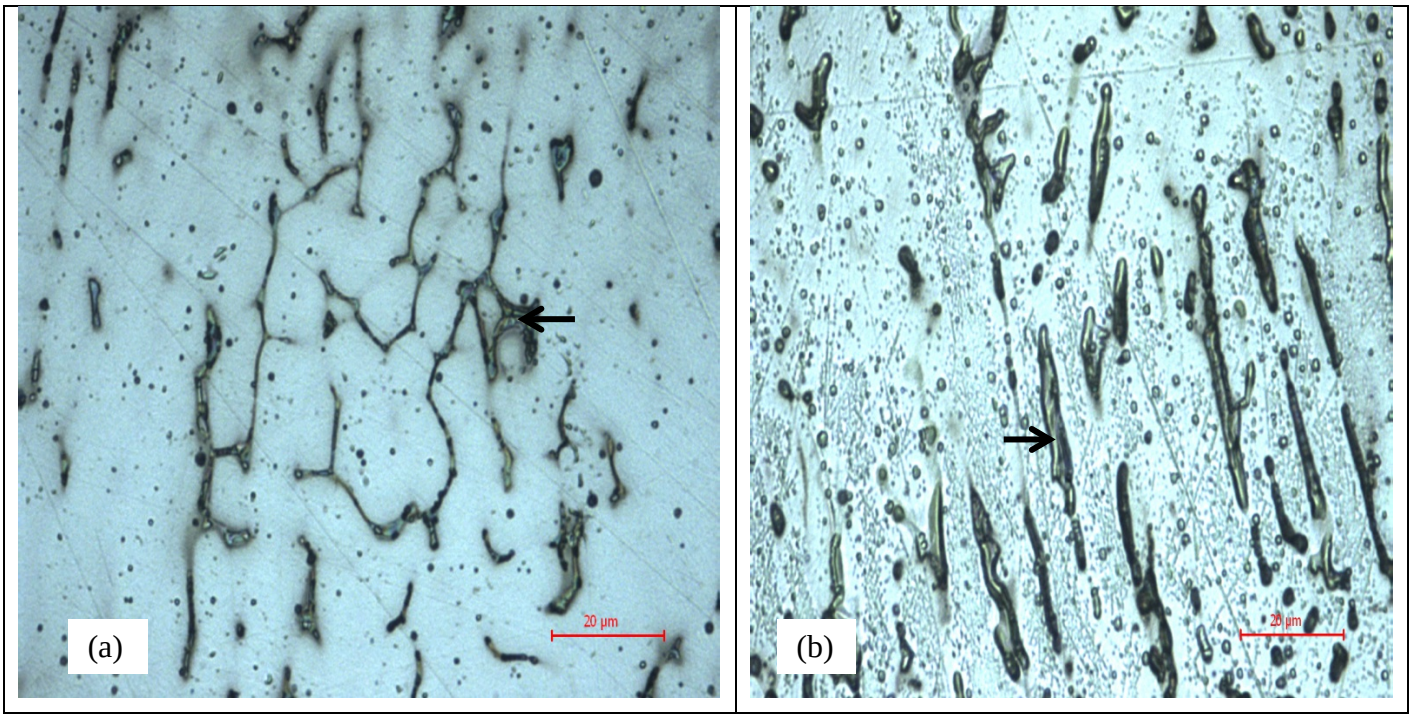

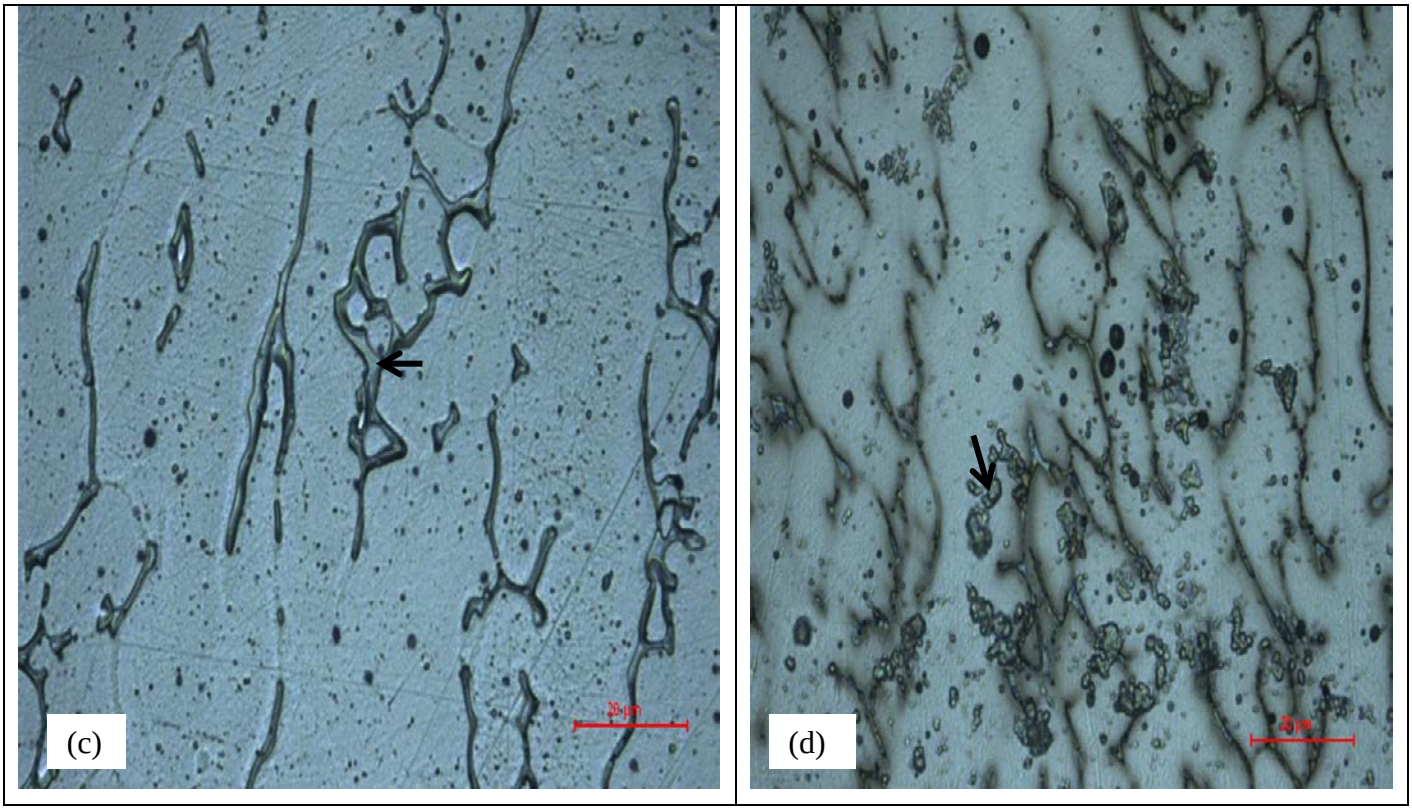

Figure 53: Micrographs of the microstructures of specimens A to D at X1000 magnification after electrolytic etching with NaOH

4.2.5 Low temperature sensitization of heat affected zone

The specimens were etched in Groesbeck reagent to determine the effect of welding inter-pass temperature on the precipitated $M_{23}C_6$ carbide secondary phase. Figures 54a-d show stereographs of specimen A, B , C and D welded at 105-100°C, 135-140°C, 165-170°C and 195-200° inter-pass temperatures respectively taken at X6.7 magnification. Figure 55a-d show micrographs of the heat affected zone (HAZ) of the base metal at X1000 magnification.

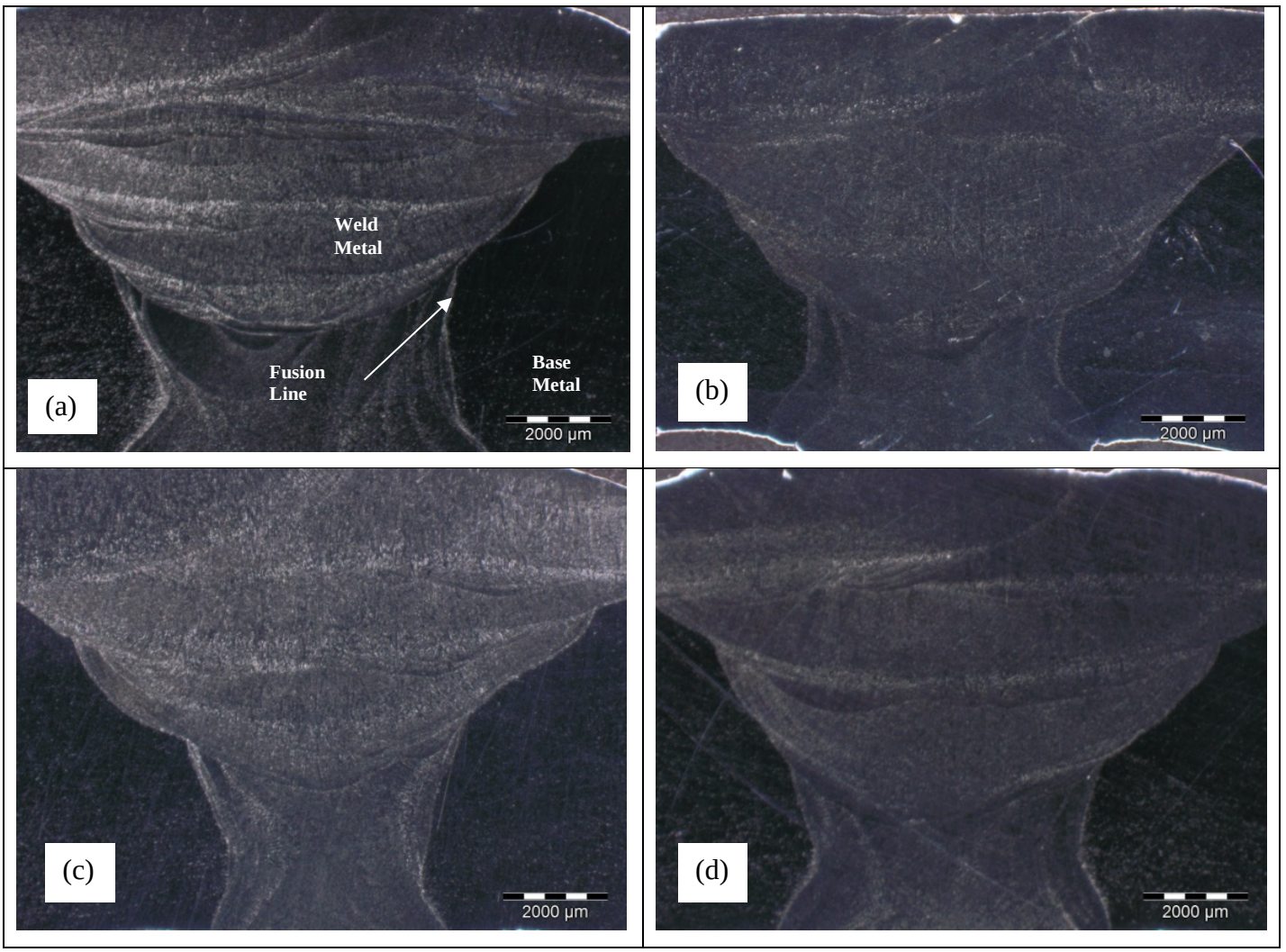

Figure 54: Stereographs of the weld after Groesbeck etchant at X6.7 magnification

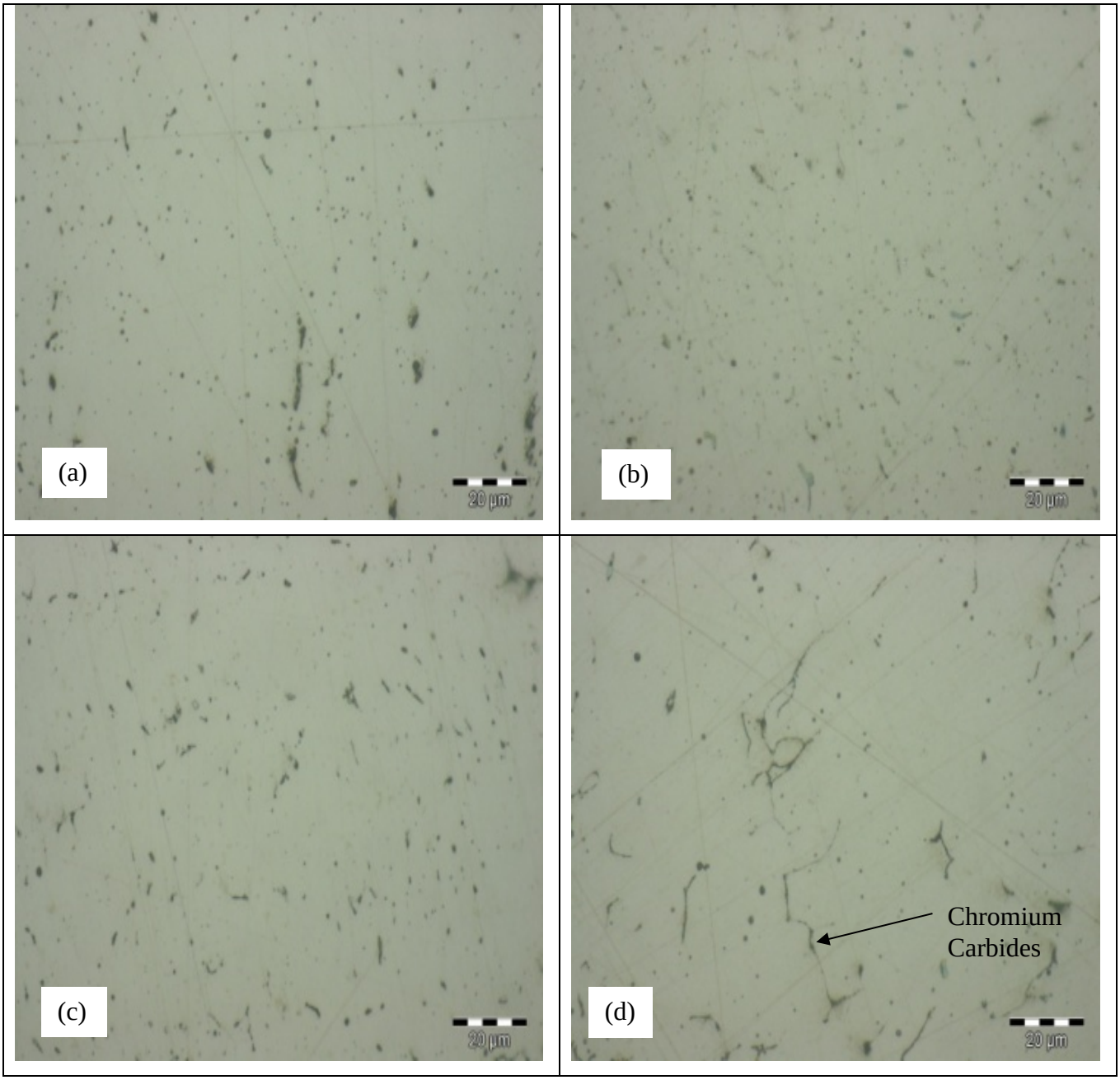

Figure 55: HAZ microstructure of the 304H austenitic steel base metal at X1000 magnification after chemical etching with Groesbeck

V. CHAPTER FIVE - DISCUSSION

5.1 Ferrite numbers

The WRC 1992 constitution diagram predicted ferrite number values shown in Table 17 consistently increased with the increase of welding inter-pass temperature. Specimen A and D welded at interpass temperatures of 105-110°C and 195-200°C respectively have the lowest and highest calculated FN numbers of 1 FN and 3 FN. The Cr_{eq}/Ni_{eq} ratio and WRC-1992 ferrite numbers of the weld metal were calculated using the weld chemical compositions in Table 16. These calculated values showed the Cr_{eq}/Ni_{eq} ratio to increase with an increase in inter-pass temperature. This is because; solute segregation in the weld metal, during cooling, locally raised the concentration of ferrite formers as inter-pass temperature increased. The higher the inter-pass temperature, the stronger the delta ferrite forming tendencies of the weldment were. The cooling rate decreased as inter-pass temperature increased resulting in specimen A, B, C and D welded at inter-pass temperature of 105-110°C, 135-140°C, 165-170°C and 195-200°C having predicted ferrite numbers of FN1, FN2, FN2.5 and FN3 respectively.

The comparison between the WRC 1992 FN values calculated from the weld metal chemical composition and the ferritescope measured values is shown in table 20. The expected instrument error of the Fischer MP30 ferritescope is 0.5 FN for ferrite number values ranging between 0-10FN for measurements taken in the temperature 10-30°C.

Table 20: Comparison between ferritescope measured and the WRC-1992 predicted ferrite numbers

Inter-pass Temp (°C)	10cm Sample	FN (Ferritescope) (%)	FN (WRC-1992)
105 - 110	A	2.3	1
135 - 140	B	3.8	2
165 - 170	C	2.3	2.5
195 - 200	D	2.7	3.0

5.2 Metallurgical feature evaluation

5.2.1 Solidification phases

Figure 39a-d show the main solidification phases of the welded specimens to be delta ferrite in an austenite matrix. The dendrites are of a columnar dendritic morphology. As shown by the arrows in figure 39d, the dark phase in the micrographs is the interdendritic delta ferrite phase (δ) with the lighter phase being the austenite matrix (γ). No micro-fissuring resulting from solidification cracking was observed in any of the welded specimens even though the predicted ferrite numbers of all the specimens was below FN 4. The Cr_{eq}/Ni_{eq} ratio of the weld metal, as calculated from the weld metal chemistry, was 1.36, 1.44, 1.46 and 1.48 for specimens A, B, C and D respectively. It is worth noting that micrographs of specimen A, B and C in figure 39a to 39c respectively are similar in appearance after etching while specimen D in figure 39d appeared different to specimens A, B and C which could be as a result of darker etching. The Cr_{eq}/Ni_{eq} ratios of specimens A, B and C were below 1.48. The Cr_{eq}/Ni_{eq} ration of specimen D was equal to 1.48. The Cr_{eq}/Ni_{eq} ratio of the specimens increased with an increase in inter-pass temperature with the inter-pass temperature range of 105-110°C having the lowest ratio of 1.36 and the inter-pass temperature range of 195-200°C having the highest ratio of 1.48. The solidification mode is therefore expected to be a combination of the austenite-ferrite (AF) and the ferrite-austenite (FA) solidification modes. The weld metal microstructural evaluation of the specimens revealed that specimen A had an austenitic matrix with a columnar dendritic morphology and delta ferrite with an interdendritic morphology which indicates the austenite-ferrite (AF) solidification following the $L \rightarrow L + \gamma \rightarrow L + \gamma + \delta \rightarrow \gamma + \delta$ solidification sequence. Specimens A, B, C and D all had a mixed delta ferrite morphology containing some interdendritic with predominantly vermicular delta ferrite which is an indication of a combination of the austenite-ferrite (AF) and ferrite-austenite (FA) solidification modes. Some areas of the weld metal therefore followed the FA, $L \rightarrow L + \delta \rightarrow L + \delta + \gamma \rightarrow \gamma + \delta$, solidification sequence while other areas of the weld bead followed the AF solidification sequence similar to that already described for specimen A. This mixed solidification mode is not surprising as the Cr_{eq}/Ni_{eq} ratios for specimens B, C and D were 1.44, 1.46

and 1.48 respectively which were very close to the 1.48 ration required for the FA solidification mode to start dominating.

No solidification cracking was observed in any of the specimens evaluated in this study even though all the specimens had ferrite contents well below FN 4 in the center line of the weld beads. The minimum ferrite content of FN 5 was required to prevent solidification cracking. This observation supports research that indicates that controlling of the primary solidification mode as delta ferrite is more important a factor in preventing solidification cracking than trying to control the actual ferrite content of the weld metal. By controlling the weld metal chemistry to have a chromium-nickel-equivalent ratio to be close to 1.48 ensured that delta ferrite would be part of the primary solidification phase which has higher solubility for the sulphur and phosphorus impurities present at high temperatures than what austenite does and therefore reducing susceptibility of the weld metal to solidification cracking.

5.2.2 Delta ferrite morphology

Figure 41a showed an annealed structure consisting of equiaxed austenite grains with annealing twins. Figure 41b showed a location of the heat affected zone which was exposed to temperatures in the sensitization range during welding because the precipitated carbides are both within the grains and on some of the grain boundaries. Grain growth was also evident. Figure 41c showed the coarse grain structure of the base metal on the fusion line. As aforementioned in the, Figures 48, 49, 50, and 51 showed the microstructures of the columnar dendritic zone of the weld metal for samples A to D respectively. The columnar dendritic zone is region 4 of the schematic in figure 35. The presence of delta ferrite in the weld metal microstructures of specimens A to D of figures 48 to 51 indicates that the 308H weld metal welded to the 304H base metal passed through the 3 phase region of the Cr-Ni-Fe phase diagram shown in Figure 14. A mixed morphology with mostly vermicular delta ferrite and some interdendritic delta ferrite in specimens A B, C and D was observed in figures 48 to 51. This mixed morphology resulted from differences in chromium content to due solute segregation during cooling. In the regions of the weld microstructure where the delta

ferrite had dendritic arms, the delta ferrite was the first phase to solidify (FA solidification mode) and became the nuclei for the delta ferrite-austenite transformation. As the chromium rich weld metal cooled into the (δ + γ) two-phase region, the outer portions of the dendrites having less chromium transform to austenite. The delta ferrite-austenite transformation therefore started at the boundary of the delta ferrite dendritic arms and rapidly progressed to the core of the delta ferrite dendrite. This morphology where delta ferrite has dendritic arms is called vermicular ferrite. The regions of the microstructures for specimens A to D where the core of the delta ferrite, with no distinct dendritic arms, was located at the austenitic grain boundary, austenite was the first phase to solidify before the delta ferrite solidified (AF solidification mode). It is worth noting that the delta ferrite morphology of specimen B in figure 49 revealed a combination of a vermicular-lathy and interdendritic morphology. The lathy ferrite of specimen B in figure 49 was an indication of the higher chromium content in the some regions of the weld metal in this sample while the vermicular morphology showed that some regions were lower in chromium content than the lathy ferrite regions; both the vermicular and lathy ferrite regions followed the FA solidification mode sequence.

5.2.3 *Sigma phase transformation in the weld metal*

The transformation sequence of delta ferrite to sigma phase is such that only after all the nucleated delta ferrite has transformed to sigma phase will the austenite to sigma phase transformation occur on the grain boundary starting at the triple points of the grain boundary. The austenite to sigma phase transformation is slow and only occurs after long term exposure in the sigmatization temperature. Electrolytic etching with 20% NaOH will the delta ferrite phase blue/tan and the sigma phase will be coloured brown-orange (van der Voort, 2011). The microstructure at the mushy zone revealed the presence of delta ferrite dendrites in an austenitic matrix. The welded specimens A to D in figure 53a-d respectively showed no distinct presence of sigma phase in their as-welded condition.

5.2.4 Low temperature sensitization of heat affected zone

Low temperature sensitization occurred after welding in the heat affected zone (HAZ) adjacent to the fusion zone of specimens A, B, C and D welded at 105-100°C, 135-140°C, 165-170°C and 195-200° inter-pass temperatures respectively. Figures 54a-d show stereographs taken at X6.7 magnification while Figure 55a-d shows micrographs taken at X1000 magnification. The evaluation at X1000 magnification, shown in figure 55a-d, indicated a difference in the carbide between specimens A, B, C and specimen D. Specimens A to C at X1000 showed nucleated carbides with no carbide networks while specimen D revealed discontinuous networks of carbides that had formed during the welding of this specimen at an inter-pass temperature 195-200°C. This is because specimens A, B and C were briefly exposed to the sensitization temperature range upon cooling. The chromium carbides nucleated in specimen D which was welded at 195-200°C formed a discontinuous network of carbides through diffusion. The carbide networks that started to form show that specimen D experienced enough slow cooling through the sensitization temperature range. This confirms that the cooling rate experienced in specimen D was slower than those experienced during the welding of specimens A, B and C. The EDS analysis of the grain boundary using SEM confirmed that the grain boundary precipitate, spectrum 1 shown in Figure 45, had a carbon peak that was relatively higher than that of the EDS analysis for matrix, spectrum 2 shown in Figure 47. Unfortunately the high peak of carbon in the spectrum could not be quantified with the EDS because the carbon is a light element with a Kα value of 0.277. The Kα value for carbon is therefore too low to quantify with the EDS.

VI CHAPTER SIX - CONCLUSION

The study into the effect of welding inter-pass temperature when welding 304H type austenitic stainless steel using the shielded metal arc welding (SMAW) process revealed the following points:

a) The ferrite numbers calculated using chemical composition of the weld metal and the WRC 1992 constitution diagram showed a positive correlation between the welding inter-pass temperature and the ferrite number. The predicted ferrite numbers plotted on the WRC 1992 diagram increased with an increase in inter-pass temperature while the measured ferrite number values did not. The lack of correlation between the calculated ferrite numbers and measured ferrite number values can be attributed to the instrument error of 0.5FN and/or ferrite measurement procedures not being adequately followed.

b) Etching with Groesbeck reagent revealed that the nature of low temperature sensitisation in the heat affected zones (HAZ) of the base metal changed with an increase in inter-pass temperature. A maximum inter-pass temperature of 165-170°C should be maintained to avoid sensitisation when welding 304H austenitic stainless steel. The maximum temperature limit of 170°C is consistent with API recommended practice 582. When considering the effects of inter-pass temperature on low temperature sensitization, it is clear that interpass temperature has a stronger influence on sensitization than what is does on ferrite number. The interpass temperature reduces the cooling rate of the weld which result in the formation of discontinuous chromium carbide networks at interpass temperatures of 170°C because the cooling rate allows sufficient time for chromium carbide diffusion while the weld passes through the sensitization temperature range. The chromium carbide grain boundary precipitate was confirmed with a SEM EDS analysis.

c) Primary solidification mode changed with an increase in inter-pass temperature. The Cr_{eq}/Ni_{eq} ratios of specimens A, B and C were below 1.48 which indicates that the theoretical dominating primary modes of solidification would be the austenite-ferrite (AF) solidification mode in figure 15. The Cr_{eq}/Ni_{eq} ratio of specimen D was 1.48 which indicates that the theoretically dominating primary solidification mode would start changing from the AF primary solidification mode to the ferrite-austenite (FA) solidification mode. No solidification cracking was observed in any of the specimens evaluated in this study even though all the specimens had ferrite contents well below FN 5 in the center line of the weld beads. The SAPREF Refinery internal quality standards required a minimum ferrite content of FN 5 to prevent solidification cracking. This observation supports research that indicates that controlling of the primary solidification mode as delta ferrite is more important a factor in preventing solidification cracking than trying to control the actual ferrite content of the weld metal.

d) After evaluating the solidification phase and the evolution of secondary phases of the specimens after welding. The shielded metal arc welding variables used in the welding of specimen B, welded at an inter-pass temperature of 135-140°C, were the most optimum as they resulted in an average weld metal ferritescope ferrite content measurement of 3.8%, equivalent to FN 3.8, which was closest to the desired weld metal ferrite number of 5-8 FN.

VII CHAPTER SEVEN - FUTURE WORK OPPORTUNITIES

- To determine the influence of welding interpass temperature on delta ferrite content and solidifation mode on 304H stainless steel when welding with higher heat input welding process e.g. GMAW and SAW.
- The parent metal used in this research fell marginally in the Type 304H range and could have been classified as a Type 304 stainless steel; further work can be done with the use of Type 304H parent material which has a carbon content greater than 0.071 wt%.

VIII REFERENCES

1. Albright, L.F., & Hansen, D.A., 2009, '*Albright's chemical engineering handbook',CRC Press, Boca Raton, Florida.*
2. Ahlblom, B., Sandström, R., 1982, 'Hot workability of stainless steels: influence of deformation parameters, microstructural components, and restoration processes', *International Metals Reviews*, vol. 27, Issue 1, pp.1-27.
3. American Petroleum Institute., 2003,'Calculation of heater tube thickness in petroleum and natural gas industries', *American Petroleum Institute recommended practice 530,* 5th ed, API Publishing Services, Washingtin DC.
4. American Petroleum Institute., 2009, 'Welding guidelines for the chemical, oil and gas industries', *American Petroleum Institute 582,* 2nd ed, API Publishing Services, Washingtin DC.
5. Andresen, P. L., Solomon, H. D., & Taylor, D. F., 1981, 'Basic Studies on the Variabilities of Fabrication-Related Sensitization Phenomena in Stainless Steels', EPRI NP-1823, Project 1072-1, Final Report, May 1981, pp. 2–18.
6. ASME. 1977 (July). *1977 code cases, nuclear components,* 1977 ed., case N-47-12 (1592-12), appendix 1-14, table 1-14.6A, p. 152. New York.
7. Atlas steels, 2011, *Atlas Tech Note No. 8.* August 2011. *pdf*, viewed 20 April 2014, from http://www.atlassteels.com.au/documents.
8. Bermejo, M., 2012, 'Predictive and measurement methods for delta ferrite determination in stainless steels', *Welding journal*, April 2012, pp. 11-12.
9. Binder, W.D., Brown, C.M., 1946, 'Proceedings of the American society for testing and materials', Vol. 46, pp. 593.
10. Bramfitt, B., & Benscoter, A., 2002, metallographic guide: practices and procedures for irons and steels', ASM International, Materials Park.
11. Briant, C.L., 1882, 'Effects of nitrogen and cold work on the sensitization of austenitic stainless steels', *EPRI NP-2457, Project 1574-1, final report*, June 1982.
12. Bruemmer, S., & Gas, G.,1994, 'Microstructural and microchemical mechanisms controlling intergranular stress corrosion cracking in light-water-reactor systems', *Journal of Nuclear Materials* 216, pp. 348-363.

13. Castro, R & de Cadanet, J.J., 1975, *Welding metallurgy of stainless & heat resistant steels*, Cambridge University Press Bentley House, Euston, London.
14. Chalmers, B., & Rutter, J.W., 1953,'Á prismatic substructure formed during solidification of metals', *Canadian Journal of Physics*, vol. 31, no. 1, pp.15-39.
15. Davis, J.R., 1994, '*ASM specialty handbook: stainless steels*', ASM International, Ohio.
16. Dillon, C.P., & Dekker, M., 1995, 'Corrosion resistance of stainless steels: high-temperature applications, pp. 245-269.New York.
17. Long, C.J., & Delong W.T., 1974 'Ferrite in austenitic stainless steel weld metal', *Welding Journal* 52(7), pp. 281s-297s.
18. Elmer, J.W., Allen, S. M., and Eagar, T.W., 1989, *Metallurgical and materials transactions, Vol* 20A, 1989, pp. 2117.
19. Escriba, D.M., Pimenta Jr, F.C., Plaut, R.L., & Padihla, A.F., 2006, 'Comparative study on sigma phase precipitation of three types of stainless steels: austenitic, superferritic and duplex', *Materials Science and Technology*, 22(9), 1098-1104.
20. Folkhard, E., Rabensteiner, G., Perteneder, E., Schabereiter, H., & Tosch, J., 1984, *Welding metallurgy of stainless steels*, Springer-verlag/Wien, New York.
21. Funderburk, R. S., 1998, 'Key concepts in welding engineering: the importance of inter-pass temperature', *Welding Innovation,* vol. xv, No 1.
22. Funderburk, R. S., 2000, 'Taking your weld's temperature', *Modern Steel Conctruction,* February 2000.
23. Handbook committee & Olson, D.L., 1993, *ASM handbook: Welding, brazing, and soldering*, vol. 6, ASM International.
24. Handbook committee & Olson, D.L., 1993, *ASM handbook: Metallography and Microstructures,* vol. 9, ASM International.
25. Hedström, P., Lienert, U., Almer, J., & Odén, M., 2008, 'Elastic strain evolution and ε-martensite formation in individual austenite grains during in situ loading of a metastable stainless steel', *Mater Letter*, Vol. 62, pp. 338-340.
26. Jorge, L., Seijas, H., & Seijas, A., 2006, 'Sigma phase embrittlement of stainless steel in fcc service', *NACE International Conference,* San Diego Ca, 16 March 2006.
27. Kaushish, J. P., 2008, '*Manufacturing processes'*, Prentice-Hall, Connaught Circus, New Delhi.

28. Keown, S.R., 1980, 'Hot ductility of wrought austenitic stainless steels part I: Effect of alloying additions', In: Hot working and forming processes, *The Metals Society*, pp. 140-147. London.
29. Kontecki, D. J., & Siewert, T.A., 1992, 'WRC-1992 constitution diagram for stainless steel weld metals:A modification of the WRC-1998 diagram', *Welding Journal* , May 1992, pp. 171s-178s.
30. Korinko, P.S., & Malene, S.H., 'Considerations for the weldability of type 304L and 316L stainless steels', *Practical failure analysis,* vol. 1, no 4, pp. 61-68.
31. Kou, S., 2003, *Welding Metallurgy*, 2nd ed, John Wiley and Son Inc, Hoboken, New Jersey.
32. Kujanpaa, V., Suutala, N., Takalo, T. & Moisio, T., 1979, *Welding Research International, vol.9,* pp. 55.
33. Kutz, M., 2002, Handbook of materials selection, John Wiley and Sons, New York.
34. Lacombe, P., Baroux, B., Beranger, G., 1993, 'Stainless Steels', *Editions of the Pysiques Les Ultis*, pp. 42.
35. Lee, C.H., 1985, 'The effect of welding variables on HAZ sensitization behaviour of austenitic stainless steels', The University of Tennessee, March 1985.
36. Losert, W., Shi, B.Q., & Cummings, H.Z., 1998, 'Evolution of dendritic patterns during alloy solidification: Onset of the initial instability' *Proceedings of the National Academy of Science of the United States*, vol. 95, no 2, January 1998, pp. 431-438.
37. Lippold, J.C., & Savage, W.F., 1982, 'Solidification of austenitic stainless steel weldments: part 3 – The effect of solidification behaviour on hot cracking susceptibility', *Welding Journal*, vol. 61, no 12, December 1982, pp. 338-396.
38. Lundin, C.D., Chou, C.P.D., & Sullivan, C.J., 1980, 'Hot cracking resistance of austenitic stainless steel weld metals', *WRC Bulletin 256*, 226-252.
39. Marshall, P., 1984, Austenitic Stainless Steels: Microstructure and mechanical properties, Elsevier Applied Science, pp. 23, London.
40. Mehl, R.F., 1972, 'Metals Handbook: Atlas of microstructures of industrial alloys', 8th Ed, vol. 7, Materials Park, Ohio.
41. Milada,M., Zreibaa, M., Elhalouanib, F., Baradaib, C., 2008, 'The effect of cold work on structure and properties of AISI 304 stainless steel', Journal of Materials Processing Technology, Vol. 203, pp.80–85.

42. Mumtaz, K., Takahashi, S., Echigoya, J., Kumara, K., Zhang, L., Kikuchi, H., Ara, K., & Sato, M., 2004, 'Magnetic measurements of the reverse martensite to austenite transformation in a rolled austenitic stainless steel', Journal of Material Science, Vol 39, pp. 1997–2010.
43. M´Esz´Arosa, I., & Proh´Aszkab, J., 2005, 'Magnetic investigation of the effect of ά-martensite on the properties of austenitic stainless steel', *Journal of Material Processing Technology*, Vol 161, pp 162–168.
44. Nickel Development Institute., 1992, 'Guidelines for welded fabrication of nickel-containing steels for corrosion resistant service', *The Nickel Development Institute* Reference Book Series N° 1100, 26-27. Viewed from, www.nickelinstitute.org/index.cfm/ci_id/15786/la_id/1.htm
45. Ogawa, T., & Tsunetomi, E., 1982, 'Hot cracking susceptibility of austenitic stainless steels', *Welding Journal*, March 1982, pp. 82-93.
46. Petzow, G., 1978, *Metallographic etching: techniques for metallogrpahy, ceramography, plastography,* 2nd Ed, ASM International, Metals Park, Ohio.
47. Padilha, A.F., Tavares, C.F., Martorano, M.A., 2013, 'Delta ferrite formation in austenitic stainless steel castings', *Material Science Forum Vols. 730-732, pp.733-738.*
48. Padilha, A.F., Plaut, R.L., & Rios, P.R., 2007, In: Totten GE (editor). Stainless steels heat treatment (chapter 12). *Steel heat treatment handbook*, 2 ed, pp. 695-739, CRC Press, Boca Raton, Florida.
49. Padilha, A.F, Plaut, R.L., & Rios, P.R., 2003, 'Annealing of cold-worked austenitic stainless steels', *ISIJ International (Japan),* 43(2), pp. 135-143.
50. Padilha, A.F, & Guedes, L.C., 1994, 'Austenitic stainless steels: Microstructure and properties', pp. 27-61, Hemus Publishing Limited, São Paulo.
51. Plaut, L. R., Herrera, C., Escriba, M. D., Rios, P. R., & Padilha A. F., 2007, 'A short review on wrought stainless steel at high temperatures: processing, microstructure, properties and performance', *Materials Research*, vol. 10, no 4, October 2007, pp. 453-460.
52. Priceputu, I.L., Moisa, B., Chiran, A., Nicolescu, G., & Bacinschi, Z., 2011, 'Delta ferrite influence in AISI 321 stainless steel welded tubes', *The Scientific Bulletin of Valahia University – Materials and Mechanics* 6(9), 87-96.
53. Povich, M.J., & Rao, P., 1978, 'Low temperature sensitization of welded type 304 stainless steels', Corrosion vol.34, No. 8

54. Rao, K., & Prasannakumar, S., 1984, 'Assessment criterion for variability of delta ferrite in austenitic weld and clad metals', *Welding Research Supplement,* July 1984*,* pp. 231-236.
55. Rivlin, V.G., & Raynor, G.V., 1980, *International Metals Reviews, vol.* 1, pp. 21-38.
56. Schmidt, C.G., Caligiuri, R.D., Eiselstein, L.E., & Wing, S., 1983, 'Low tempeterature sensitization of type 304 stainless steel weld heat affected zone', *EPRI Project T110-1, final report,* November 1983.
57. Schramm, R. E., & Reed, R. P., 1975, 'Stacking fault energies of seven commercial austenitic stainless steels', Metallurgic. Material. Transaction. A., Vol. 6, pp 1345-1351.
58. Sedriks, J.A., 1996, *Corrosion of stainless steels*, 2nd Ed, John Wiley and Sons Inc, Third Avenue, New York.
59. Siewert, T.A., M_cCowan, C.N., & Olson, D.L., 1989, 'Stainless steel weld metal: prediction of ferrite content' *WRC Bulletin(324),* pp. 36
60. Singh, R., 2011, *Applied welding engineering: processes, codes and standards*, Elsevier, viewed 04 February 2014, from http://books.google.co.za/books.
61. Smith, G. V., 1969, 'An evaluation of the yield, tensile, creep, and rupture strengths of wrought 304, 316, 321, and 347 stainless steels at elevated temperatures', ASTM data series DS 5S2 prepared for the Metal Properties Council, *American Society of Testing and Materials*. February 1969, Philadelphia.
62. Stickler, R., Vincier, A., 1961, 'Nucleation of $M_{23}C_6$ on various phase boundaries in an Fe-18Cr-8Ni-0.52Mo-0.038C stainless steel' *Acta Metallurgica*: vol.9, pp.898.
63. Svensson, L.E., Hidesjo, C.,1999, 'Exploiting Advances in Arc Welding Technology: Consumables for welding high strength steels', Abington Publishing, Cambridge, England.
64. Svensson, L. E., 1994, 'Control of Microstructures and Properties in Steel Arc Welds', CRC Press Inc, Boca Raton, Florida.
65. Van der Voort, G.F., 1999, *Metallogrpahy: Principles and practice,* ASM International, Materials Park, pp. 227.
66. Voorhees, H. R., 1979, 'Interim data summary'*, Metal Properties Council*, January 1979, contract no. 174-1, project D.

67. Wilks, G.W., 2002, ‘Weld cracking in a 72-inch stainless steel fcu duct’, *Stainless Steel World*, 21-26.
68. XU, L., Zang, J., & Chen, Y., 2010, ‘Effect of heat input on the microstructure and mechanical properties of 07MnCrMoVR weld joints’, *Chinese Journal of Mechanical Engineering 24,* 1-6.